Use of low-cost photogrammetry to explore the link between soil microtopography and overland flow on hillslopes

Thesis submitted in accordance with the requirements of the University of Liverpool for the degree of Doctor in Philosophy

by

Poonperm Vardhanabindu

14th August 2018

Abstract

The detachment of soil by flowing water on a hillslope is dependent upon the hydraulics of shallow overland flows. The role of microtopography on controlling the spatial patterns of these flows is poorly understood. This study aimed to improve this understanding by undertaking a series of controlled laboratory tests using an experimental plot, consisting of a soil box, a rainfall simulator and overland flow generator. A particular emphasis was placed on developing low-cost photogrammetric techniques to provide novel, high spatial resolution measurements of surface DEMs, 2D flow velocities and distributions of inundation levels and fluid drag. Overland flow experiments were run over surfaces with differing topographies to further examine the effect of discharge and inundation ratio on the spatial patterns of overland flow velocities, hydraulic resistance and fluid drag.

Structure-from-Motion (SfM) was used to measure the microtopography of soils eroded by high intensity rainfall events. An accuracy test showed, for the first time, that SfM is capable of producing highly accurate measurements of microtopographic features at a scale similar to those found on rilled soil surfaces. The results also provided crucial information on how to optimize the acquisition of SFM-imagery in different lightning situations and using different cameras. Analysis

of the DEMs of the eroded surfaces revealed the potential to estimate soil surface roughness and the distribution of elevations based on plot slope.

A low-cost Particle Tracking Velocimetry system was developed to provide novel, detailed 2D surface vector fields, co-located with the acquired DEMs. The results showed that streamwise and lateral velocities have high spatial variability, revealing the flow was 2D. The distribution shape of streamwise velocities was dependent upon discharge and thus relative submergence; the higher submergences, the spatial variability in streamwise velocity was higher and the distributions were wider, flatter and more skewed. The correlation between these distributions and the surface elevations was not sufficiently high to suggest that overland flow velocity can be predicted well by surface elevations alone. On the other hand, local roughness was better correlated, revealing that local variations in surface elevations are more important in controlling spatial patterns of overland flow velocity.

The hydraulic resistance, estimated by the Darcy-Weisbach friction factor, varied strongly with the Reynolds number when the flows were fully turbulent but not when they were close to being transitional, such as in shallow, interrill flows. Surface roughness and relative submergence were found to have a greater or equally strong control as Reynolds number on hydraulic resistance.

Drag force varied considerably over eroded soil surfaces, with some areas experiencing forces an order magnitude higher than others. Areas of high drag forces correlated with the walls of rills and with areas in which flows converged from

different rills. Thus, the distributions of drag force provide some explanation for why rills expand, deepen and migrate, as well as why erosion rates are so variable over hillslopes. The drag force distributions were well-approximated by a two-parameter Weibull distribution, whose parameters were heavily dependent upon surface roughness and hydraulic resistance. The strength of these relationships revealed the potential to predict the drag force distribution, and thus spatial patterns of hydraulic resistance and erosion, based on these simple parameters.

Overall, the study has provided the first detailed study of the effect of microphotography on overland flow patterns, revealing new understanding of the statistical properties of eroded surfaces and the control of roughness on the distribution of 2-D velocities, drag force and hydraulic resistance. These results have important implications for the modelling of overland flow and resultant flow detachment. In doing so, the study has demonstrated the potential of low-cost photogrammetric techniques for providing new understanding of the physics of overland flows, and thus, in the future, driving the development of more physically-based erosion models.

Acknowledgement

Firstly, I would like to thank Liverpool-Mahidol University Partnership for granting me the funds to undertake this PhD programme. I would like to express my sincerest gratitude for the support, understanding and encouragement received from Dr James R Cooper during the four years I have undertaken this PhD project under his supervision. His unwavering contribution of time and knowledge into this project has been the greatest experience of my educational life. I would also like to thank supervisory team members Dr Hugh Smith and Professor Janet Hooke for their constant knowledgeable advice and support.

I am extremely grateful for the mental and physical support I have received from Professor Richard Chiverrell and Dr John Boyle who I know will always provide the utmost help whenever it is needed. This appreciation also goes to Professor Andy Plater, Professor Andreas Lang and Dr Barbara Mauz.

The undertaking of the experiments would not have been possible without the help of Mike O'Connor and the Roxby team of technicians, Ness Garden, especially Timothy Baxter who provided space and facilities to operate the experiment. I would like to thank Paula Houghton and the school's financial team for their generous financially related assistance.

Living 6,000 miles away from home for four years would not have been as warm without the friendship of Rachael Lem who has been the best companion throughout these years and also Fiona Russell, Cai Bird, Amy Lennard, Charlotte Lyddon, Jenny Bradley, Chris Oldknow, Chris Feeney, Jenny Clear, and all my friends in the Roxby Building.

I would like to extend my special gratitude to Elizabeth and Paul Lem for their love, support and encouragement with this thesis.

Finally, I would like to thank my lovely wife Vichaya Sirirattanachai who has sacrificed so much by coming to Liverpool and has been the greatest support. I could have never asked for more.

Thank you to you all.

Table of contents

Abstract i

Acknowledgement iv

CHAPTER 1 Introduction 1-1

1.1. Background 1-1

1.2. Aims and Objectives 1-4

1.3. Thesis outline 1-5

CHAPTER 2 Literature review 2-1

2.1. Introduction 2-1

2.2. Effect of microtopography on overland flow hydraulics 2-3

2.2.1. Hydraulic resistance 2-3

2.2.2. Surface roughness 2-7

2.3. Advances in the measurement of microtopography and hydrodynamics 2-8

2.3.1. High-resolution topographic reconstruction 2-8

2.3.2. Velocimetry techniques 2-11

2.4. Outcome of literature review. 2-14

CHAPTER 3 Methods 3-1

3.1. Introduction 3-1

3.2. Structure-from-Motion 3-1

3.2.1. Structure-from-Motion Procedures 3-2

3.3. Structure-from-Motion accuracy test 3-8

3.3.1. Sensor size 3-11

3.3.2. Image number 3-14

3.3.3. Image size 3-15
3.3.4. Image exposure 3-15
3.4. Experimental plot 3-16
3.5. Microtopography and surface roughness 3-23
3.6. Overland flow hydraulics 3-25
3.6.1. Particle Tracking Velocimetry 3-26
3.7. Probability distribution functions 3-38
3.8. Flow components 3-39
3.8.1. Inundation height 3-39
CHAPTER 4 The accuracy of Structure-from-Motion in the measurement of microtopography 4-1
4.1. Introduction 4-1
4.2. Effect of sensor size 4-2
4.3. Effect of number of images 4-7
4.3.1. Point cloud density 4-8
4.3.2. Accuracy 4-9
4.4. Effect of image size 4-11
4.5. Effect of image exposure 4-13
4.6. Summary 4-18
CHAPTER 5 Effect of slope on the statistical properties of eroded soil surfaces 5-1
5.1. Introduction 5-1
5.2. Digital elevation models 5-2
5.3. Probability distribution function 5-5
5.4. Second-order structure function 5-9

5.5. Local roughness 5-12

5.6. Summary 5-15

CHAPTER 6 The effect of discharge on the spatial distribution of velocity over eroded soil surfaces 6-1

6.1. Introduction 6-1

6.2. Qualitative assessment of flow organisation 6-1

6.2.1. Inundation surface area 6-2

6.3. Spatial distribution of streamwise velocity 6-6

6.4. Spatial distribution of lateral velocity 6-11

6.5. Summary 6-14

CHAPTER 7 Effect of micro-topography on patterns of overland flow 7-1

7.1. Introduction 7-1

7.2. Visualizations of the effect of microtopography on the spatial patterns of overland flow 7-2

7.3. Correlation between surface elevation and overland flow velocity 7-6

7.3.1. Streamwise velocity 7-6

7.3.2. Lateral velocity 7-8

7.3.3. Absolute velocity 7-9

7.4. Correlation between local roughness and overland flow velocity 7-10

7.5. Effect of surface roughness on flow resistance 7-11

7.6. Effect of topography on spatial patterns of fluid drag 7-14

7.7. Summary 7-21

CHAPTER 8 Discussion 8-1

8.1. Introduction 8-1

8.2. Estimating eroded soil surface properties from hillslope gradient 8-1
8.3. Spatial properties overland flow 8-3
8.4. Estimating overland flow hydraulics using surface properties from SfM-derived DEMs 8-3
8.4.1. Overland flow velocity 8-3
8.4.2. Overland inundation level 8-4
8.4.3. Hydraulic resistance 8-6
8.4.4. Surface drag force 8-7
8.5. The effect of spatial variability in overland flow 8-8
8.6. Future research avenues 8-9
8.6.1. Mobile surfaces 8-9
8.6.2. 3D turbulence measurements 8-9
8.7. Key findings 8-11
CHAPTER 9 Conclusion 9-1

CHAPTER 1
Introduction

1.1. Background

The past century has seen a gradual increase in precipitation intensity at a global scale associated with extreme drying in the mid-latitudes (Figure 1.1). Since the middle of the previous century, precipitation intensity has doubled, and it has been forecasted that in the next 30 years, this rate of increase will remain (Tebaldi *et al.*, 2006). Many studies have suggested that an increase in precipitation – and an associated rise in occurrence of pluvial and fluvial flooding – is linked to an increase in catchment sediment yield (e.g. Walling and Kleo, 1979), particularly on hillslopes, where the link between the two is stronger than in fluvial systems. Therefore, the need to study and understand the effects precipitation have on hillslopes is highly important.

Extreme drying, on the other hand, is responsible for expanding desertification along the Mediterranean belt (Hooke and Sandercock, 2012) and many parts of Asia. These two changing factors combined – precipitation and drying – has the potential to cause severe erosion and mass movements on hillslopes as well as flooding. Typically, areas with exposed soil such as semi-arid surfaces generate overland flow more frequently. According to the forecast made by Tebaldi *et al.*, (2006), the increase in precipitation, especially rainfall, and more

frequent dry days should be expected (Favis-Mortlock *et al.*, 2000). This will consequently lead to more frequent flashy flood events (Tamminga, Eaton and Hugenholtz, 2015). Unfortunately, a complete understanding of overland flow hydraulics, how it changes with soil microtopography, and its role in controlling soil erosion processes in order to have better flood prevention systems are still challenging questions to be answered (Smith *et al.*, 2007).

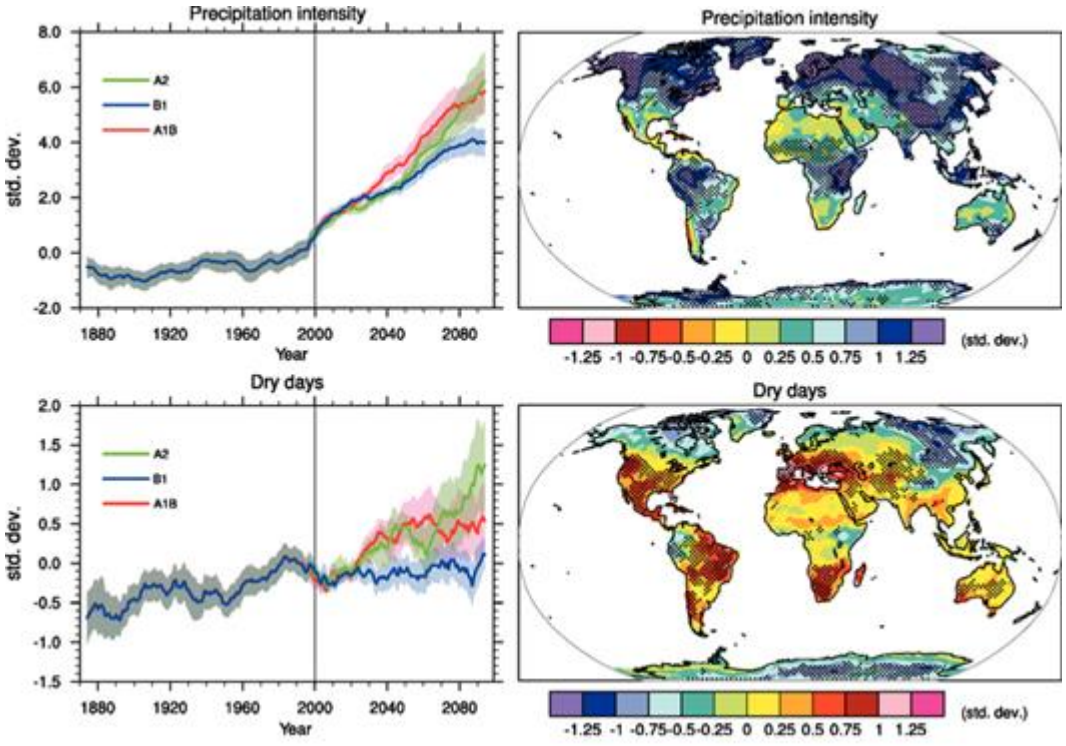

Figure 1.1: Forecasted weather changes (image from Tebaldi *et al.*, 2006)

There is still a large gap in the understanding of runoff on hillslopes and its role in controlling soil erosion processes. To understand these complexities, there has been a substantial amount of research attempting to overcome these questions (Parsons *et al.*, 1996; Wainwright *et al.*, 2008). Through the pass few decades,

scientists have been able to gain fair understandings of the processes at the plot and site scale (Gilley *et al.*, 1992; Michaelides and Wainwright, 2008; Prasad *et al.*, 2009; Kashyap *et al.*, 2010). However, only a handful of researches associate overland flow resistance to the development of hillslope hydrology (Smith and Vericat, 2015), which is usually represented by a single parameter, random roughness (i.e. standard deviation of rill and lumps soil surface). This study, on the other hand, provides detailed investigation of surface factors influencing runoff at microtopographic scale.

The development of physically-based soil erosion models, that are not site-specific, is challenging, but required in order to develop new preventive measures to make rural and urban communities more resilient to the projected increase in precipitation. Examining the control of microtopography on local patterns of overland flow can help play an important role in developing the physical understanding required to help tackle this limitation. Acquiring highly detailed information about these patterns is, however, a technical challenge. Thanks to recent advances in remote photogrammetric techniques, there is now the potential to tackle this challenge. Moreover, the equipment, unlike in the past, can now be acquired at a significantly lower price. Thus, the study will explore the potentials of these low-cost techniques for providing new insights into soil roughness and overland flow dynamics.

1.2. Aims and Objectives

This study has two main aims. First, to provide a detailed examination of how photogrammetry can be used to measure microtopography and shallow, overland flow hydraulics. Secondly, to examine the effect of microtopography on spatial patterns of overland flow. The specific objectives are:

1. To develop low-cost photogrammetric techniques to provide novel, high spatial resolution measurements of surface DEMs, 2D flow velocities and distributions of inundation levels

2. To characterise the microtopography of eroded soils through a statistical description of their roughness and distributions of surface elevations, and how they vary with slope gradient.

3. To improve the understanding of the effect of microtopography on local patterns of overland flow velocity, fluid drag, and hydraulic resistance over a range of relative submergences

4. To identify the statistical attributes of surface microtopography that have the potential to predict spatial patterns of overland flow.

These aims and objectives will be achieved through conducting a series of controlled laboratory tests using an experimental plot, consisting of a soil box, a rainfall simulator and overland flow generator. Rainfall simulation experiments will generate soil surfaces with differing microtopographies, and overland flows of differing discharge will be run over these surfaces. Structure-from-motion (SfM)

and Particle Tracking Velocimetry (PTV) will be used to provide co-located measurements of the soil surface and overland flow velocity field.

1.3. Thesis outline

Chapter 2 reviews the current understanding of overland flow hydraulics, highlighting where current limitations lie, and briefly introduces the means by which to overcome these limitations using the latest developments in photogrammetry. **Chapter 3** describes the methods and apparatus. This includes a description of how digital elevation models were derived from SfM, its accuracy and its optimisation. Also, this chapter describes the experimental programme, including the experimental plot, experimental conditions and the use of PTV. **Chapter 4** presents a series of accuracy tests of SfM and explores the factors that affects its accuracy in order to optimise the measurements. **Chapter 5** examines the implementation of SfM to measure the microtopography of eroded soils, and the roughness and statistical properties of these surfaces. **Chapter 6** explores the effect of discharge, relative submergence and surface roughness on spatial patterns of overland flow. **Chapter 7** examines the effect of microtopography on these patterns, including the correlation between the surface and the flow, and its effect on fluid drag and hydraulic resistance. **Chapter 8** discusses, based on the results presented, whether the statistical properties of eroded soil surfaces can be estimated, and whether overland flow properties can be predicted based on these properties. The chapter also examines the implications of the observed spatial

patterns of overland flow for soil erosion, and future research avenues. Finally, **Chapter 9** provides a summary of the main findings and their implications.

CHAPTER 2
Literature review

2.1. Introduction

Erosion by water can be classified into several processes. Firstly, splash erosion caused by the direct impact from precipitation (e.g. Poesen and Savat, 1981; Quansah, 1981). Craters from the raindrops generate microtopographic roughness on the exposed surfaces (Furbish *et al.*, 2007; Bullard *et al.*, 2018). The water body may immediately infiltrate into the soil beneath, be temporarily stored in craters (pond) before infiltrating, or flow over the surfaces. The travel of water body over surface is known as overland flow. Secondly, at a point when this ponding occurs, or when the ponding exceeds the height of the craters, but the overland flow does not have sufficient energy to entrain the soil, interrill erosion occurs. This process involves raindrops detaching the soil beneath a thin layer of water (e.g. Torri *et al.*, 1987; Kinnell, 1991) and/or being eroded by unconcentrated flow detachment (e.g. Kinnell, 1993), and the detached particles being transported within the flow (e.g. Kinnell, 2001). Thirdly, rill erosion occurs when the overland flow has sufficient energy to detach, transport and eventually deposit sediment on the surface it travels over. In these concentrated flows sediment can be detached and transported as either bedload or suspended load (Wainwright *et al.*, 2008). These differing erosion processes occur at different temporal and spatial scales, and thus produce multi-

scale erosional and depositional features on the surface. This roughness, and its organisation, has important consequences for the velocity and spatial patterns of overland flow, and thus its role in soil erosion and landscape evolution. This interaction between the soil surface and overland flow hydraulics is generally quantified using equations originally developed for pipe flows, and later adjusted for river flows. However, overland flows are likely to behave differently since they are shallower than river flows and are more dependent upon the topography they flow over compared to pipe flows.

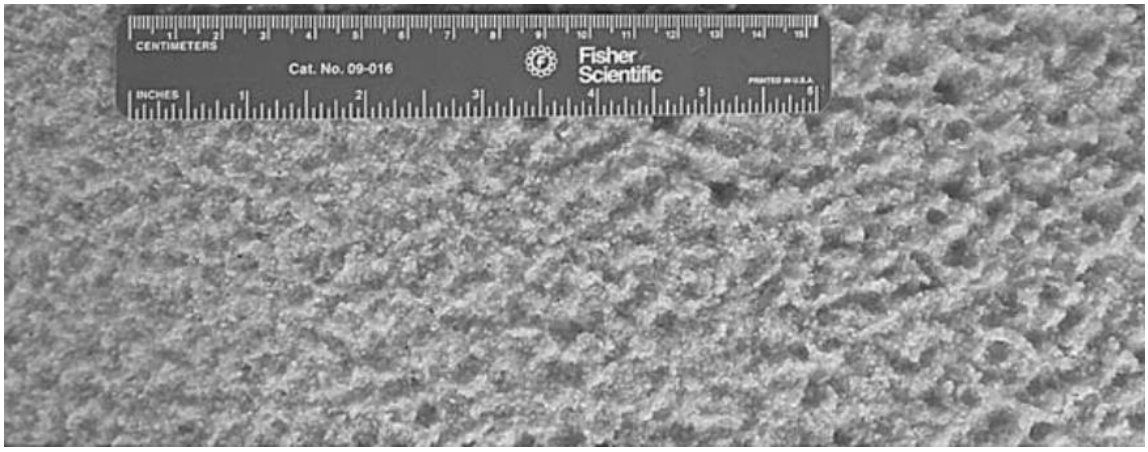

Figure 2.1: Micro-craters created by raindrop creating roughness over sand surface. From Furbish *et. al.,* (2007)

This chapter briefly reviews this current understanding of overland flow hydraulics, highlighting where current limitations lie, and briefly introduces the means by which to overcome these limitations using the latest developments in photogrammetry.

2.2. Effect of microtopography on overland flow hydraulics

2.2.1. Hydraulic resistance

The study of hydraulic resistance was initiated and developed from one-dimensional pipe flows (Smith *et al.*, 2007), and later developed for river flows, in which the flow is assumed to be steady and uniform. One of the most well-known flow resistance equations is the Darcy-Weisbach equation. In many studies, for example, in a study done by Gilley *et al.* (1992), the Darcy-Weisbach friction factor (roughness coefficient) is used to quantify the relationship between surface and flow in terms of the energy lost as the water flows over the rough surface (hydraulic resistance). This friction factor is influenced by the dimensions of the channelised flow, slope gradient and overland flow velocity:

$$f = \frac{8gRS}{V^2} \tag{2-1}$$

where g is the acceleration due to gravity, R is the hydraulic radius, S is the average slope and V is the velocity.

Many studies relate Darcy-Weisbach friction factor to the turbulence of flow, approximated by the Reynolds number, *Re* (e.g. Abrahams *et al.*, 1986; Gilley *et al.*, 1992; Bryan, 2000). For example, Gilley *et al.* (1992) suggested that at low inundation levels, the Darcy-Weisbach friction factor f normally increases with *Re* when the flow is laminar or transitional, and decreases with increasing *Re* when the

flow is fully turbulent. However at higher inundations, *f* decreased with *Re* for laminar, transitional and fully turbulent flows.

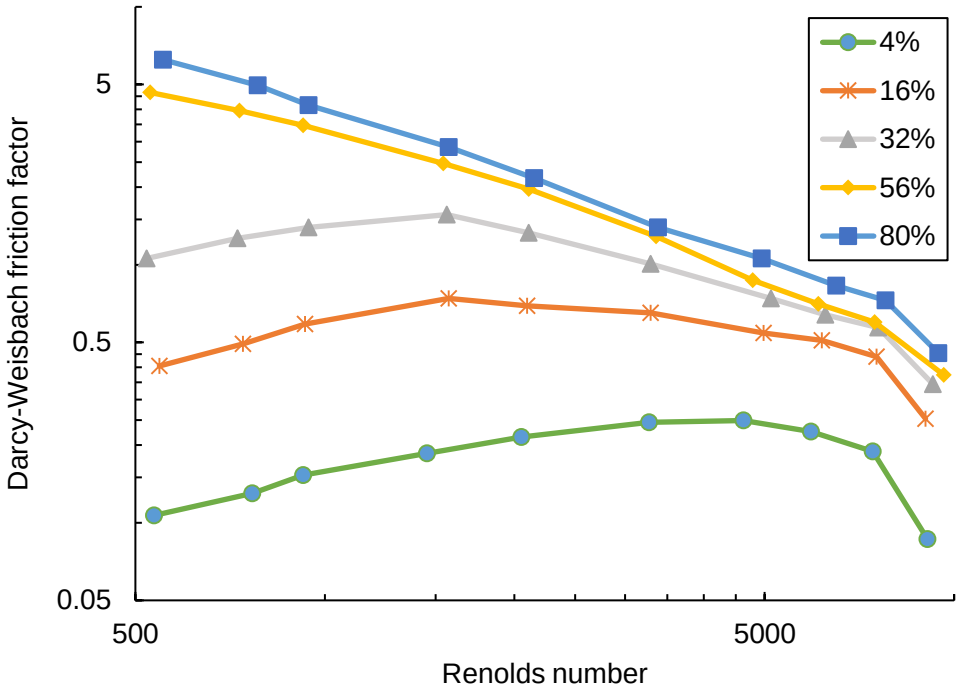

Figure 2.2: Relationship between Darcy-Weisbach friction factor and Re from Gilley *et al.* (1992). Each line represents different inundation percentages.

Smith (2011) suggested that relating *f* with *Re* can be misled by a number of factors, for example, this relationship can be modelled only when the flow is well inundated. Therefore, the relationship should be considered with caution. Instead of the relation between Darcy-Weisbach friction factor and *Re*, Lawrence (1997) suggested that inundation ratio (a ratio between inundation height and elevation range; also known as relative submergence or relative roughness) and friction factor

was more critical for the modelling of overland flow hydraulics. The terminology for inundation ratio, and Lawrence's classification of flow, is shown in Figure 2.3. Lawrence (1997) found that at low inundation ratios (partially inundated), flow resistance was governed by the characteristics (e.g. roughness) of material covering the surface; hence the friction at this level was generally high. Friction decreased rapidly as inundation increased because the water could travel more freely in a vertical direction. When surfaces were well-inundated, the frictional resistance tended to decrease gradually with a rise in inundation ratio since the water could flow relatively independently of the surface beneath.

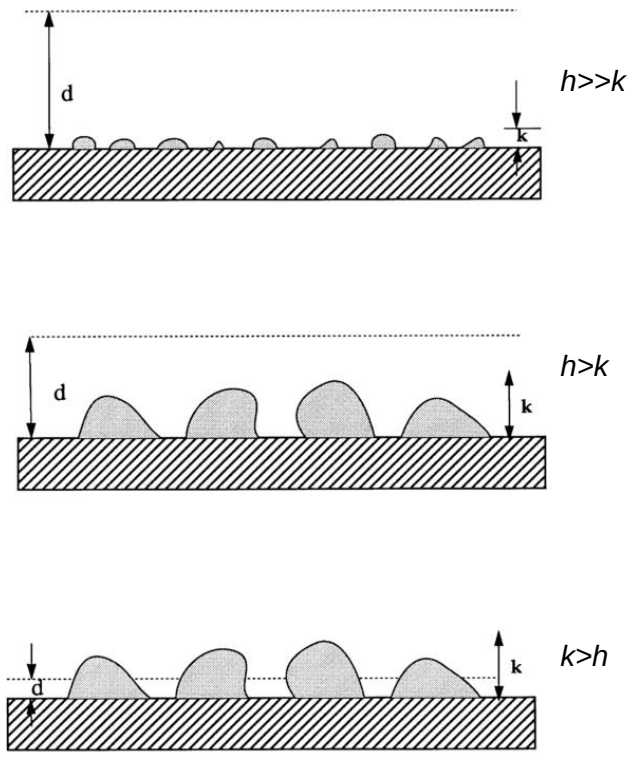

Figure 2.3: (top) well-inundated flow; (middle) marginally inundated and (bottom) partially inundated. From Lawrence, 1997

However, the use of a flow resistance equations originally developed for pipe flow, such as the Darcy-Weisbach equation, is questionable for three important reasons. First, eroded soil surfaces, unlike pipe surfaces, tend to have multi-scale roughness that reflects the different erosion processes that form them. Thus unlike pipe flows, this roughness consists of friction created both by the grains which form the surface (grain roughness), such as impact craters and grain imbrication, and roughness introduced by the surface undulations, such as rills (form roughness; Li, 1994). Therefore these two scales of friction are likely to generate different levels of flow resistance and energy loss. Secondly, the flow-inundation ratio of overland flows is much lower than in pipe flows, resulting in different levels of flow resistance (Figure 2.2; Gilley et al., 1992). Thirdly, overland flows are unlikely to be 1D and uniform. The flow energy loss is greatest in the near-bed region, where turbulence is generated when the water accelerates and decelerates as it flows around and over surface roughness elements, forming a turbulent boundary layer. In shallow flows, this layer can cover the entire range of the flow, from the surface to the water surface (Cooper and Tait, 2008, 2009; Rice *et al.*, 2014), creating distinct, coherent vortices throughout the flow depth. Furthermore, not all overland flows are channelised, such as in rills, and are often multi-threaded and highly spatially discontinuous. Thus overland flows are likely to be 3D in nature and non-uniform. Thus an examination of the effect of microtopographic roughness on overland flow requires an understanding of how the spatial characteristics of the rough surface affect the spatial patterns of overland flow.

2.2.2. Surface roughness

Many studies have sought to understand the link between surface roughness and overland flow velocity by examining the effect of random roughness (*RR*). The study of the effects of topography on overland flow hydraulics has covered several factors. One is surface roughness. Many studies suggest that random roughness (*RR*), which can be determined by the standard deviation of the surface elevation, has a great influence on overland flow, being one of the indices for surface ponding and infiltration (Engman and Eswin, 1986; Chu *et al.*, 2012; Legout *et al.*, 2012). Bryan (2000) and Römkens *et al.* (2002) suggested that *RR,* which is highly influenced by splash erosion, in turn, also influences soil erodibility on hillslopes. However, *RR* as a single index does not represent the spatial and local components of the surface (Huang and Bradford, 1990; Vidal *et al.*, 2010; Chu *et al.*, 2012). As a result, the evaluation of the impacts of local roughness on overland flow hydraulics is required.

There has been very little work done to determine the spatiotemporal variations of soil surface roughness (Local roughness; *LR*). As mentioned above, many studies use a single index to determine the roughness of a surface at a certain scale. This particular index cannot justify the dynamic and complexity of surface roughness. Since roughness is a property that plays an important role on governing surface runoff and erosion processes (Kirkby, 2001; Haubrock *et al.*, 2009), there needs to be a more robust system to justify the spatiotemporal variations of soil surface roughness. As a result, local root-mean-square values at certain measurement sizes throughout the soil surface were used in a work demonstrated

by Haubrock *et al.* (2009). They have proposed that the combining change of topography at the macro-scale governs the hydraulics of overland flow. Though one can assume that the assumption made is true, there has yet to be a study to confirm what effects *LR* have on the hydraulics of overland flow.

2.3. Advances in the measurement of microtopography and hydrodynamics

The review above has highlighted the need to relate the spatial characteristics of the rough surface with the spatial patterns of overland flow. Fortunately new photogrammetric techniques developed in the fields of computer science and fluid diagnostics offer this new capability. In particular, recent developments in consumer-grade cameras and open-source software have allowed high-resolution topographic surveys and spatially-distributed flow measurements to be performed at a relatively low cost. These techniques show great promise to reveal new, detailed information about the way in which shallow overland flows interact with multi-scale roughness.

2.3.1. High-resolution topographic reconstruction

Traditional high-resolution topographic surveying techniques are costly (Westoby *et al.*, 2012; Smith *et al.*, 2015; Carrivick *et al.*, 2016). Thus, acquisition of topographic data, in many cases, had to be passed on to specialised third party agencies, while methods that could be performed by researchers, such as pin-meter

(plot scale) and Differential Global Positioning System (dGPS) (field scale), were destructive to the studied site and time consuming.

Despite the development of advanced equipment such as terrestrial laser scanners (TLS) which is highly capable of acquiring high-resolution topographic data in a shorter period, the use of TLS can still be inconvenient due to the low mobility and long scanning times. The emergence of close-range digital photogrammetry in the past decade or so, mean that the acquisition and reconstruction of three-dimensional topographic data is now much more affordable and can be performed with relative-ease (Remondino and El-Hakim, 2006; Furukawa and Ponce, 2007; Matthews, 2008). In particular, over the past few years the use of Structure-from-Motion (SfM) in geomorphology has grown in popularity for these very reasons (Harwin and Lucieer, 2012; Fritz *et al.*, 2013; Javernick *et al.*, 2014; Prosdocimi *et al.*, 2015; Tamminga *et al.*, 2015; Ferreira *et al.*, 2017). This technique involves taking sequential images of the object or scene, and through software processing, the output is given as 3D DEMs.

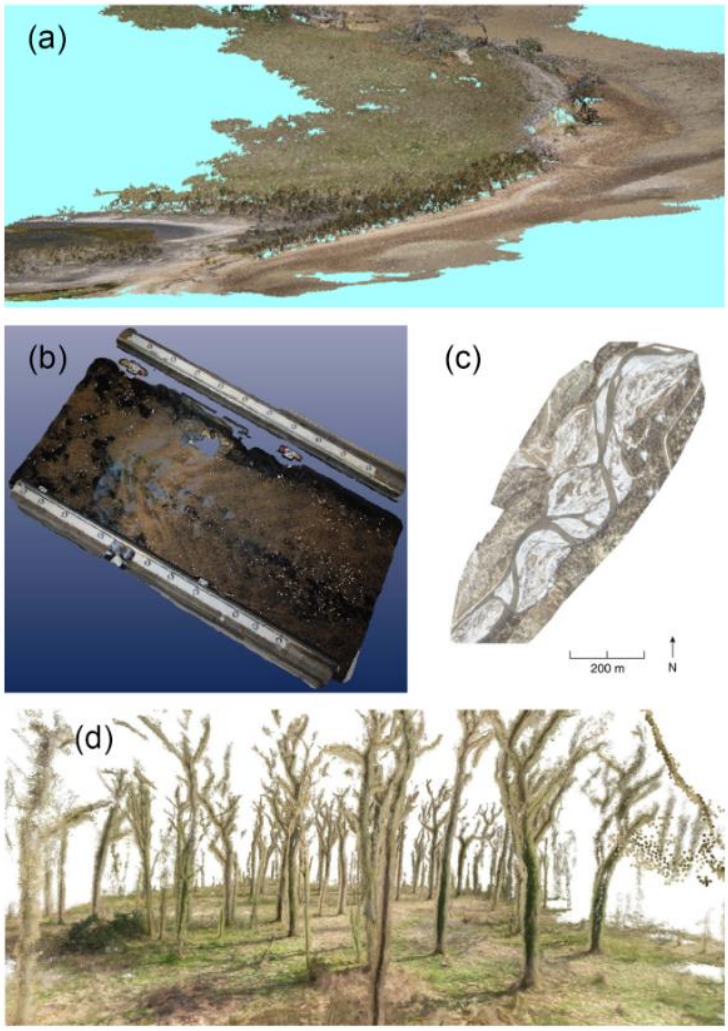

Figure 2.4: Examples of how SfM is used in different situations. (a: Harwin, 2012; b: Ferreira, 2017; c: Tamminga, 2015; d: Fritz, 2013)

At a field scale, Westoby *et al.*, (2012) tested the accuracy and speed of SfM and found that the quality of SfM-derived DEMs was similar to those derived from TLS. In their study, a consumer-grade digital camera was used as part of the process to produce SfM-derived DEMs of three different landscapes – an exposed rocky coastal cliff, a breached moraine-dam complex and a glacially-sculpted bedrock

ridge. Their results showed that SfM-derived DEMs can achieve decimal-scale accuracy.

Smith *et al.,* (2015) reviewed results from different methods for acquiring topographic data and found that Structure-from-Motion (referred to as Photogrammetry and Structure-from-Motion Multi-visual Stereopsis) is capable of acquiring a compatible result to more expensive methods such as TLS and Airborne Light Detection and Ranging Scanning (ALS/LiDAR).

Despite the popularity of SfM, the focus of previous work has all been measuring topography at large scales, such as river channels, cliffs (e.g. Westoby *et al.*, 2012; Fritz *et al.*, 2013; Javernick *et al.*, 2014; Smith, Carrivick and Quincey, 2015). SfM has yet to be used to measure the microtopography of soils. Thus the accuracy and the resolution of the technique at these much smaller scales, has yet to be established.

2.3.2. Velocimetry techniques

Particle-based velocimetry techniques are motion-based techniques used to measure the velocities of particles as a surrogate measure of flow velocity. In the past two decades or so, three main devices have been widely used to measure the velocity of channelised flows: electromagnetic current meter, acoustic Doppler velocimeters and laser Doppler velocimeters (Robert, 2014). The most popular amongst the three has been the two-dimensional electromagnetic current meter; a magnetic field is generated when water moves through the probe, and the probe then converts

voltage produced from this movement into velocity data. The more recently developed velocimeter amongst the three is the acoustic Doppler velocimeter (ADV). This equipment is highly applicable both in laboratory and in the field. The ADV is capable of measuring three-dimensional velocity (streamwise, lateral and vertical directions) by measuring the acoustic Doppler shift created by particles moving through the measurement volume. All these velocimeters have limitations however, that make them difficult, if not impossible to be used in overland flows. First, they only provide measurements of velocity at a single location. Therefore, to gain detailed spatially distributed measurements in the multi-threaded flows common over soils surfaces is time consuming. Secondly, they need to be submerged causing disturbance of the flow. This facet is a particular problem in shallow flows. Thirdly, the standoff distance between the probe and the measurement volume is too large to measure in the depths commonly observed in overland flows.

To overcome these limitations, dye tracing is extensively used to measure overland flow velocity (Abrahams *et al.*, 1986; Smith *et al.*, 2011; Legout *et al.*, 2012). This technique involves measuring the time it takes for the leading edge of the injected dye to travel from the injection point to a known distance downslope. Although this technique provides remote measurement, the measurements are usually taken infrequently and it does not provide spatially distributed measurements of velocity. Thus understanding of the fine-scale, spatial patterns of overland flow velocity is lacking.

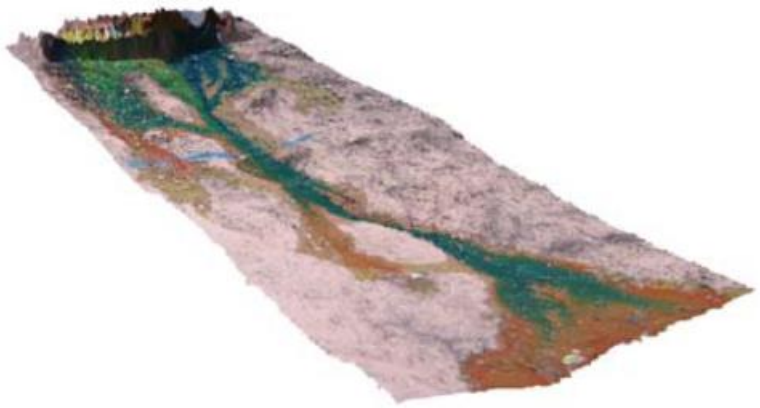

Figure 2.5: Dye tracing over rilled topography. From (Smith *et al.*, 2007)

However, the development of photogrammetric velocimetry over the past decade provides a means by which to improve this understanding. Two of the most used techniques are Particle Image Velocimetry (PIV) and Particle Tracking Velocimetry (PTV). Both techniques share one common principles, they estimate particle displacements using sequential images, but differ in one important way; PIV is based on image correlation of particle patterns (Raffel *et al.*, 2007) and PTV on the tracking of individual particles (Tropea *et al.*, 2007). In geomorphology, PIV has been predominately used to measure complex flow velocity patterns, such as by fluvial researchers in the measurement of turbulent, coherent flow structures over sediment surface (Cooper and Tait, 2008; Rimkus, 2012; Cea *et al.*, 2014; Rice *et al.*, 2014; Evans *et al.*, 2016). PTV has been used mainly to track the movement of transported sediment (e.g. Hergault *et al.*, 2010). The advantages of PTV and PIV over traditional velocimetry measurements are they provide remote, spatially distributed velocity measurements and can be used to measure velocity patterns in any type of flow and at any scale. However, they have yet to be used to measure overland flows

on hillslopes. Combining the use of SfM with these techniques therefore provides the exciting potential to provide co-located, high-resolution measurements of topography and overland flow velocity that reveal new understanding of the local effect of topography on overland flow velocity patterns.

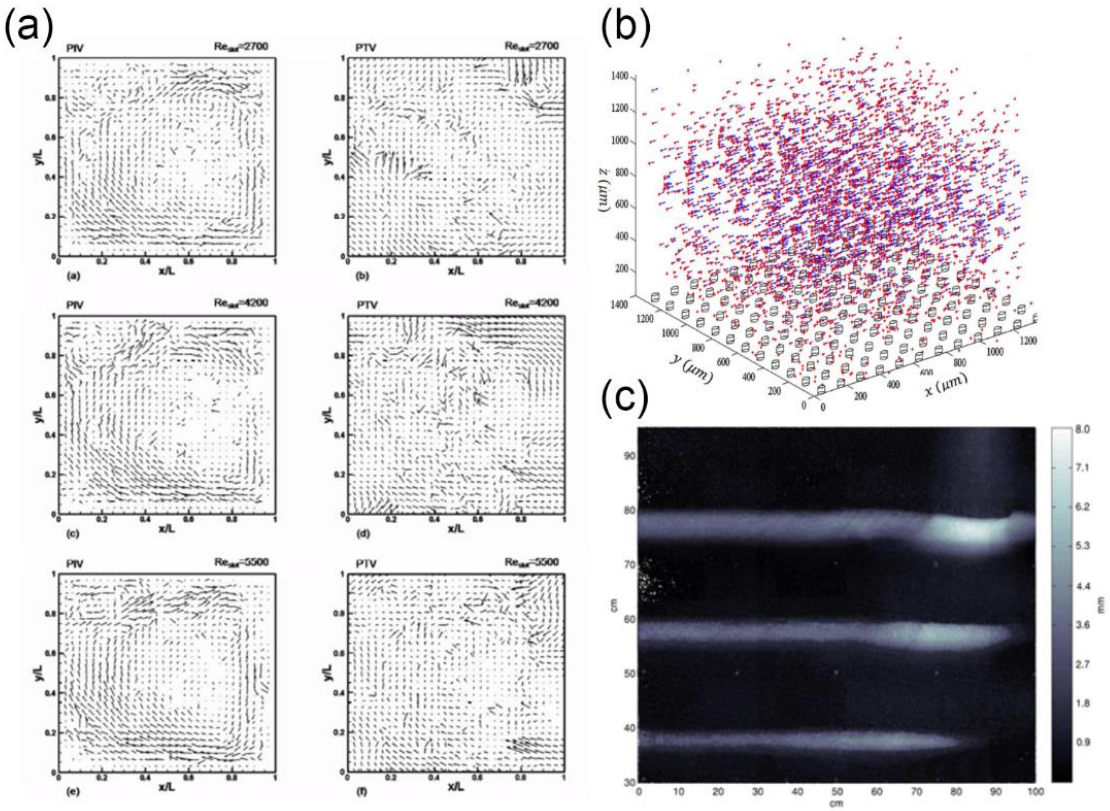

Figure 2.6: Examples of PIV and PTV work from the literature. (a: Fu *et al.*, 2015; b: Bocanegra Evans *et al.*, 2016; c: Legout *et al.*, 2012)

2.4. Outcome of literature review.

Previous attempts to understand the effect of microtopography on overland hydraulics have concentrated on quantifying hydraulic resistance and the effect of random roughness on overland flow velocity. These attempts are hampered by the

common assumption that overland flows behave in a similar manner to pipe and river flows, but overland flows are rarely 1D and uniform. Instead, these shallow flows are not always channelised as they occur over multi-scale roughness. Therefore these flows can be multi-threaded, 3D and non-uniform. Thus, an examination of the effect of microtopographic roughness on overland flow requires an understanding of how the spatial characteristics of the rough surface affect the spatial patterns of overland flow. Thanks to advancing technology, non-destructive photogrammetric techniques can be used to measure these characteristics. Thus, these techniques have great potential to reveal new understanding of overland flow hydraulics especially the ability to acquire high-resolution information of the surface. The review has highlighted that this new understanding should to be gained for overland flows with a range of inundation ratios, given the important role this ratio has on hydraulic resistance, and over surfaces with different scales of roughness and organisation.

CHAPTER 3
Methods

3.1. Introduction

The first part of this chapter describes how digital elevation models were derived from Structure-from-Motion (SfM), how its accuracy was tested. The second section focuses on the experimental programme, including the experimental plot, measurement techniques and experimental conditions. The experimental programme consisted of three stages: (1) generating eroded soil surfaces using a rainfall simulator; (2) measuring the microtopography of these surfaces; and (3) generating different overland flows over the surfaces and measuring their hydraulics.

3.2. Structure-from-Motion

Structure-from-Motion is a photogrammetric technique that generates three dimensional data from a series of two dimensional images using geometrical analysis (Westoby *et al.*, 2012; Carrivick *et al.*, 2016). It is the technique that was selected in order to reconstruct the surfaces of the experiment. A series of experiment was done to examine whether its accuracy is adequate to measure micro-topographic changes. The tests were carried out by comparing SfM-derived point clouds of LEGO® bricks

with their equivalent computer-aided design (CAD) models. This section, the procedures of acquiring SfM-derived results is described.

3.2.1. Structure-from-Motion Procedures

In order to generate a three dimensional environment, a series of images has to be taken and inputted into the dedicated software. The output of the software is an array of horizontal, lateral and vertical coordinate values (XYZ). Each of the processes involved are shown in Figure 3.1. Firstly, the software detects similar features in each image and matches each photograph accordingly. Secondly, the software reconstructs common reference points between images at low resolution (sparse points), places the values (points) into a matrix environment (point clouds), and calculates the position of the cameras used to acquire the images. Thirdly, from known positions of cameras and images, pixels of images which share common positions are calculated to generate dense points. Finally, to produce a complete three dimensional model of the target, the mesh can be texturised to imitate the colour of the actual target.

3.2.1.1. Image acquisition

In order to produce high quality SfM-derived DEMs, a relatively dense set of point clouds should be constructed. Since a greater overlap between image pairs produces denser point clouds, sufficient image coverage of the target at different angles is required. To produce digital elevation models for the accuracy tests and for characterising the microtopography of the eroded soil surface, an image sequence

was acquired, in which each image was taken with at least a 50% overlap with the neighboring image and the camera was positioned at two heights and 360 degrees around the target (Figure 3.2). This specific approach of SfM was first developed by Furukawa and Ponce (2007) in the field of digital object reconstruction and later used in geomorphology (Smith *et al.*, 2015), and is often termed Structure-from-Motion Multi-View Stereo (SfM-MVS).

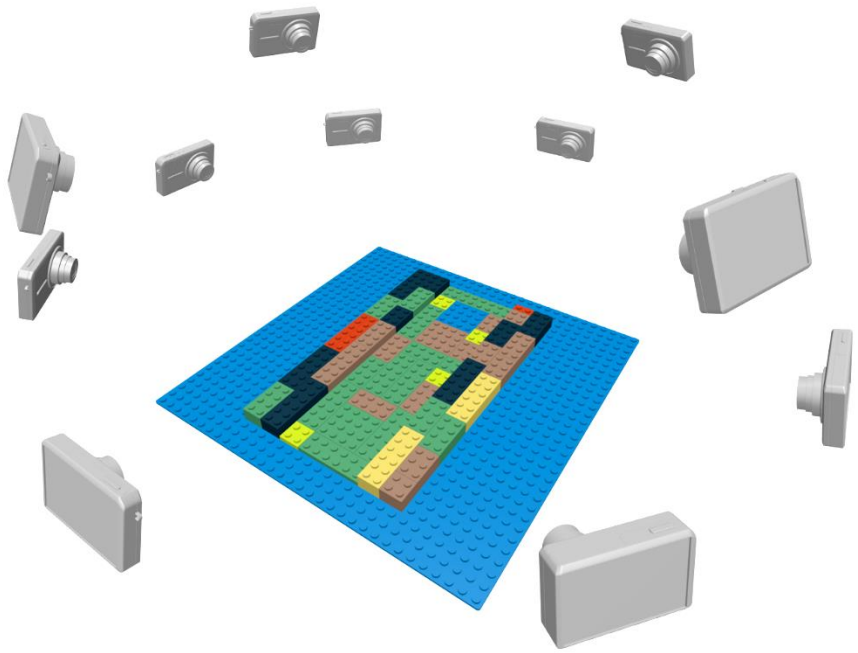

Figure 3.1: Position of the camera of how the image sequence was taken. The number of the camera positions should increase according to the size of the target in order to maintain at least a 50% overlap between each image pair

3.2.1.2. Image post-processing

After the image sequence was acquired, each photo was assessed in order to optimise the quality of the point clouds. The images were checked to determine

whether parts of the area were consistently focused, and had balanced brightness and contrast. If too many images were out-of-focus, the image sequence was re-taken. When the images had insufficient brightness or contrast (which will be referred to from this point as exposure), post-processing was carried out. Acceptable exposure was judged by the distribution of RGB histogram. For images with inadequate brightness, the brightness and contrast of these images was optimized using highlight and shadow compensation in Adobe Lightroom (Adobe Systems, 2017a). Highlight and shadow refers to the value of pixels where highlights are higher values, shadows are the lower values.

3.2.1.3. Point clouds and 3D model generation

After the image sequences were taken and optimised, they were processed in a SfM software program called Agisoft PhotoScan 1 (Agisoft LLC, 2016) for 3D processing. Agisoft PhotoScan was chosen as the processing software due to two main reasons – (1) users have the ability to optimise the settings and control the output specification, (2) the software is widely used in geomorphological studies (Westoby *et al.*, 2012; Smith *et al.*, 2015). Figure 3.3 illustrates the settings interface for this software.

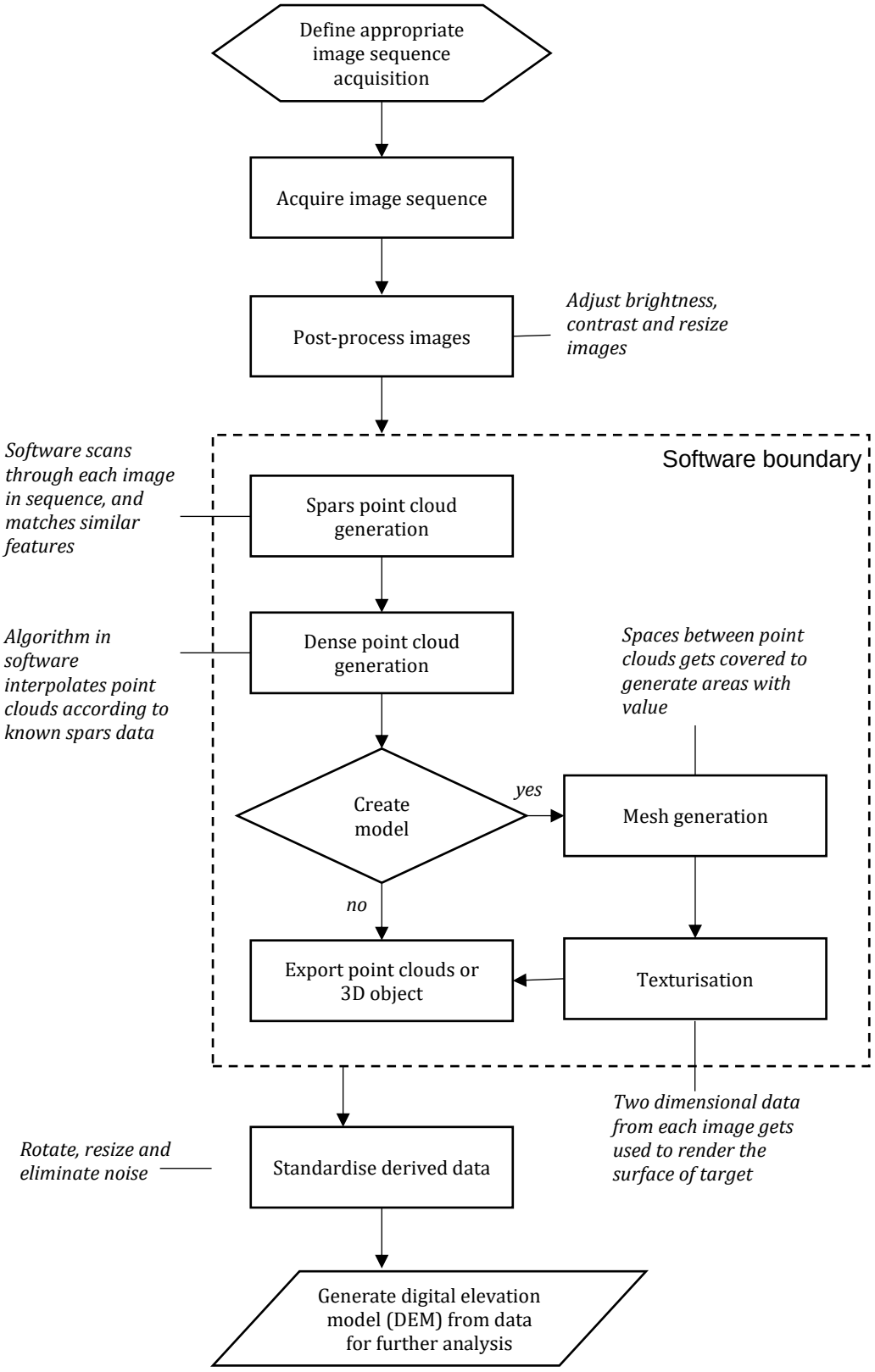

Figure 3.2: Procedure to produce a SfM-derived DEM

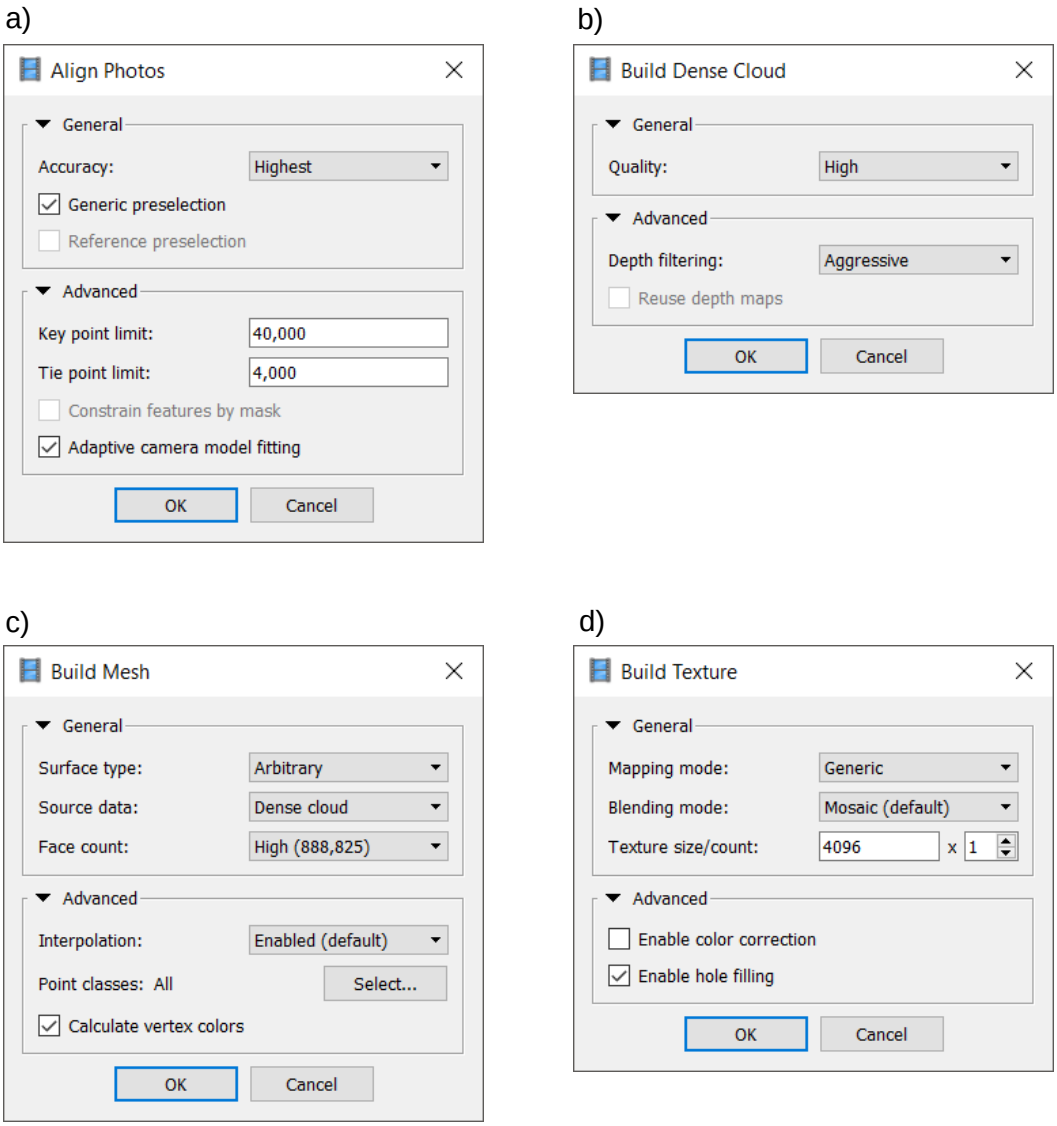

Figure 3.3: The adopted settings in Agisoft PhotoScan 1

Firstly, the images were aligned in Agisoft PhotoScan. The settings for the first step were set to 'Highest' accuracy (Figure 3.3a), which is the highest optimisation available in the software, in order to produce dense populated sparse point clouds. 'Generic preselection' was selected in order to speed up the processing time; overlapping pairs of photos are selected by the software's algorithm to preserve computational resource by using the lower optimisation first then increasing the

precision when lower precisions are not effective. In the advance settings, the key point limit[1] and tie point limit[2] were set as default settings where the key point limit was set at 40,000 and tie point at 4,000. When the photos were aligned, which take approximately one to two hours (depending on the number of images in the sequence), dense point clouds for each image pair were generated. In this stage (Figure 3.3b), the quality was set at "High" which is the second maximum option ("Highest" being the maximum setting). This setting was chosen as compromise between computational time and the level of required point cloud quality. This stage took approximately two to four hours. The third step was involved constructed a mesh over the dense point clouds (Figure 3.3c). There were two settings to choose from when constructing the mesh – Height Field and Arbitrary. The Height Field option is used when the target surface is a flat plane or cover a large area such as targets that require photo acquisition from unmanned aerial vehicles. In this study, the setting was set to "Arbitrary". Arbitrary surface type is generally used for closed objects of which image sequences were acquired by SfM-MVS. Once the mesh was created, a 3D cubical interpolation method was used to fill in any missing values using the software's algorithm. The final stage was to create texture for the model. The "Build Texture" option renders the colour information from the image files over the mesh model, allowing the mesh to visually imitate the target. This mesh was then

[1] Number which indicates upper limit of feature points on every image to be taken into account during processing.
[2] Number which indicates upper limit of matching points for every images.

exported as a 3D object (.OBJ) file for further post-processing. These files contain the coordinates and texture of the mesh.

3.2.1.4. Model post-processing

Post-processing of 3D object files was performed in CloudCompare 2 (CloudCompare, 2017). CloudCompare is an opensource program which can process 3D objects in many formats and is commonly used in SfM post-processing (Lague *et al.*, 2013; Prosdocimi *et al.*, 2015). In CloudCompare, the objects were standardized (rotated and resized) and were resampled to have certain numbers of point clouds in order to match with the lowest resolution model (explained in Chapter 4). The outputs from this process can be exported in any 3D model format (e.g. .GRD, .TIFF, .OBJ, .TXT, etc.).

3.3. Structure-from-Motion accuracy test

As highlighted in Chapter 2, the ability of SfM to accurately resolve microtopography is unknown. To overcome this limitation, SfM-derived DEMs of LEGO® brick models, involving bricks of differing size, shape and configurations, were produced. First, each brick is manufactured to a precision of less than 5 μm (LEGO, 2017a). Thus, one could reasonably assume each brick had the same geometry and size, which was important when evaluating accuracy over the entire target area. Secondly, an exact CAD model of the brick configurations could be produced using LEGO Digital Designer 4 CAD software developed by LEGO® (LEGO, 2017b). Thus, SfM accuracy could be tested through a comparison of the SfM-derived

DEM and the CAD model. The consequence is that the CAD model allows an unbiased test of SfM accuracy, negating the need to perform the comparison using a DEM derived from another measurement technique. Furthermore, the resolution of the CAD model is much higher than could be achieved with any measurement techniques. These facets represent a significant advantage over previous tests of SfM accuracy in geomorphological applications that have used terrestrial laser scanners and LiDAR (Harwin and Lucieer, 2012; Skarlatos and Kiparissi, 2012; Fritz *et al.*, 2013), which have their own inaccuracies and bias. Thirdly, the bricks contain multi-scale surface variability in the form of knobs on the surface, brick geometry and multi-layering of bricks, which is important when considering the ability of SfM to measure multi-scale roughness on eroded hillslope-surfaces (although there is no suggestion the brick models are a facsimile by any means). Fourthly, the bricks come in various colours and therefore allow us to test the effect of target colour on accuracy. Fifthly, the bricks have strong geometrical forms (i.e. sharp edges, rough knobs, square corners) and therefore produce a more acute test of accuracy than would be possible with a natural sediment surface. Finally, any error caused by the SfM process is illustrated clearly due to the basic and universal shape of the bricks.

A LEGO® model was built using bricks of varying colour, and constructed to produce a linear channel that had a depth-to-width ratio of 7 (Figure 3.4), which is a common ratio observed in natural rills (Shit and Maiti 2012). This ratio was taken so that the effect of shadowing, that would be a potential problem when measuring rilled surfaces, could be explored, but there is no suggestion the model is representing a natural feature.

The SfM image sequence was taken by using the method shown in Figure 3.1. For each model, the image sequence typically contained around 40 images, with the aim of obtaining 20 all around the target at a low angle to the surface and 20 more at a high angle (**Error! Reference source not found.**). Examples from the images sequence can be seen in Figure 3.5. In CloudCompare (2017), the SfM-derived point clouds of the LEGO® model were aligned to the equivalent CAD model so that the models shared common coordinate systems. Each SfM-derived DEM was then compared to the CAD model to examine the difference in elevations and assess the level of accuracy. This accuracy test is the focus of Chapter 4.

In this tests four images, and camera-related factors that might affect SfM-accuracy were examined. The tested factors were: (1) camera sensor size; (2) the number of images used to derive the point clouds; (3) image size; and (4) image exposure and its related effect on brightness and contrast

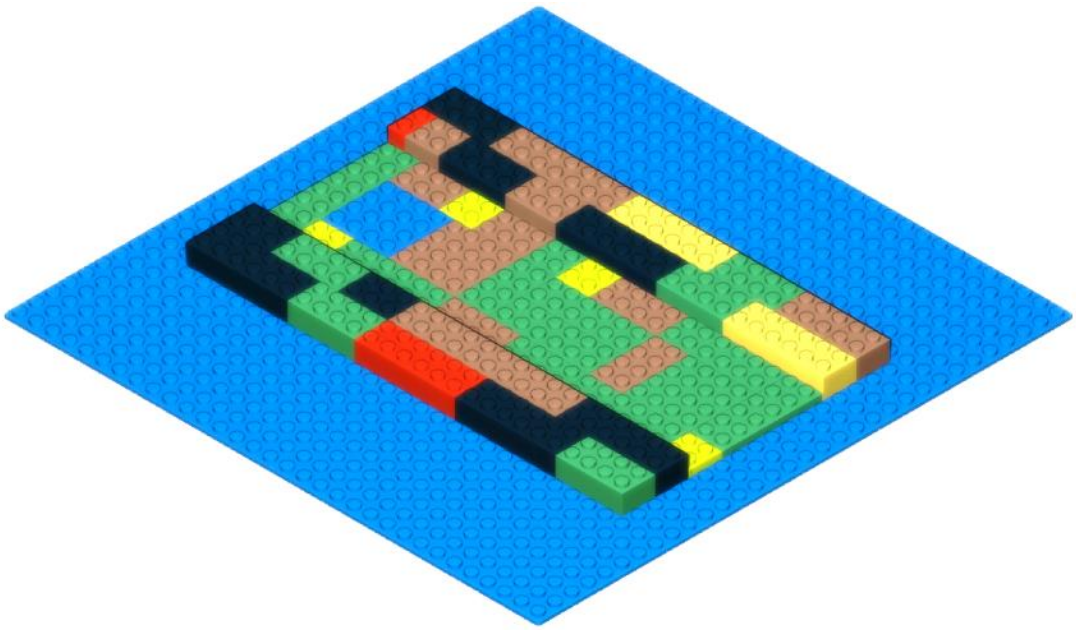

Figure 3.4: CAD model of the LEGO bricks. The ratio of the height of the two parallel linear bars and the width of the middle area was set at 1:7 in order to match the ratio of actual environmental rills.

3.3.1. Sensor size

Three cameras with differing sensor sizes were used: (1) Sony ILCE-6000 mirrorless camera with Carl Zeiss Vario-Tessar T E 16-70mm f/4 ZA OSS lens with a 24.3 MP APS-C sensor (sensor size = 25.1 × 16.7 mm); (2) a Fujifilm FinePix XP150 with a 14 MP compact 1/2.3" sensor (6.17 × 4.55 mm);, and (3) an LG Nexus 5 Smartphone with a 8 MP 1/3.2" sensor (4.5 × 3.4 mm). All three cameras were set into Automatic mode. A total of 40 images were taken from each camera to build dense point clouds. The derived point clouds were subsampled to statistically compare 500,000 points in order to produce a less biased. This number of points is the maximum that could be achieved with the LG Nexus 5 camera.

The three chosen cameras not only have different sensor sizes but also considerable differences in cost, a factor that can be important when choosing which camera to use. The Sony ILCE-6000 (R1) camera with Carl Zeiss Vario-Tessar T E 16-70 mm f/4 ZA OSS lens was the highest in price. As of May 2016, the equipment costed £1,165. The Fujifilm FinePix XP150 (R2) is a compact camera that cost significantly lower. It was £135, as of May 2016. Finally, the LG Nexus 5 (R3) phone camera. As of May 2016, this phone cost £172.

Table 3.1: Summary of the cameras used in the tests

Name given	Camera	Sensor size (mm)	35 mm equivalent focal length (mm)	Price (£)
R1	Sony ILCE-6000	22.2 x 14.8	24	1,165
R2	Fujifilm FinePix XP150	6.17 x 4.55	28	135
R3	LG Nexus 5	4.54 x 3.42	30.4	172

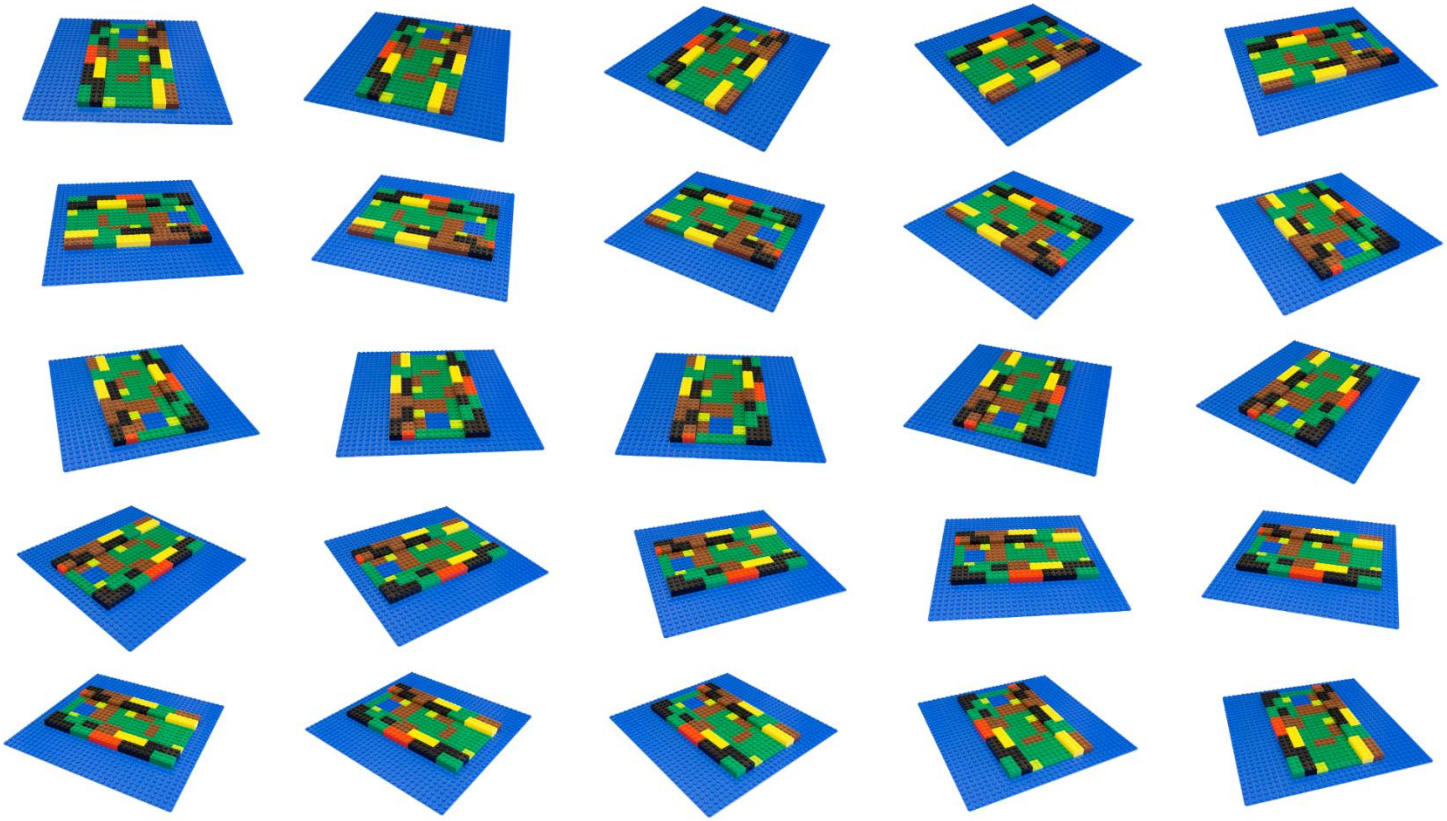

Figure 3.5: Example of how the image sequences were taken. The next image had at least 50% overlapping features from the previous throughout the sequence. The images were corrected in Adobe Lightroom to have balanced exposure throughout the target: brightness was decreased and shadow was compensated.

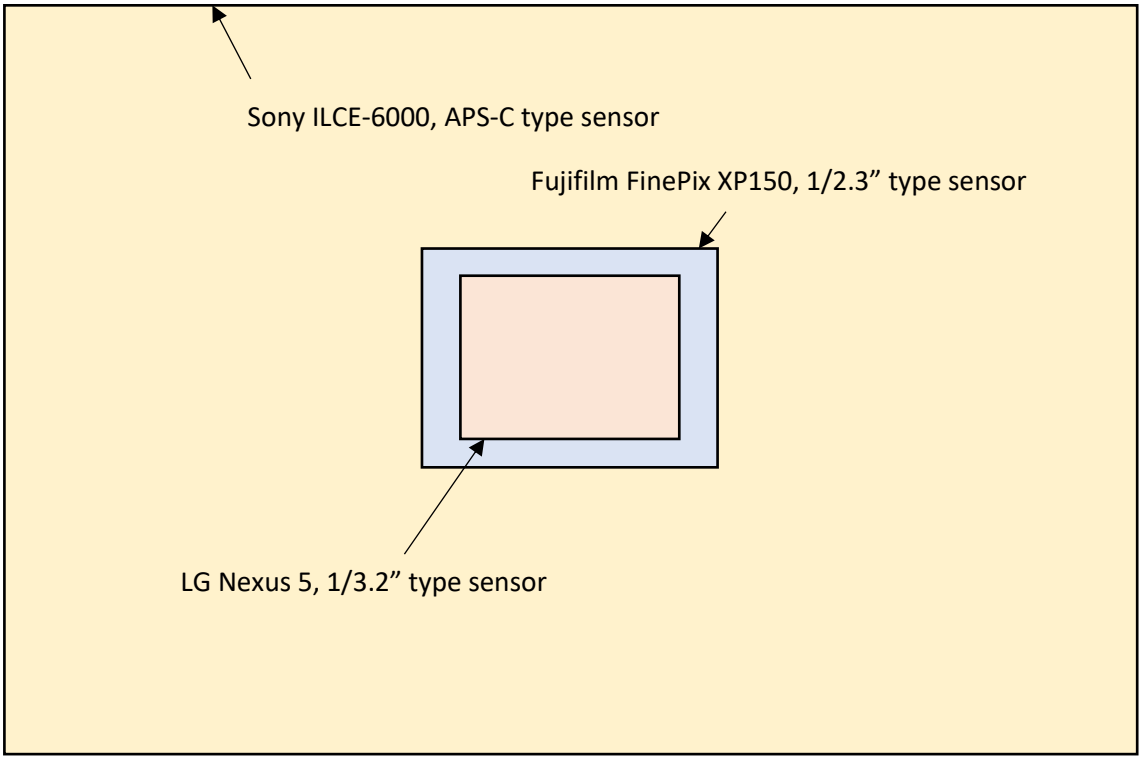

Figure 3.6: Comparison of sensor size in proportion

3.3.2. Image number

To examine the effect of image size on SfM-accuracy an image sequence of 40 images was taken with the LG Nexus 5, and the sequence subsampled to examine sequences containing 5, 10, 20, 30 and 40 images Subsampling was performed by maintaining an equal interval between images within a sequence. For example, for a sequence containing 5 images, images were selected with an interval of 8 images between each of the original 40 images; a sequence with 10 images had an interval of 4 images, and so on.

Unlike other tests, 400,000 subsampled point clouds from each image sequence were tested instead of 500,000 points. This was because 400,000 points was the maximum that could be gained from processing 5 images.

3.3.3. Image size

To test the influence of image size on SfM-derived point clouds' accuracy, an image sequence with a total of 50 photos from two different elevation levels around the LEGO® model was taken. The Sony ILCE-6000 was chosen to allow a wider range of image sizes to be used (this camera produces the highest image size of the three cameras). The original image size (RAW) from the camera ranges from 23,300 to 23,900 kilobytes (kb). The RAW images were then resized to produce images sequences with file sizes of 500 kb, 2,000 kb, 5,000 kb and 12,000 kb.

3.3.4. Image exposure

The image sequence containing 40 images that was taken with the LG Nexus 5. The images were processed in Adobe Lightroom CC to create two further SfM-derived point clouds; one with lower exposure and another with higher exposure. The lower exposure images were adjusted by decreasing the Exposure to +1.5, Contrast -100, Shadows +100 and Blacks +50 while the higher exposure images were adjusted to have Exposure -1.5, Contrast +100, Shadows -100 and Blacks -50.

Each exposure value refers to a light stop. When adding 1.5 exposure value, Lightroom simulates 1.5 times the amount of light the original image contains hence the adjusted image would be 1.5 times brighter than the original. An opposite effect

is applied when reducing 1.5 exposure value. The contrast, shadow and black values are in percentage. Adding or reducing these values simulates different values proportionally.

3.4. Experimental plot

An experimental plot consisting of a soil box, a rainfall simulator and overland flow generator was used to examine the effects of two things. Firstly, the effects of rainfall to microtopography of plot-scale soil surface. Secondly, the effects of hydraulics overland flow on particle transport and the effects flows do to soil surface, vice versa.

The soil box had a total length of 2.44 m, width of 1.22 m and depth of 0.4 m. The slope of the box could be adjusted via a simple jacking mechanism. At the upslope end was an overflow trough, with a length of 0.2 m that ran the full width of the plot, in which water entered via an inlet pipe in the bottom of the centre of the trough. This configuration allowed differing overland flow discharges to be generated over the plot and acted to reduce the turbulence of the water generated in the pipe before it flowed over the soil surface. At the bottom end of the soil box contained a second trough with 10 μm meshed-outlets, with a length of 0.2 m that ran the full width of the plot, allowing eroded sediment to be trapped, preventing the rainfall simulator and overland flow system from clogging. This trough also allowed the outflowing water to slowly drain through the outlet into a water tank, ensuring the water within the tank remained reasonably steady. These two troughs gave a soil box working length of 2.04 m by 1.22 m.

The rainfall simulator was based on a design by Parsons *et al.*, (1991) and consisted of two nozzles, separated by a distance of 0.27 m, supported at a height of 2.2 m above the soil surface. This configuration allowed the full coverage of the working section. The nozzles were axial-flow full-cone nozzles by Lechler, version 461.048.30.AK.00.0 for its ability to replicate droplet size and density similar to monsoon condition (Lascelles *et al.*, 2000). The nozzles were supplied with water from a water tank with a capacity of 200 litres via a 780W EINHELL GH-DP 7835 submersible pump. The flow rate, and thus the rainfall intensity, could be controlled via a simple valve on the pump outlet. The resulting rainfall drain down the plot and collected in the water tank.

To generate overland flows, the same pump and water tank system was used, and connected to the inlet pipe in the upslope trough. The overland flow discharge was controlled by a simple value on the pump outlet. The valve setting was calibrated to known discharge readings.

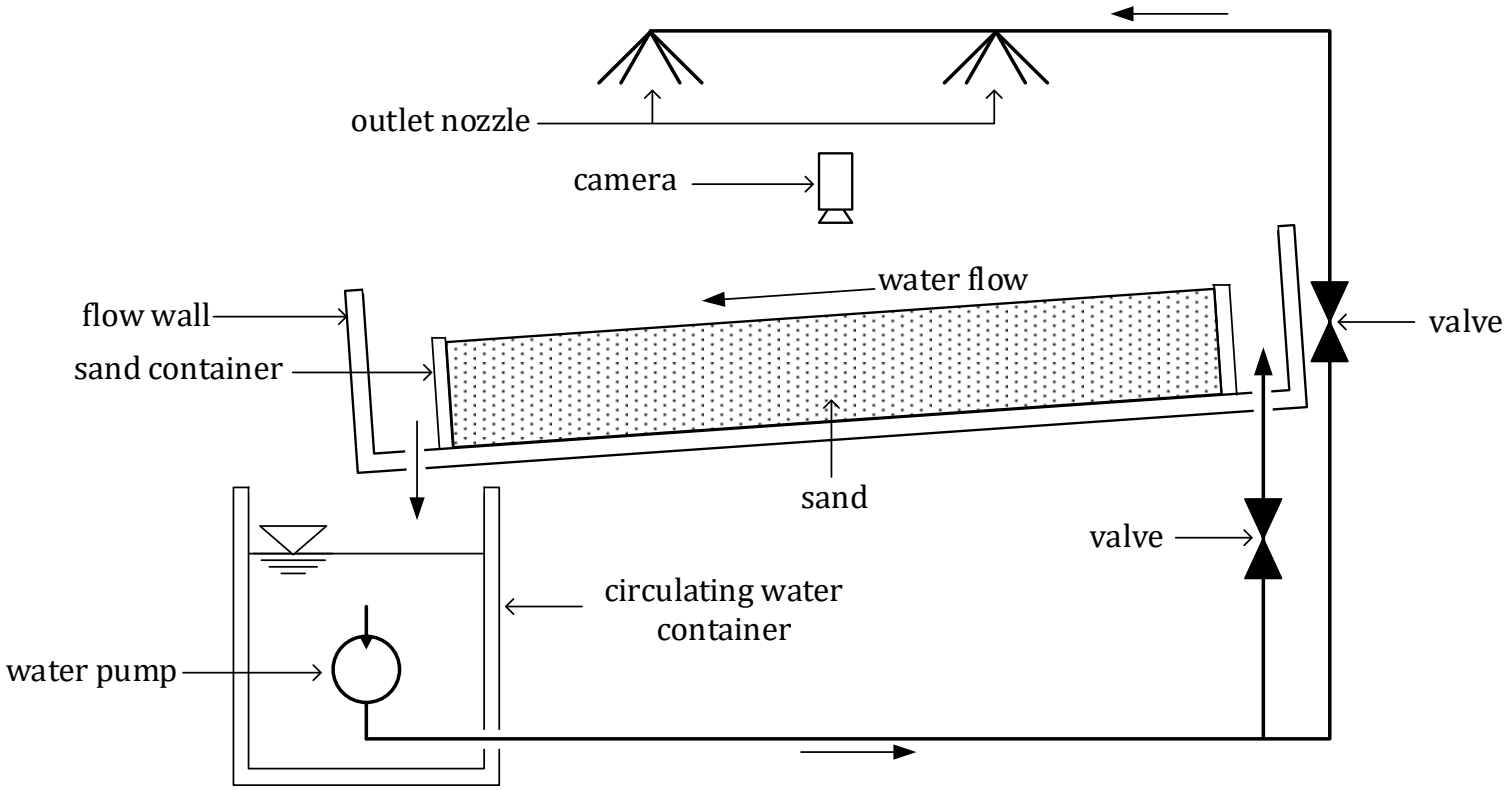

Figure 3.7: Schematic of the experimental plot, consisting of soil box, rainfall simulator and overland flow generator (adapted from Lascelles *et al.*,(2000).

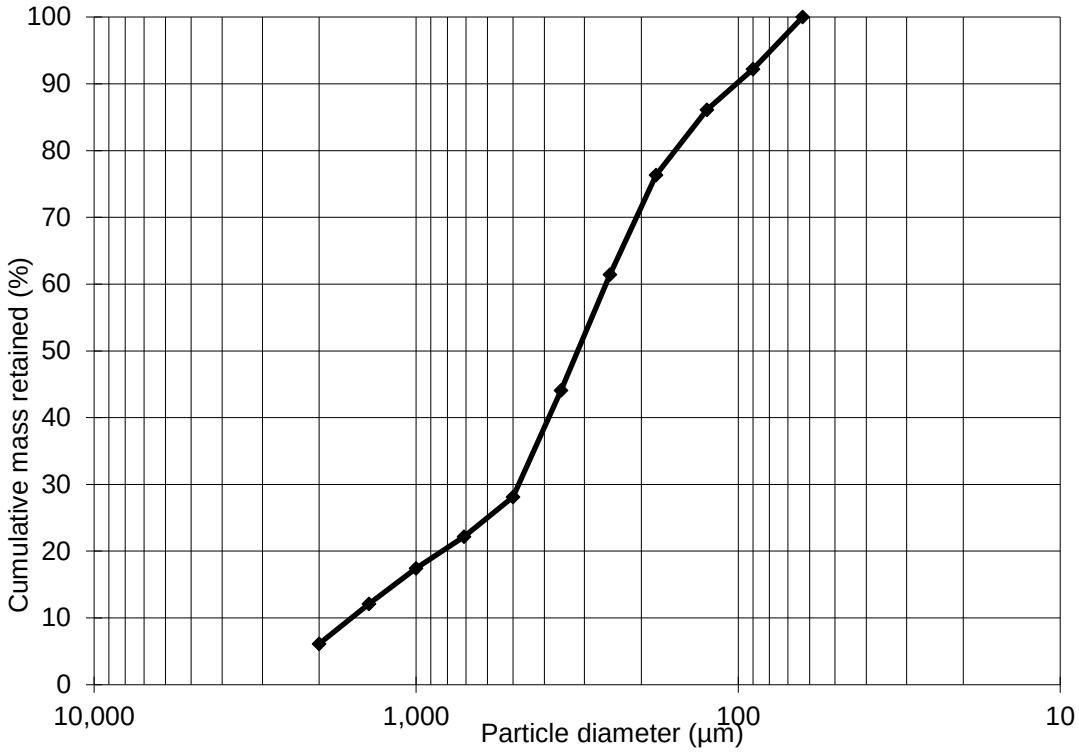

Figure 3.8: Grain size distribution

3.5 Rainfall-generated eroded surfaces

The soil used in the experimental programme was sourced locally from the University of Liverpool Ness Gardens, Wirral. The Wirral peninsula bedrock is dominated by Triassic sandstone which makes the soil in the area to be loamy and clayey soil (Natural England, 2014). The mixture had a D10, D50 and D90 of 0.10 mm, 0.32 mm and 1.59 mm respectively, and is classified as medium sand and poorly sorted with an arithmetic sorting value (σ) of 0.43 mm (Blott and Pye, 2001).

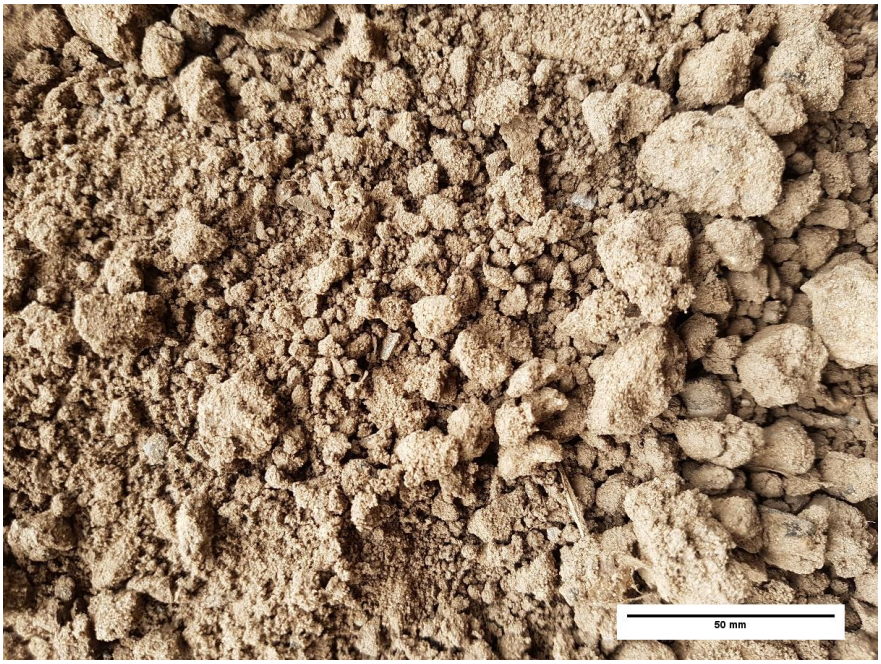

Figure 3.9: Soil used in the experimental plot after being dried.

The purpose of the first stage of the experimental programme was to create surfaces with differing microtopography using five different plot slopes using the same rainfall event Preliminary tests revealed rills form up at 20 minutes with a mean rainfall intensity of 110 mm hr^{-1}. This duration and intensity of simulated storm events were tested on the plot which slopes were set to 5, 8, 12, 15 and 20 percent adapted from several related studies (Kinnell, 2000; Abrahams *et al.*, 2001; Römkens *et al.*, 2002). These slopes were chosen since they are at reasonable height that the plot can acquire and are slopes that could be found in natural environment. Kinnell (2000) used slopes of 5, 10, 20 and 30 percent, and found that erosion starts to be seen at 5 percent slope. As a result, the value of 5 percent. In 2002, Römkens et al., (2002) has tested the effects of sediment yield of surfaces with 2, 8 and 17 percent slope and found that in order to achieve satisfactory results, higher and longer storm

events must be applied. Therefore, starting the experiment at a slope between 2 and 8 was considered (i.e. 5).

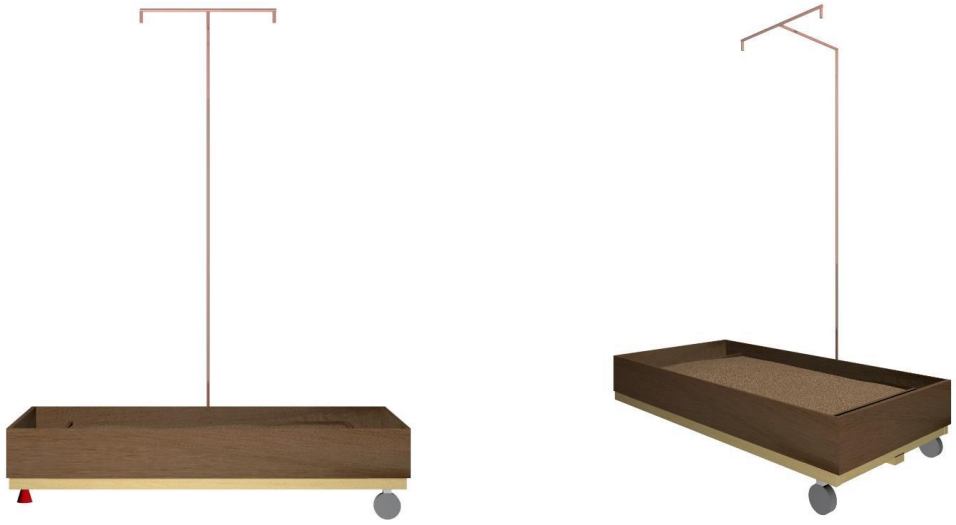

Figure 3.10: 3D-render of experiment flume

At 5 and 8 percent slope, rills tend to form later than 12, 15 and 20 percent slope which began to form after several minutes of rain and stabilises at about 15 minutes of rain. Thus this intensity and a rainfall duration of 20 minutes was chosen to ensure differing microtopography was formed at the different plot slopes. This rainfall event represents a short, high-intensity typically of convective storm. Each surface was given a test name, shown in Table 3.2: surfaces generated from 5, 10, 12, 15 and 20 percent were entitled S1, S2, S3, S4 and S5 respectively.

Table 3.2: Surface test name according to the slopes

Slope (%)	Name given
5	S1
8	S2
12	S3
15	S4
20	S5

After the 20 minute rainfall ceased, the DEM of the surface was measured using SfM (see section 3.2), and the surfaces fixed for the final stage of the experimental programme, the overland flow tests. The purpose of fixing was to prevent erosion in these tests and ensure the microtopography was the same for all the overland flow conditions. Unlike the semi-permanent/permanent techniques used by others(Vanoni and Nomicos, 1959; Khalil, 1972; Kashyap *et al.*, 2010) where the hardenings use mixtures of chemicals to stabilise the surface, the method chosen was far simpler, using Everbuild 502 All Purpose Weatherproof Wood Adhesive. The adhesive was mixed with water in a ratio of 1:1 and sprayed over the surfaces, and left to dry overnight. After leaving the adhesive to dry, black waterproof colour spray was used to spray over the surface, and turn the surface darker. This procedure was used to produce a high contrast between the background and the imaged particles for the hydraulics measurements made using Particle Tracking Velocimetry (PTV), which is key for producing accurate results (Thielicke and Stamhuis, 2014).

3.5. Microtopography and surface roughness

The surface roughness and topographic conditions were identified using Structure-from-Motion. Since the results presented in chapter 4 reveal no significant difference in the level of accuracy between the different types of camera, a 12 megapixel mobile phone camera in the Samsung Galaxy S7 Edge was used for convenience. For every surface image sequences were collected before and after the rainfall simulation. In total, ten sets of image sequences were acquired and processed. Since the experimental plot has a larger area than the LEGO® bricks, a larger number of images were taken. Each image sequence contained between 110 and 136 images to cover the whole experimental area (Table 3.3). After processing the image sequences, using the same procedure as the accuracy test, each SfM-derived point clouds was aligned to share the same datum and coordinate system. Additionally, each set of point clouds had its mean and linear trend removed. This process was done using a Matlab function, Detrend.

In Matlab, Detrend is a function (Mathworks, 2017) which subtracts offsets of linear trends. The inputted data are computed. Mean values from each dataset are subtracted. By applying this function into the surface data, the biased slope data were eliminated. This can be examined from an example in Figure 3.11.

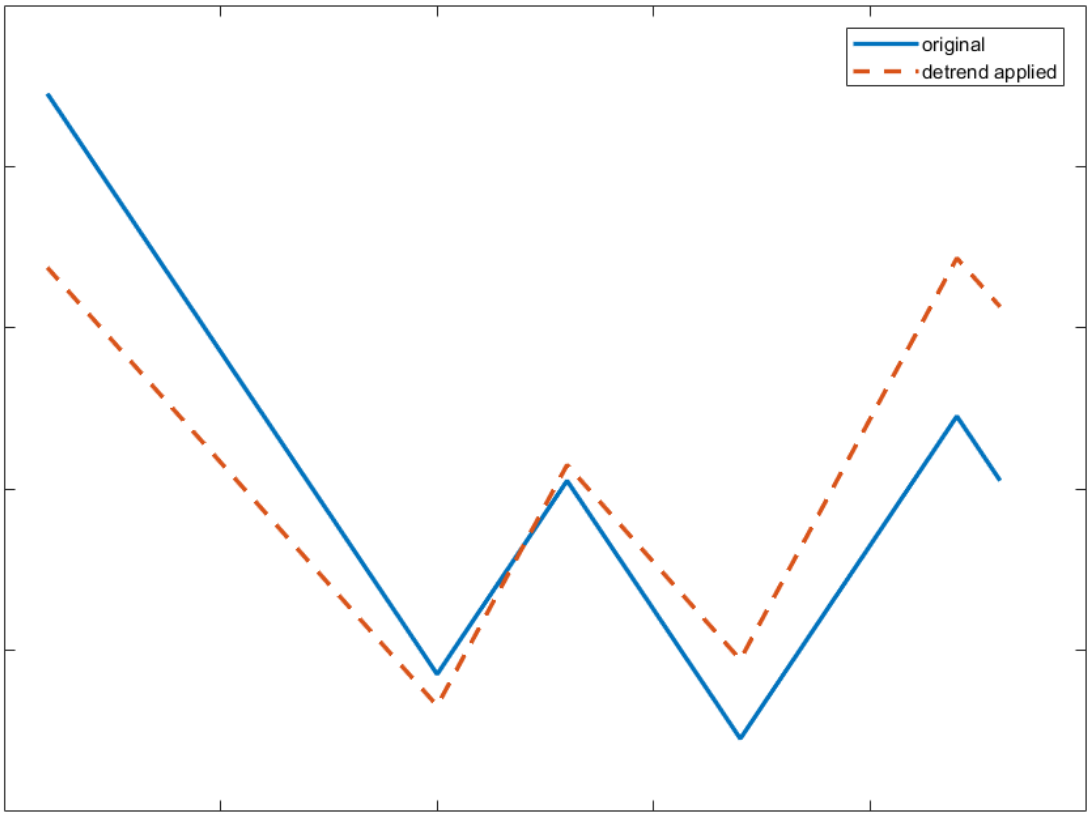

Figure 3.11: Example of Detrend function after being applied to a set of data

Table 3.3: Number of images used to process each surface SfM-derived model of the before and after simulated rainfall

Slope (%)	Number of SfM images	
	Before	After
5	136	120
8	114	122
12	110	125
15	115	127
20	113	112

3.6. Overland flow hydraulics

3.6.1 Introduction

Particle Tracking Velocimetry (PTV) was used to measure the surface velocity fields of the overland flows generated over the experimental plot. These measurements were conducted after each rilled surface was generated and fixed. For each surface three overland flows discharges were generated (Table 3.4), each representing differing upslope. Therefore, in total fifteen overland flow tests were conducted. In each test, the surface velocity was measured for 120 seconds (Buffin-Bélanger and Roy, 2005).

Unlike Structure-from-Motion where the quality of the result could be contingent by the equipment, software or experimental environment, PTV is processed in a less complicated process. Initially, the software detects bright pixels of each frame then calculates the displacement of individual pixels using cross-correlation analysis. As the process of the analysis is statistic, it is highly reliable. Therefore, further validation is not required.

Table 3.4: Summary of experimental conditions for the overland flow experiments. The test name incorporates the slope number, and discharge category: l (low) – 0.0022 m^3 sec^{-1}, m (medium) – 0.0044 m^3 sec^{-1} and h (high) – 0.0064 m^3 sec^{-1}.

Test name	Slope (%)	Discharge (m^3 s^{-1})
S1l		0.0022
S1m	5	0.0044

Test name	Slope (%)	Discharge ($m^3 s^{-1}$)
S1h		0.0064
S2l		0.0022
S2m	8	0.0044
S2h		0.0064
S3l		0.0022
S3m	12	0.0044
S3h		0.0064
S4l		0.0022
S4m	15	0.0044
S4h		0.0064
S5l		0.0022
S5m	20	0.0044
S5h		0.0064

3.6.1. Particle Tracking Velocimetry

Particle Tracking Velocimetry (PTV) is a particle tracking spatially-distributed velocimetry technique commonly used in environmental hydrodynamics and fluid dynamics (e.g. Malik *et al.*, 1993; Parsons *et al.*, 2014; Evans *et al.*, 2016). Unlike Particle Image Velocimetry, which often requires double-frame high-speed cameras and double-pulsed lasers to illuminate and cross-correlates the movement of an assemblage of neutrally-buoyant particles between image pairs (cost ~£120k), PTV measures the trajectory of individual particles though the whole sampling period. Most commonly in environmental hydrodynamics this involves tracking buoyant particles on the water surface to resolve the surface velocity field in 2D. Thus PTV is a less complex technique than PIV and can be performed with relatively inexpensive single-frame cameras and illumination provided by a white light source,

such as a consumer grade video camera and a LED lamp (cost ~£300). Therefore, from a practical perspective, SfM and PTV can be fused using the same photogrammetric equipment and at a low cost. Despite having potentials to perform measurements at microtopography scale, there has been little amount of work in using PTV in shallow overland flow; one being the work from Lascelles *et al.*, (2000)

3.6.1.1. Apparatus

a. Camera

A GoPro Hero 4 Black version was used in the experiments because it is capable of capturing sufficiently high frame rates to ensure there is negligible particle aliasing (blur) between each image pair. A GoPro Hero 4 Black is an action camera that is able to capture up to 120 frames per second videos depending on the resolution of the video. This camera has the added advantages of being low cost, waterproof, portable and proven as a capable camera for PTV (Detert and Weitbrecht, 2015). The camera settings used in the overland flow experiments are presented in Table 3.5.

Table 3.5: GoPro Hero 4 Black capturing settings

Setting	Value
Resolution	1920 x 1440 px
Frame rate	80 fps
Shutter speed	1/80 sec
White balance	5500

Setting	Value
ISO limit	6400
Sharpness	Low
Exposure compensation	0
Focal length	17.2 (35 mm equivalent)

Although the camera was able to capture 120 frames per second, this study uses the second highest frame rate of 80 frames per second to allow recording at a higher resolution (1,920 x 1,440 pixels vs. 1440 x 1080 pixels). This resolution was chosen to ensure the resolution was sufficient to detect the seeding particles used in this study. The camera was placed at the center of the plot at a height of 0.8 m, and angled parallel to the surface. A wide angle lens enabled the camera to view the entire working area of the plot. The total imaged area, with fisheye effect (visual distortion), was approximately 2,400 x 1,300 mm.

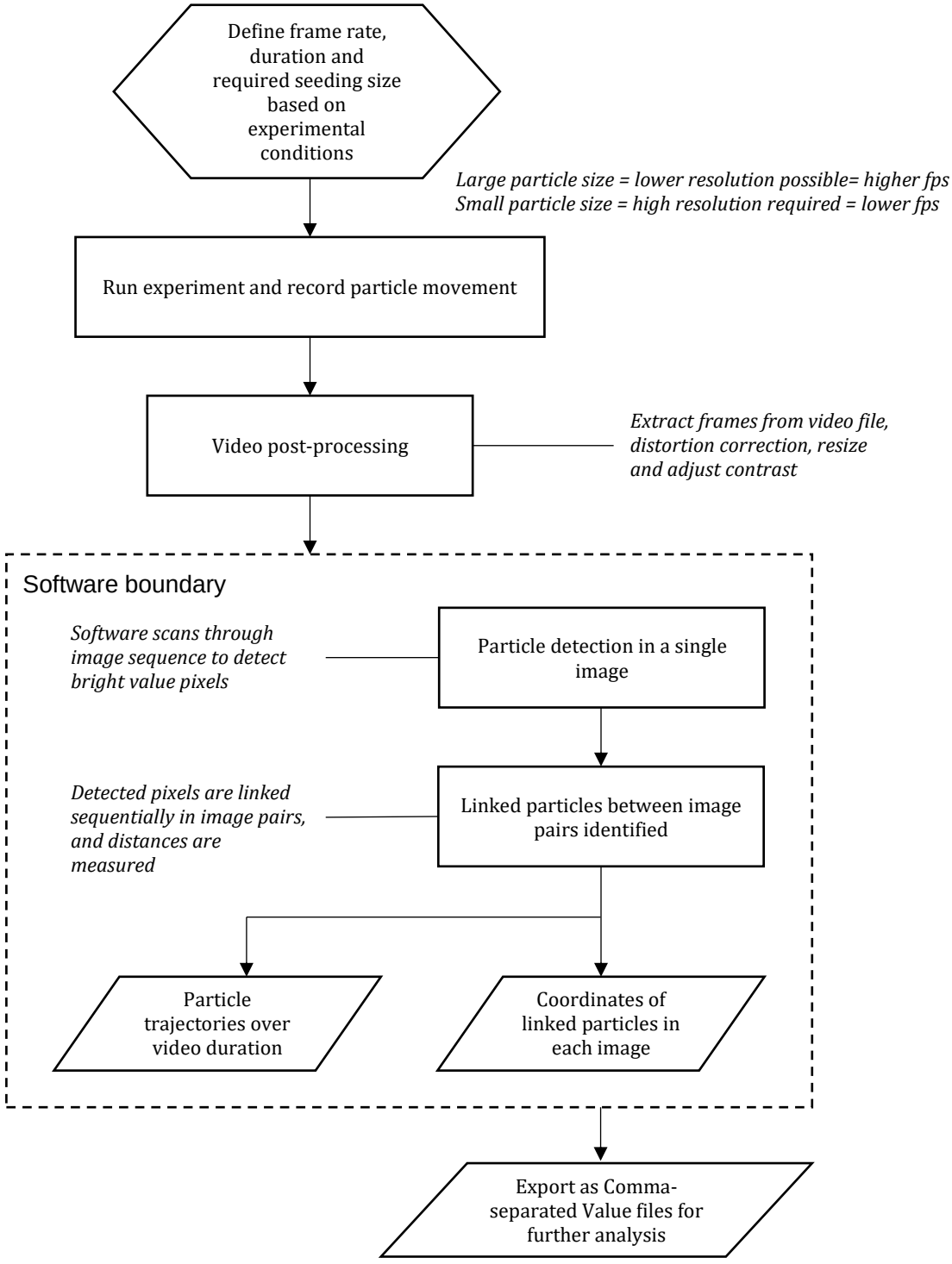

Figure 3.12: PTV processing procedure

Figure 3.13: Unprocessed image extracted from the recorded video with fisheye effect presented

b. Seeding particles

Buoyant, polyethylene particles varying in size from 2-5 mm in diameter were used to see the water surface. This size ensured, each particle had a size between two and five pixels. A minimum size of two pixels is required for accurate particle identification (Thielicke and Stamhuis, 2014). The size presented in the frames were sufficient of being detected from the tracking software The seeding material is particularly well-suited for PTV because it is hydrophobic and not electrostatic, meaning that individual particles do not stick to one another. These

properties prevent the mismatching of linked particle movement between image pairs. The flow was seeded with particles continuously at the upslope end of the plot and across the full width to ensure a thorough distribution across the imaged area.

3.6.1.2. Video post-processing

The procedures of PTV used in this study is presented in Figure 3.12. The wide angle lens produced a fisheye effect, which was corrected before PTV processing took place. The individual frames were extracted from the raw video files and each frame was processed in Adobe Photoshop CC 2017 (Adobe Systems, 2017b) to remove the fisheye distortion, and enhance the contrast. The contrast was adjusted to reduce the background brightness to nearly reach black pixel values and increasing the brightness of the particles to nearly white pixels, to enhance particle detection. The images were then cropped to have a resolution of 1,440 x 1080 pixels (75 percent of the original frame size), to focus only on the areas with flow activity.
Software processing

The PTV software used to process the particle movement was ImageJ (Abràmoff *et al.*, 2004) with a plug-in PTV component called Mosaic (Sbalzarini and Koumoutsakos, 2005). Mosaic is able to detect particles in a single frame in an image sequence and analyses the cross-correlation of each particle to the sequential frame, then reports the displacements of the particles. Displacement is calculated from the change in the coordinates X and Y of individual particles from one image to the next. The user can control the settings for particle detection in individual images and the settings for the detection of linked particles between image pairs (i.e. how the

software determines whether a particle detected in two sequential images is likely to be the same particle).

Figure 3.14: Processed frame ready to be used in the tracking software.

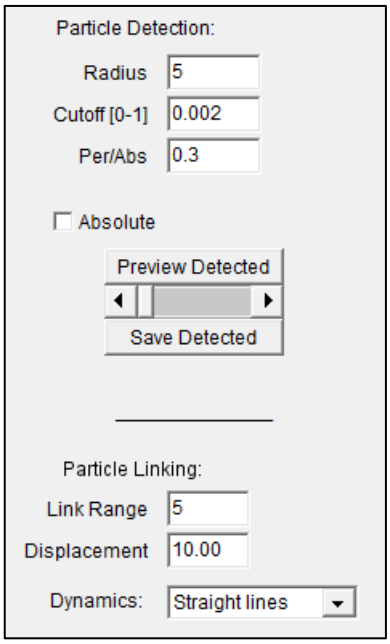

Figure 3.15: Settings used

The particle detection is based on three settings (Figure 3.14): Radius (maximum particle size in pixels), Cutoff (the distance between particles in percentage), and Per/Abs (the pixel sensitivity the software detects for particles). The settings used are displayed in Figure 3.14. As described above the seeding particle size ranged from two to five pixels. Therefore, the 'Radius' detection was set to five pixels in order to prevent software algorithm to detect larger objects. The 'Cutoff' and 'Per/Abs' setting were optimized using the collected imagery and set at 0.002 (1 being the distance at 100 percent resolution or 1440 pixels in this study) and 0.3 (i.e. 30 percent to the contrast of the scene) respectively. Figure 3.16 shows an example of particle detection according to the settings used. The image shows the PTV software was able to discriminate clearly between the white areas of the soil surface and the seeding particles. Particle linking was based on three settings: Link Range (maximum expected pixel displacement of a single particle between image pairs, Displacement (the value to detect the same particle despite particle rotation which may cause shifting size) and Dynamics (the characteristics of the trajectories). The 'Link Range' was set to 5, according to preliminary tests that found that the use of 5 pixels allowed particles that travelled with higher velocities to be linked between image pairs (a low setting does not sufficiently detect high velocities, and a high setting spuriously detects other particle movements). Thus, the software keeps

the track of a particle that moved within 5 pixels around the pre-detected position. The 'Displacement' was set to 10 frames, so that rotating or shape-changing-particles are still connected even though they disappear for up to 10 frames. The 'Dynamics' of the particle behaviour was set to "Straight line" since the particles travel typically from upstream to downstream. An example of particle tracks using these settings can be seen in Figure 3.17, showing the software can detect simultaneously particle trajectories and new particles..

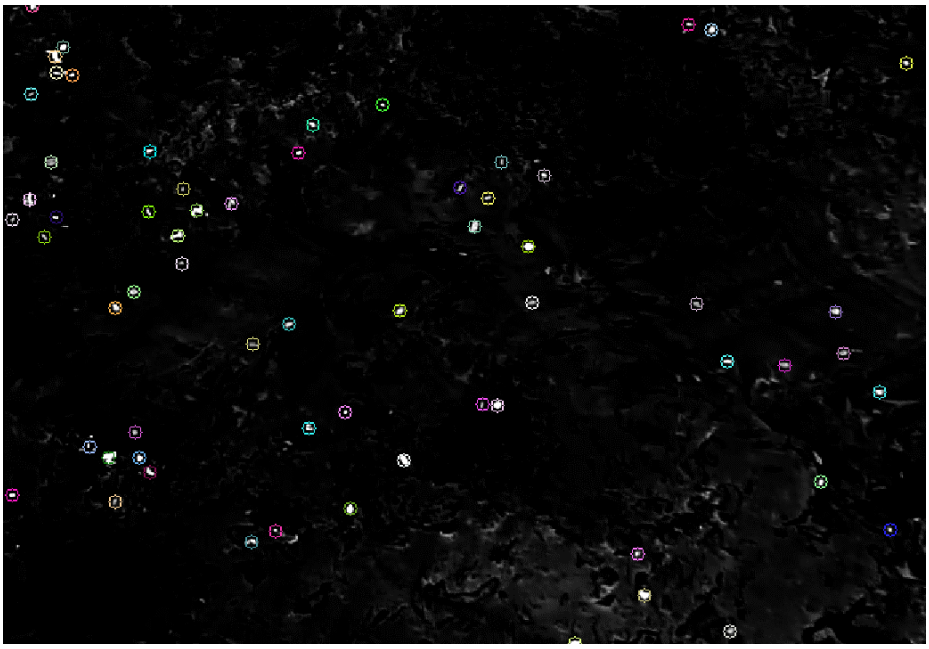

Figure 3.16: An example of particle detection

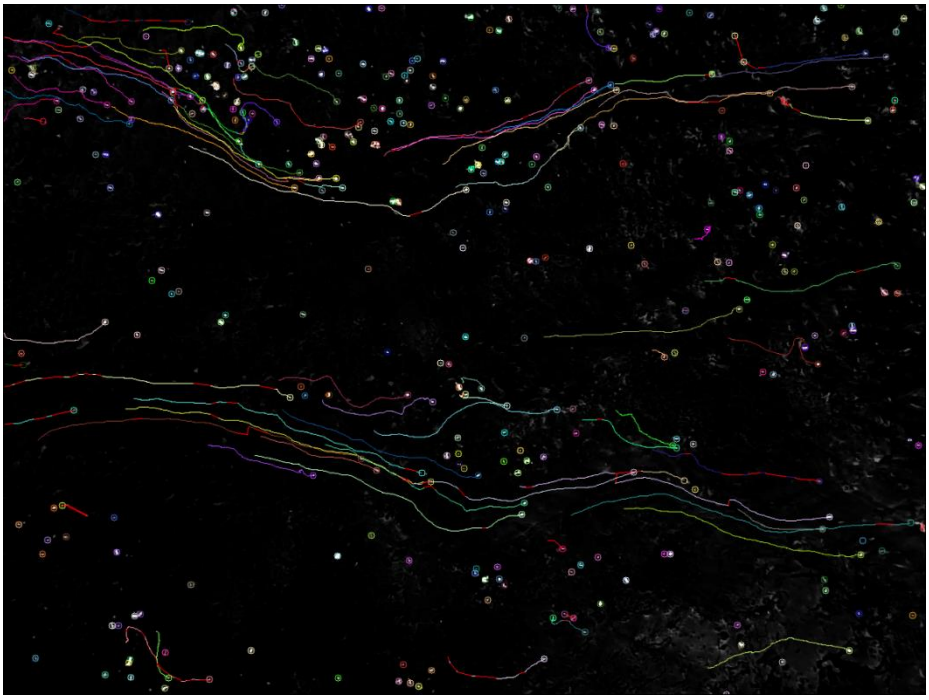

Figure 3.17: An example of particle trajectories resolved by the PTV software.

3.6.1.3. PTV analysis

After image processing with Mosaic, the output data was further analysed in Matlab R2017a (Mathworks, 2017). These processes can be seen in Figure 3.18. Firstly, the pixel coordinates exported from ImageJ were calibrated to match the physical coordinates of the plot; one pixel equaled 1.3 mm. Secondly, each particle's displacement was calculated by detecting the change in the particle coordinates between two images. From this calculation, streamwise (u) and lateral (v) velocities of particles in each frame were acquired, using the time separation between images (0.0125 seconds). This process produced a discontinuous map of 2D velocities over the plot for the entire sampling period, with the mapped locations determined by the trajectories of the identified particles. To allow a direct comparison of velocity fields

between tests, this map was interpolated onto a regular grid (cell size 800 mm 1,100 mm).

a. Applying masks

Since this study measured the velocity over rilled surfaces which contain areas without any flow. These areas were masked to avoid these areas introducing a zero velocity bias to the interpolated velocity maps. The masks were created by using 480 images of the processed frames. The 480 frames were chosen from the full 9,600 frames by using every 20th frame. The maximum pixel values of the frames, which in this case are the bright pixels representing the seeding particles, were calculated. In Adobe Photoshop CC 2017 (Adobe Systems, 2017b), a stack of only these maximum pixel values was performed to produce a stacked image illustrating where the flow was detected. An example of a stacked image is shown in Figure 3.19a. This process involved identifying only the black and dark grey pixels of each of the 480 images using a threshold set at 100[3]. The staked image was created by overlaying each of these images onto one another. White pixels were then selected adding 10 neighbouring pixels. These pixels were then converted into a flow mask leaving black, unselected pixels out. This mask was created at a resolution equal to that of the desired interpolated velocity grid (Figure 3.19b), and thus had a coarser resolution than the flow areas identified in the staked image.

3 Value of black and white scale ranges between 0 to 255 when 0 equals to black pixels and 255 white pixels. When the threshold is selected to a specific value, in this case 100, the pixels that are included in the selection ranges between 0 and 100 in the black and white scale.

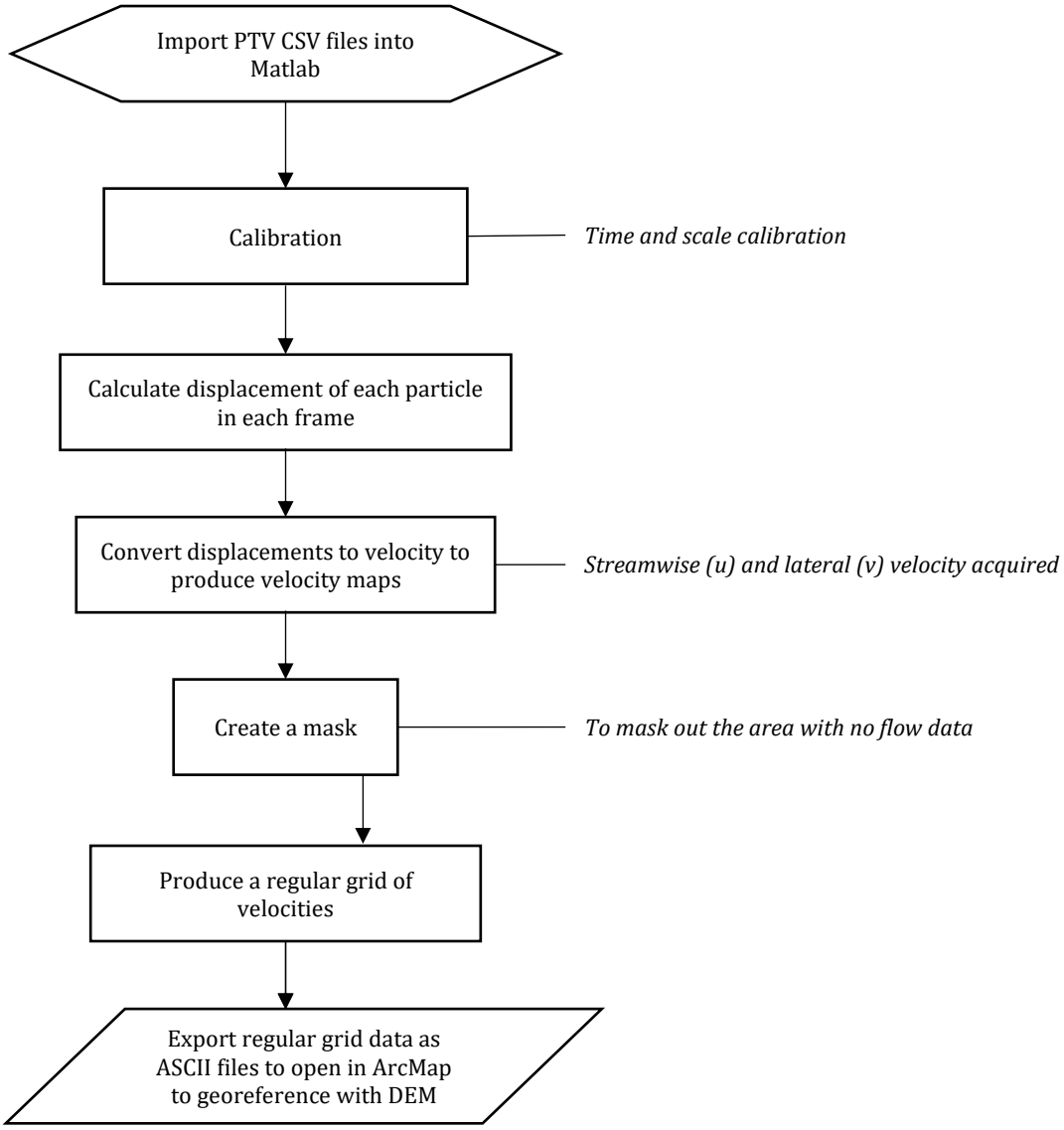

Figure 3.18: Process of analysing the data after exporting from ImageJ Mosaic

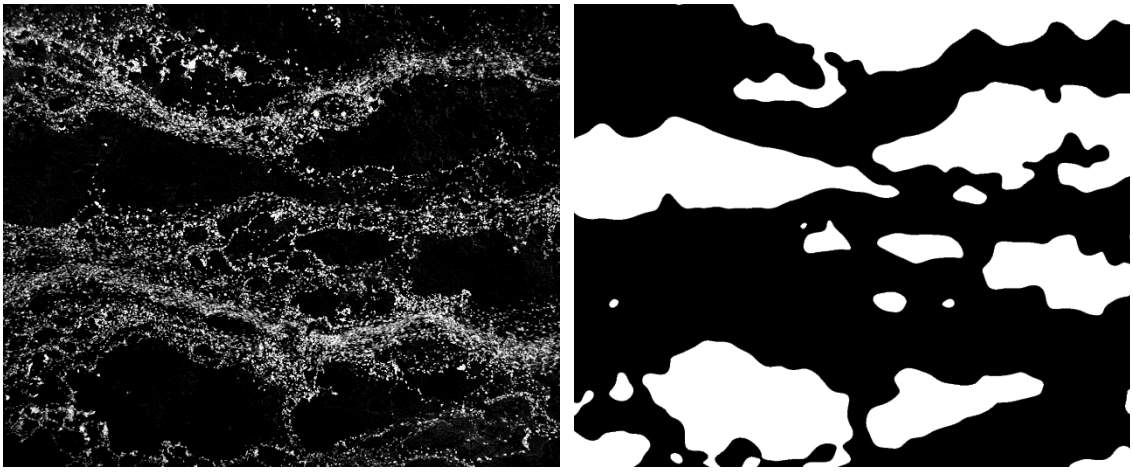

(a) (b)

Figure 3.19: (a) The result after statistically stacking 480 images to gain the maximum pixel value of each frame. (b) The mask resulting from this stacking. Areas in white are masked out areas (i.e. areas with no flow data) while the black areas are areas left where flow data was present.

3.7. Probability distribution functions

The sensitivity of surface and flow properties places crucial significance on modelling more complex attributes (Parsons and Wainwright, 2006; Smith *et al.*, 2011). Most surface and flow properties are zero or positive, and are generally highly skewed. As a result, the variables cannot be justified merely by mean, standard deviation, median or interquartile range. Therefore, the variables can be defined more effectively by specific distributions (Evans *et al.*, 2000).

In later chapters, surface and flow properties such as surface elevation, surface roughness, velocity, hydraulic resistance were observed using distribution functions. In order to decide which distribution the datasets fit best, the datasets

were put into Minitab 17 for Goodness-of-Fit test (Minitab, 2017). The Goodness-of-Fit test analyses the datasets by fitting them into various distributions. Each fit is parameterised by Anderson-Darling and P value. Distributions considered for best fit are based on two factors: low Anderson-Darling values and distributions with a small number of parameters.

Anderson-Darling, AD, is a statistical test to find the best fit for a set of data. The test focuses on the tails of the distribution and makes use of the specific distribution in calculating critical values. The Anderson-Darling test is defined as:

$$A^2 = -N - S \tag{3-1}$$

where

$$S = \sum_{i=1}^{N} \frac{(2i-1)}{N} [\int F(Y_i) + \int (1 - F(Y_{N+1-i}))] \tag{3-2}$$

F is the cumulative distribution function of the specified distribution.

3.8. Flow components

3.8.1. Inundation height

In order to acquire hydraulic radius, the inundation height (h) should be known. Unlike river channels where flow depths can be determined by the flow level in relation to the channel bank, the water level cannot be so clearly defined in

interrill and multi-threaded rill flows (Govers *et al.*, 2000; Smith *et al.*, 2011). Thus, the measurement the depth of flow poses a technical challenge, and has in the past generated large measurement errors (Govers *et al.*, 2000). Smith *et al.* (2011) proposed a method where inundation height can be measured throughout the channel using a terrestrial laser scanner. The proposed method employs five rules for rill flow:

1. The depth of the flow equals the surface elevation at end-points of each cross-section within the rill.
2. The flow level can be estimated by a linear interpolation between these two end-points.
3. Where dry areas protrude from the centre of a cross-section, the edges of the dry areas are treated as end-points.
4. Where surface peaks above the water level, the peaks are treated as the end-points.
5. Water level cannot be below soil surface level.

These rules were tested in a field experiment that involved simulating flows through a single rill. The test is illustrated in Figure 3.20. The modelled inundation height at a cross section shows an unrealistic change in water level. Though this model holds great potential to evaluate inundation height in rills, the application of it is limited to well-channelised flows and situations in which depths are much higher than the surface roughness height. Thus the technique has limited value for interrill and multi-threaded flows.

As a result, another approach to estimate the inundation height was applied. In this test, the inundation height was estimated from known discharge rates and area of flow at cross-section. The mean inundation height, <*h*>, of each flow was calculated using method similar to Parsons *et al.* (1996) and Govers *et al.* (2000) where <*h*> is relative to mean channel width, <*W*>, and mean area, <*A*>, of the flow. It is calculated from the equation:

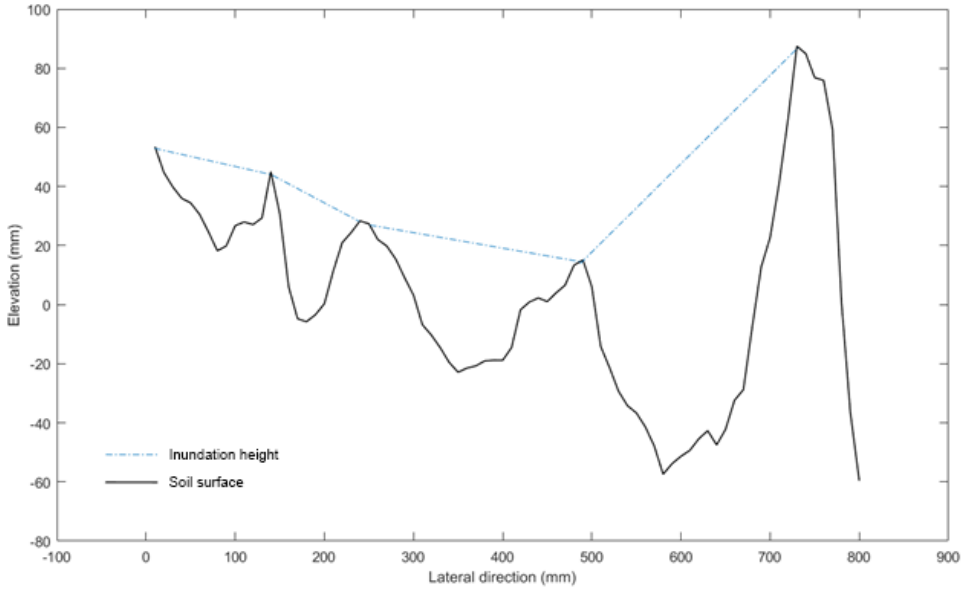

Figure 3.20: *Inundation height measurement using Smith's (2011) depth model*

$$\langle h \rangle = \frac{\langle A \rangle}{\langle W \rangle} \tag{3-3}$$

<*A*> was acquired from the equation:

$$\langle A \rangle = \frac{Q}{\langle V \rangle} \tag{3-4}$$

where Q is flow discharge and $\langle V \rangle$ is the mean velocity.

CHAPTER 4
The accuracy of Structure-from-Motion in the measurement of microtopography

4.1. Introduction

The purpose of this chapter is to examine the potentials and measurement accuracy of Structure-from-Motion (SfM) in the resolution of microtopography. Four factors that can potentially affect the measurement accuracy of Structure-from-Motion (SfM) which are (1) camera sensor size, (2) the number of acquired images used to derive SfM point clouds, (3) image resolution, and (4) image brightness were examined. The purpose of these tests was to establish the camera and image properties required to optimise measurement accuracy and provide valuable guidance on the use of Structure-from-Motion. Establishment of these properties was crucial for producing, reliable, high-resolution digital elevation models (DEM) of the soil surface that can be used to institute the link between soil micro-topography and overland flow hydraulics in succeeding chapters.

As described earlier in the previous chapter, the LEGO® model structure used to examine in this study was built using bricks of varying colour, and constructed to produce a linear channel that had a depth-to-width ratio of 7, which is a common ratio observed in natural rills (Shit and Maiti, 2012). This ratio was taken so that the effect of shadowing, that would be a potential problem when measuring rilled

surfaces, could be explored. There is no suggestion the model is representing a natural feature.

In this chapter, some photography terminology are used. Footnotes are provided to define the terms. For example pixel noise, exposure, contrast, dynamic range, etc.

4.2. Effect of sensor size

Figure 4.2 shows the images and detail of the JPEG files directly exported from the cameras without any post-processing adjustments. It can be seen from the 100% zoomed images that the JPEG acquired from the Sony ILCE-6000 (R1) is sharp and has low pixel noise[1]. The JPEG from Fujifilm FinePix XP150 (R2) contains a substantial amount of pixel noise and the contrast between colours is relatively poor. The JPEG from the LG Nexus 5 (R3) contains an adequate degree of pixel noise, but not as much as R2. The contrast[2] between colours produced by R3 is represented better than by R2, but not as well as by R1. Moreover, the JPEG also shows over sharpening[3] which improves the separation between pixels clearly.

The histogram showing the distribution of Red, Blue and Green (RGB) values reveals further that sensor size has a strong effect on the dynamic range. First, R1,

---

[1] Pixel noise are uneven results of pixel color distribution. This usually occurs when camera is set to high ISO and images taken in dark scenes.

[2] Contrast is the intensity of pixel color. High contrast images are dark in tone while low contrast are the opposite

[3] Sharp (edging) is the cut-off between different Red, Blue and Green pixel values. Sharp images are those that have high distinction of different pixel values.

the largest sensor size is capable of acquiring a wider light dynamic range[4]. Much of the details of the LEGO model was contained within this range, although some red values are over exposed[5]. Second, the distribution of RGB of R2 shows a well distributed of dynamic range. However, the distribution shows an over exposure of blue pixels. Third, the RGB distribution of R3, the smallest sensor size, is the poorest when compared to R1 and R2. Most red pixels are under exposed while blue pixels are mostly over exposed.

However, rather interestingly, despite these differences in the images, a comparison of the accuracy of three derived point clouds shows that each camera performs very well in replicating the LEGO® model. Each cloud had more than 99% of the elevations within ±1 mm of the elevations from the CAD model. Thus at an accuracy level of ±1 mm distance, the effect of sensor size is minimal. However, when a comparison at a ±0.75 and ±0.5 mm accuracy level, shows that R3 had the highest percentages of points within these levels, and R1 and R2 differ by a small degree. Thus, rather contradictory, the smallest sensor size produces a point cloud with the best performance the reason being is unclear.

To explore this effect further, and to provide possible explanations, boxplots of the elevation differences are shown. Figure 4.3 shows that R3 has the most points contained within ±1 mm distance while R2 has the largest amount of point clouds

[4] Dynamic range is the range of light tone. If a camera can capture high dynamic range, it can contain more detail in darker and brighter tones.

[5] Over exposure is the stage where pixels are in the higher region of the RGB value scale. While under exposure is the opposite stage. Over exposed images are brighter than those under exposed.

further than ±1 mm. R2 also contained the most outlying data comparing to R1 and R3.

To illustrate the effect of sensor size, the SfM-derived point clouds of elevation differences between the point clouds and the CAD model are presented in Figure 4.3. These are able to show quite why one camera performs better than another at the higher levels of accuracy. The derived point cloud of difference derived from R1 shows high elevation differences in the measurement of the brick knobs. These differences resulted from the high light contrast in the raw JPEG files. The SfM-derived point cloud acquired from R2 contains a substantial amount of noisy pixels (uneven). This was reflected in the JPEGs that contained an extensive amount of pixel noise. The model acquired from R3 has the most accurate result. The shadow and elevation difference around the brick knobs did not affect the accuracy of R3 as much it did to R1. This is due to the lower contrast in R1's JPEG files.

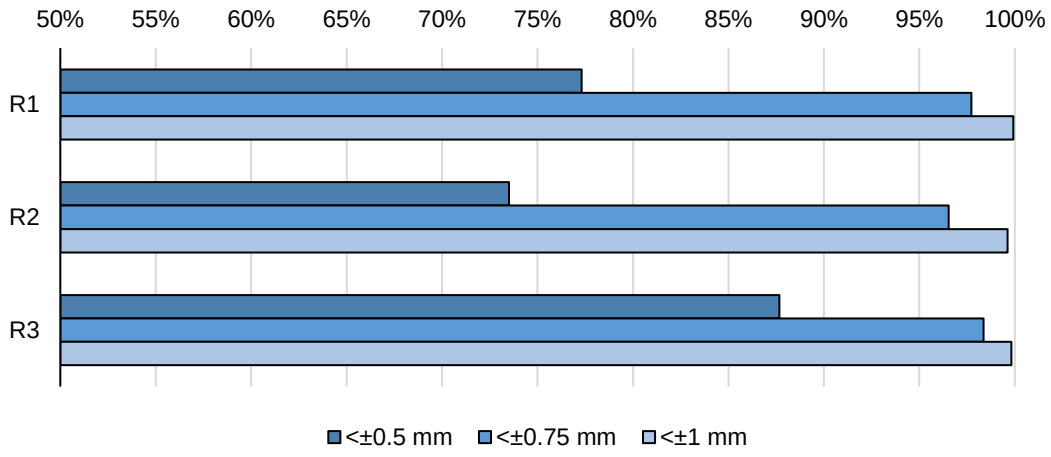

Figure 4.1: Percentage of points within a set accuracy level.

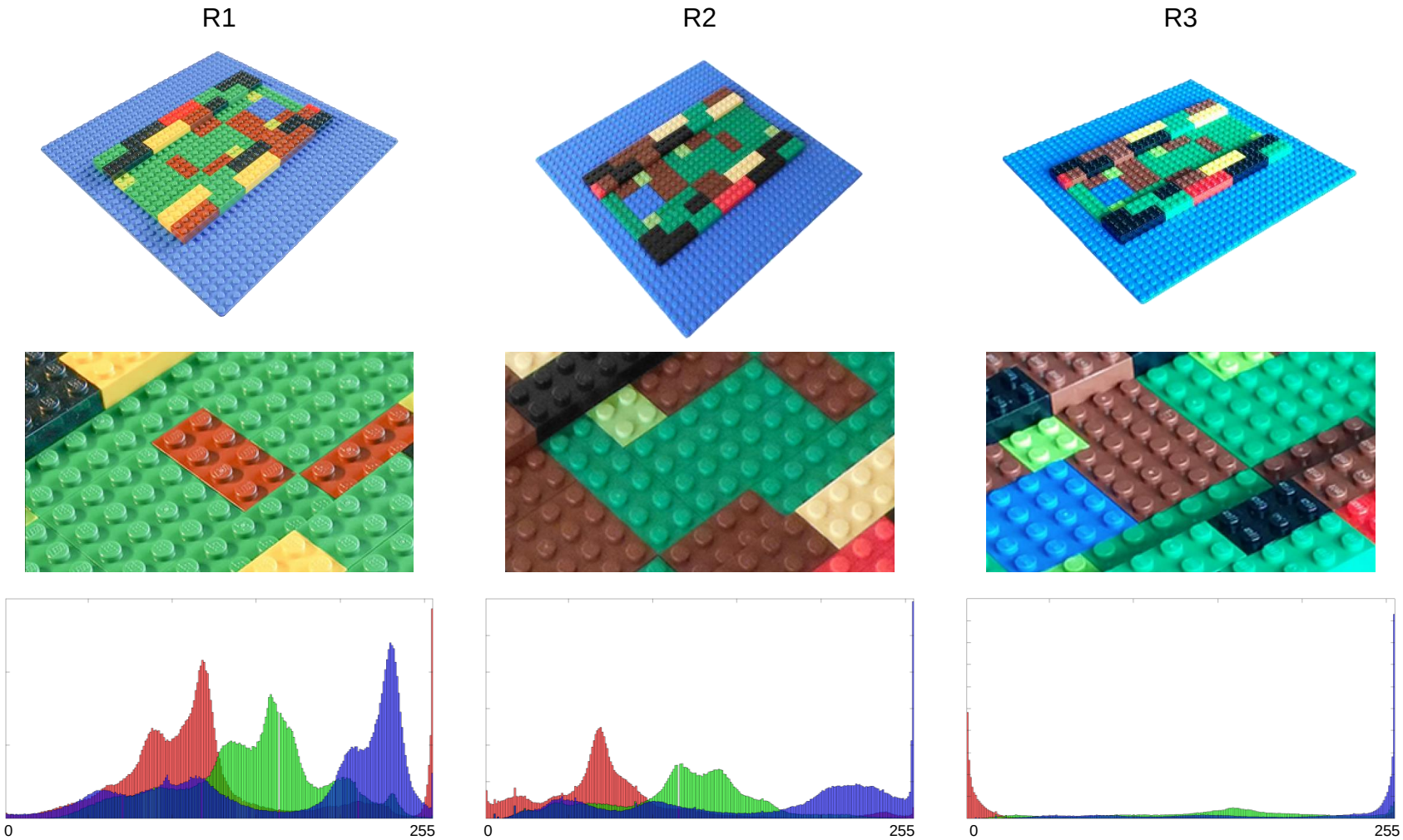

Figure 4.2: (Top row) Unprocessed JPEG image samples imported from each camera. (Middle row) Images zoomed at 100%. (Bottom row) Distribution of Red, Blue and Green pixels.

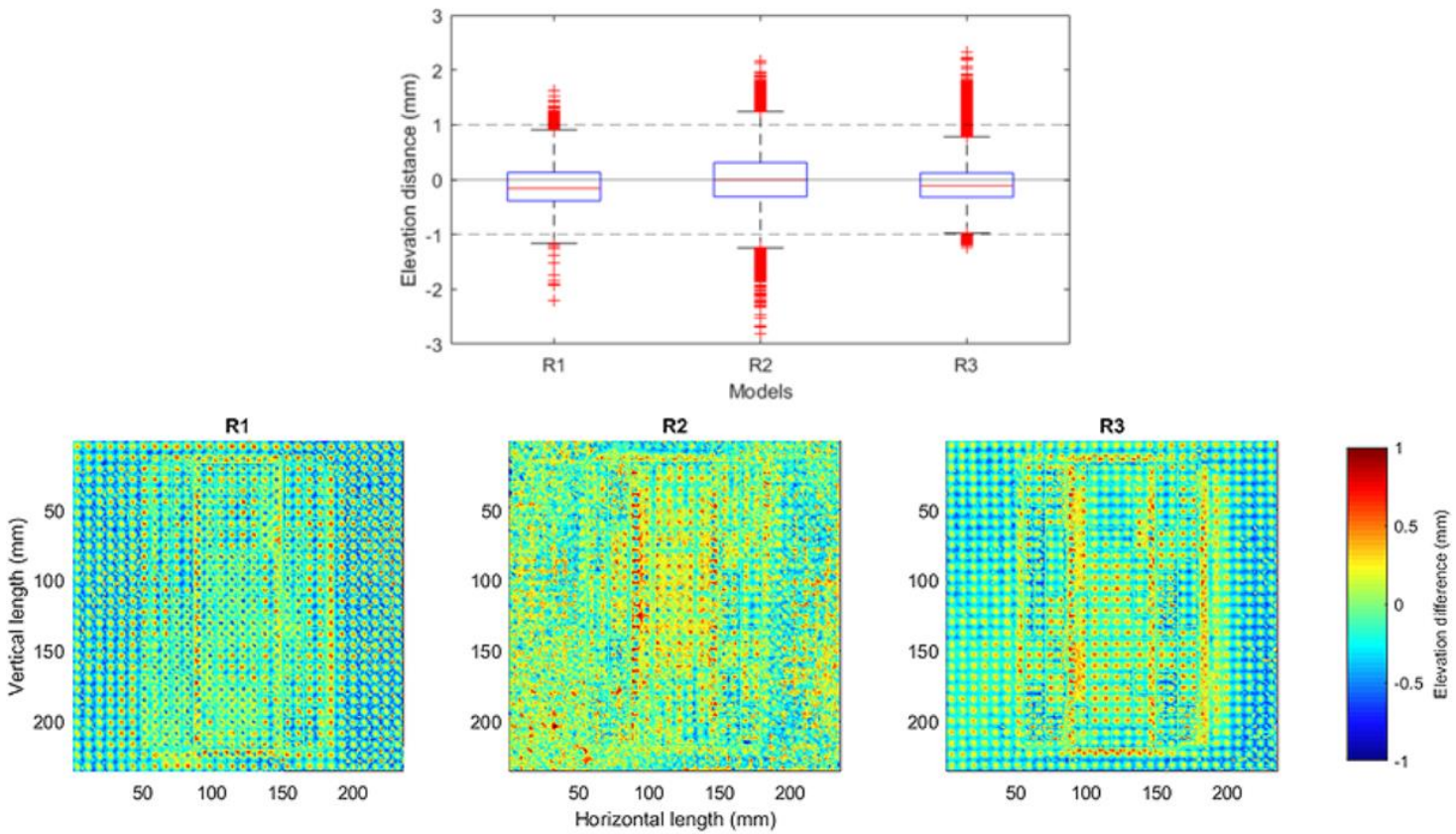

Figure 4.3: (Top) Box plot of the distribution of derived point clouds from R1, R2 and R3. (Bottom) Point clouds showing difference from reference.

4.3. Effect of number of images

The effect of the number of images on point cloud density, and their accuracy, was investigated. Forty images were taken with a LG Nexus 5, and the sequence subsampled to examine point clouds derived from 5, 10, 20, 30 and 40 images.

Table 4.1: Derived point clouds generated from a different number of images. White areas depict where no measurement points are present.

Number of images	Top view	Angle view
5	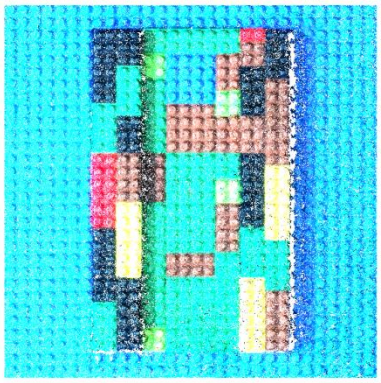	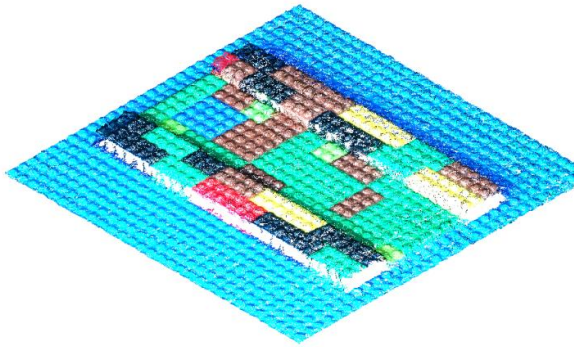
10	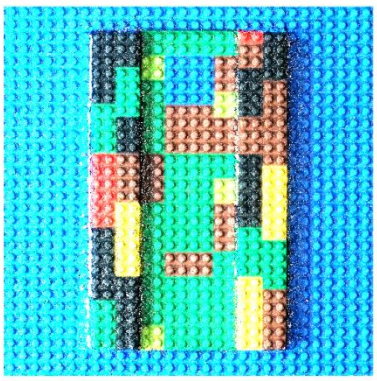	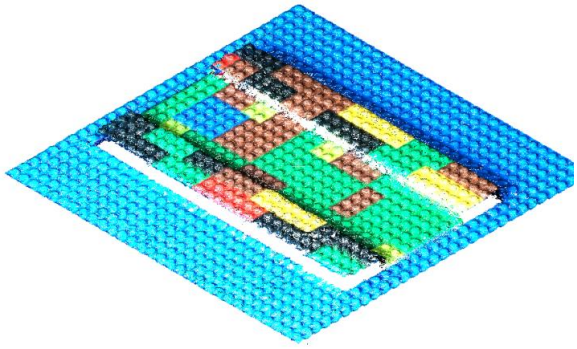

Number of images	Top view	Angle view
20	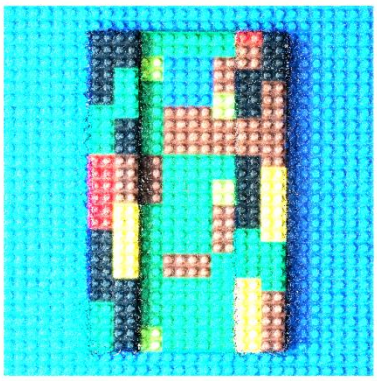	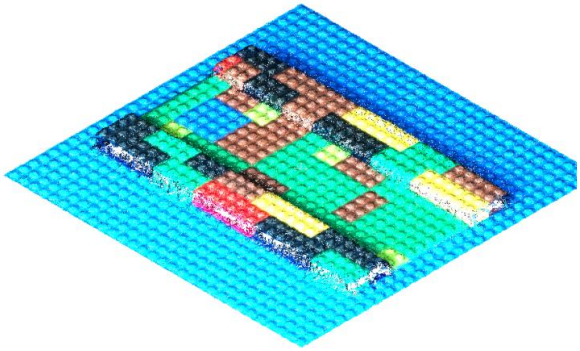
30	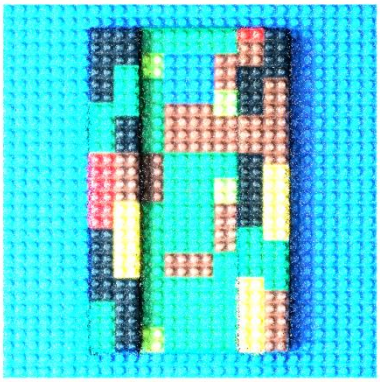	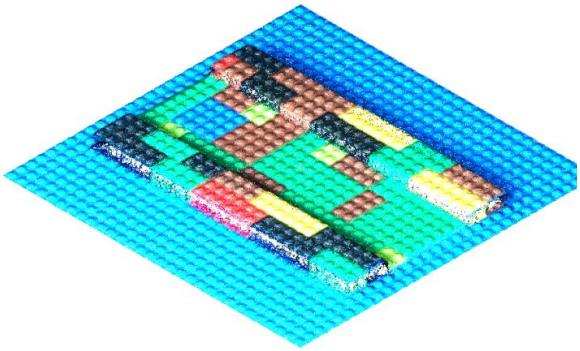
40	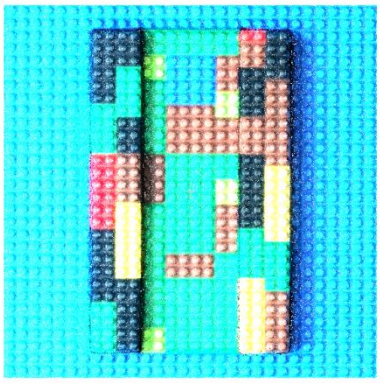	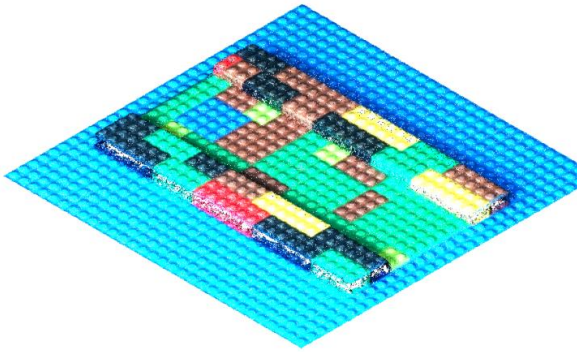

4.3.1. Point cloud density

Table 4.1 and Figure 4.4 shows that the point cloud derived from 5 images had the lowest density (6.7 points per mm^2, $ppmm^2$) while the points acquired from 40 images had 10.5 $ppmm^2$. Though the difference between these two derived point

clouds was relatively large, the density plateaus at 20 images. This is because it took about 20 images to cover one round around the object. This result shows that the ability of a point cloud to represent small-scale features is unlikely to reveal much improvement beyond this threshold number of images. At the scale of LEGO® bricks, the threshold to process satisfying dense point clouds is at 20 images.

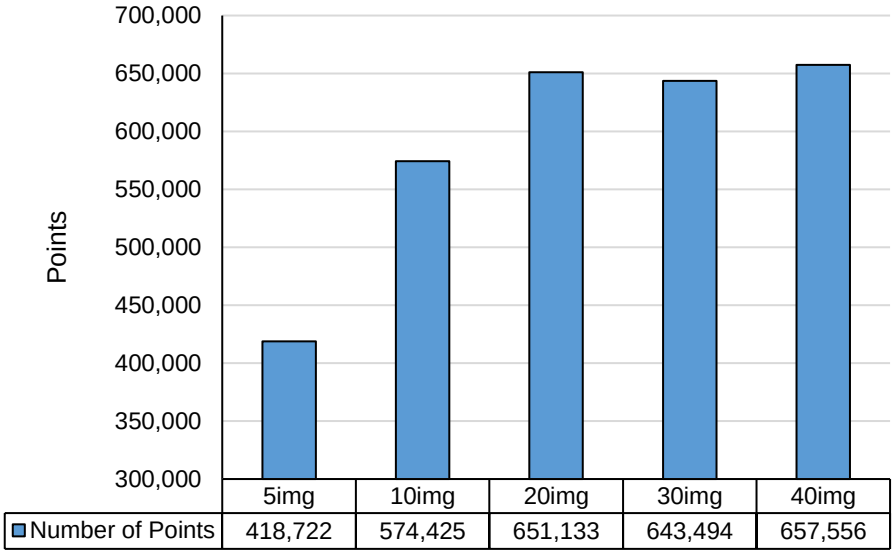

Figure 4.4: Number of point clouds generated from different number of images

4.3.2. Accuracy

In Table 4.1, the point clouds derived from five images show a poor distribution of points throughout the point cloud. Some points are missing along both sides of the bricks of the model since there was insufficient image overlap. Moreover, an extensive amount of outlying points is presented which can be observed by the distortion of bricks. The point generated from 10 images have higher density of points throughout the area of the model. However, the image

coverage was still insufficient to generate points along the vertical elevated points. By processing 20, 30 and 40 images, the derived point clouds had have well-distributed points. This similarity reflects the minimal difference in point cloud density.

These point clouds show that the effect of the number of images on point cloud density has a critical effect on the ability of SfM to resolve surface features (the side of the bricks) where elevation changes, and thus shadowing, are greatest. Thus, this result has significant importance for the accurate measurement of rilled soil surfaces. The poor resolution of the bars occurred for a low number of images because a higher number of images are critical for gaining a sufficient degree of overlap and coverage from different angles between images to match these surface features.

From the statistical bar chart shown in Figure 4.5, it can be seen that more than 99.75% of point clouds fell within ±1 mm of the CAD model. At this range of error, these points have no statistically significant difference. However, at an accuracy level of±0.5 mm, the points derived from 40 images had the highest accuracy. The point clouds processed from 10 images showed furthest deviation which accommodates the accuracy measured at a distance within ±0.5 mm. The deviation reduces gradually when increasing the number of images processed.

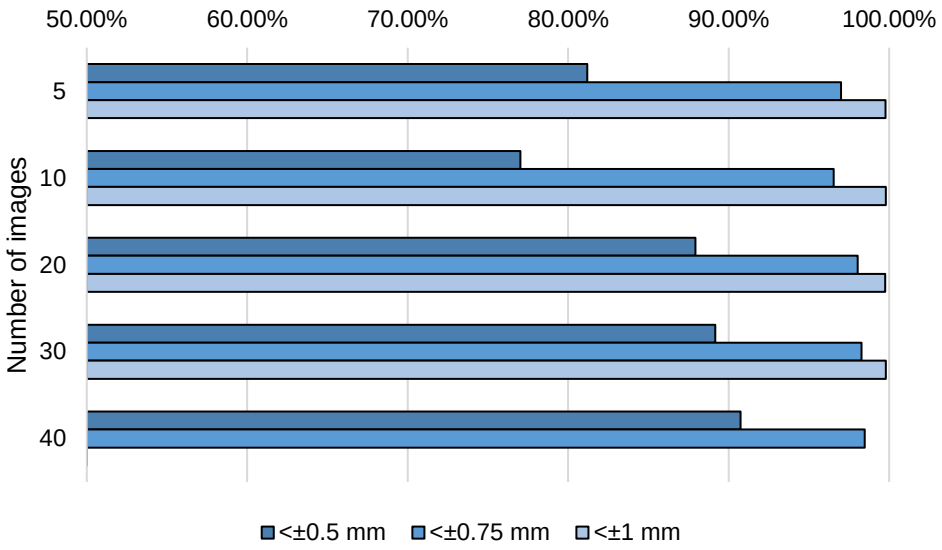

Figure 4.5: The percentage of accuracy of derived point clouds by number of images

4.4. Effect of image size

The importance of testing whether the image size affects accuracy is reflected in the choice of camera one should use to capture the image sequence. Cameras contain sensors that capture light in micro-grid format, and transfer and store the pixel values into its memory as a readable file. Thus, the size of the images reflects the size of the sensor. Therefore, just one camera was used for this test, the Sony ILCE-6000. This camera contains a 24.3 megapixel sensor and; each pixel captures and stores 8 bits per colour channel. The sensor captures three colour channels (i.e. red, blue and green) leading the camera to store 24 bits per pixel. Resizing each image sequence to have images sizes of 500, 2,000, 5,000 and 12,000 kilobytes represents cameras with image sizes of 0.2, 0.6, 1.5 and 4 megapixels respectively.

Figures 4.6 and 4.7 shows that image size has only a small effect on point cloud density and a negligence effect of accuracy.

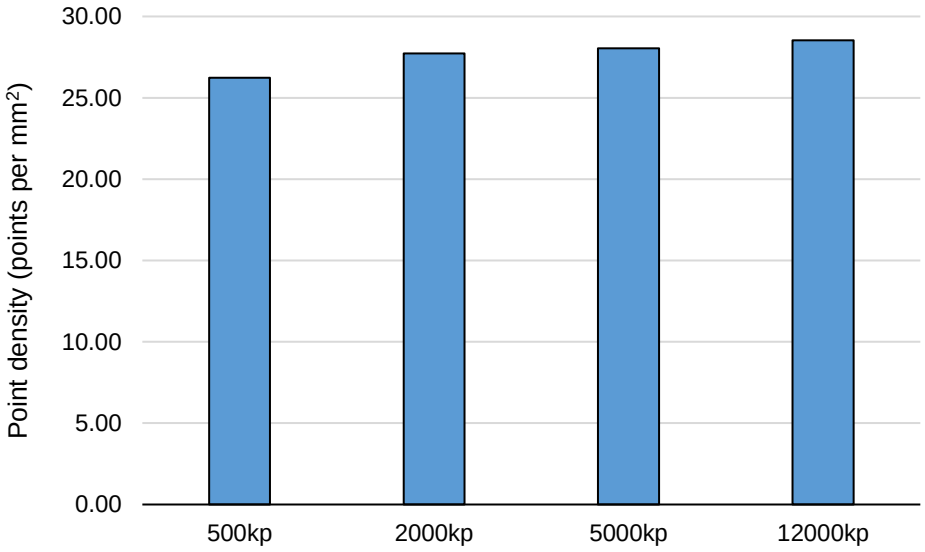

Figure 4.6: Density of points in each set of point clouds. The number of points gradually increases when image sizes are increased.

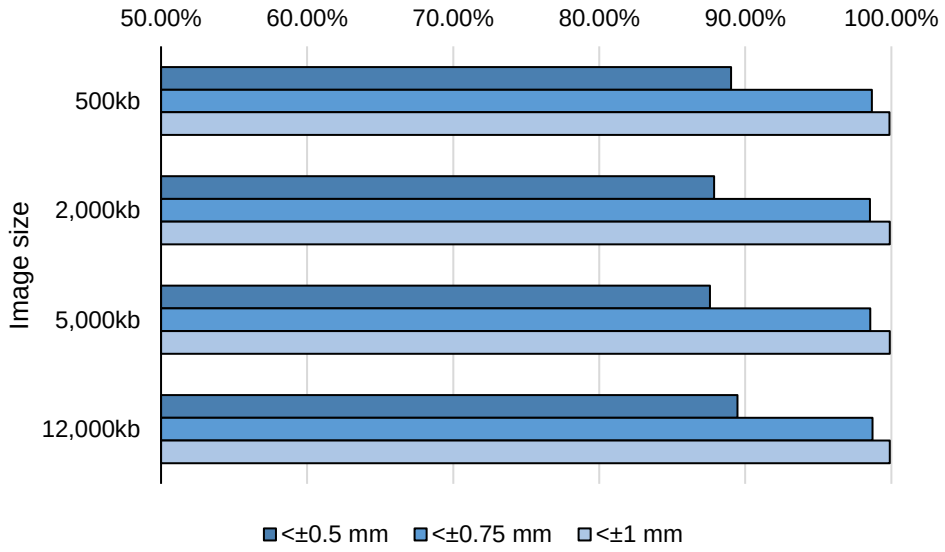

Figure 4.7: Accuracy of points by image size

4.5. Effect of image exposure

Figure 4.8 shows the point clouds and distributions of Red, Blue and Green pixels derived from the raw images, and from those in which the exposure of the images was increased and decreased. The latter represents bright conditions (e.g. bright, direct sunshine) and the latter dark conditions (e.g. overcast conditions). The images in Figure 4.8 show that lower exposure images contained extensive shadows and darker pixels, and some parts of the shadowed areas turned completely black. On the other hand, in the high exposure images the shadowed areas appeared clearer when compared to the raw and lower exposure images. Unlike the histogram presented in Figure 4.2 the histogram presented in Figure 4.9 were three times exaggerated in order to illustrate the distribution of the RGB pixels better. The histograms show that the red and blue pixels in the raw images were under and over exposed respectively; while the green pixels remain distributed within the range the camera sensor can hold. The histogram of the dark images were mainly exposed to the left, which means most pixels were underexposed especially the red and blue pixels. The bright images presented a histogram that mainly shifts to the right. They were mostly overexposed especially the blue pixels.

The elevation difference between point clouds and the CAD model is illustrated in Figure 4.9 indicate that the show little variation between those derived from the raw images and those from the higher exposure images. In contrast, the DEM of difference derived from the dark images shows an extensive difference. The shadowed areas produced by the brick knobs obscure the populated point clouds and generated noisy points throughout the surface area. Moreover, elevation

differences are sever on the area along the brick bars where shadows are harshly casted – the SfM process might assume the harsh shadowed areas are objects thus adds spurious elevations to these area.

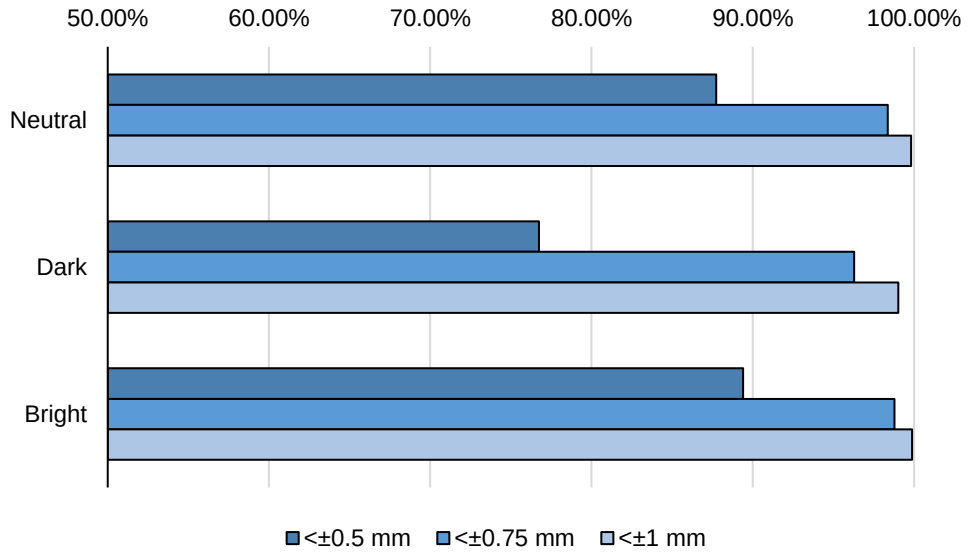

Figure 4.8: The accuracy of point clodus by exposure

Figure 4.8 shows that the point clouds derived from higher exposure images produced a slighter more accurate measurement of the LEGO model than the raw images. The lower exposure images produced point clouds with similar performance at accuracy levels of ±0.75 mm and ±1 mm, but much lower performance at the ±0.5 mm level.

These results implied that the more detail presented in the images, the greater the potential to produce more accurate SfM-derived point clouds. The images with higher exposure contain the most detail in the scene, and reduce the shadowing effects by revealing details that would otherwise be hidden, allowing the SfM

processing software to detect better matching points in the images. Overall, this result reveals that shadowing has a strong control on point cloud accuracy through generating spurious elevations and substantial dark pixels which could be undetectable by the processing software.

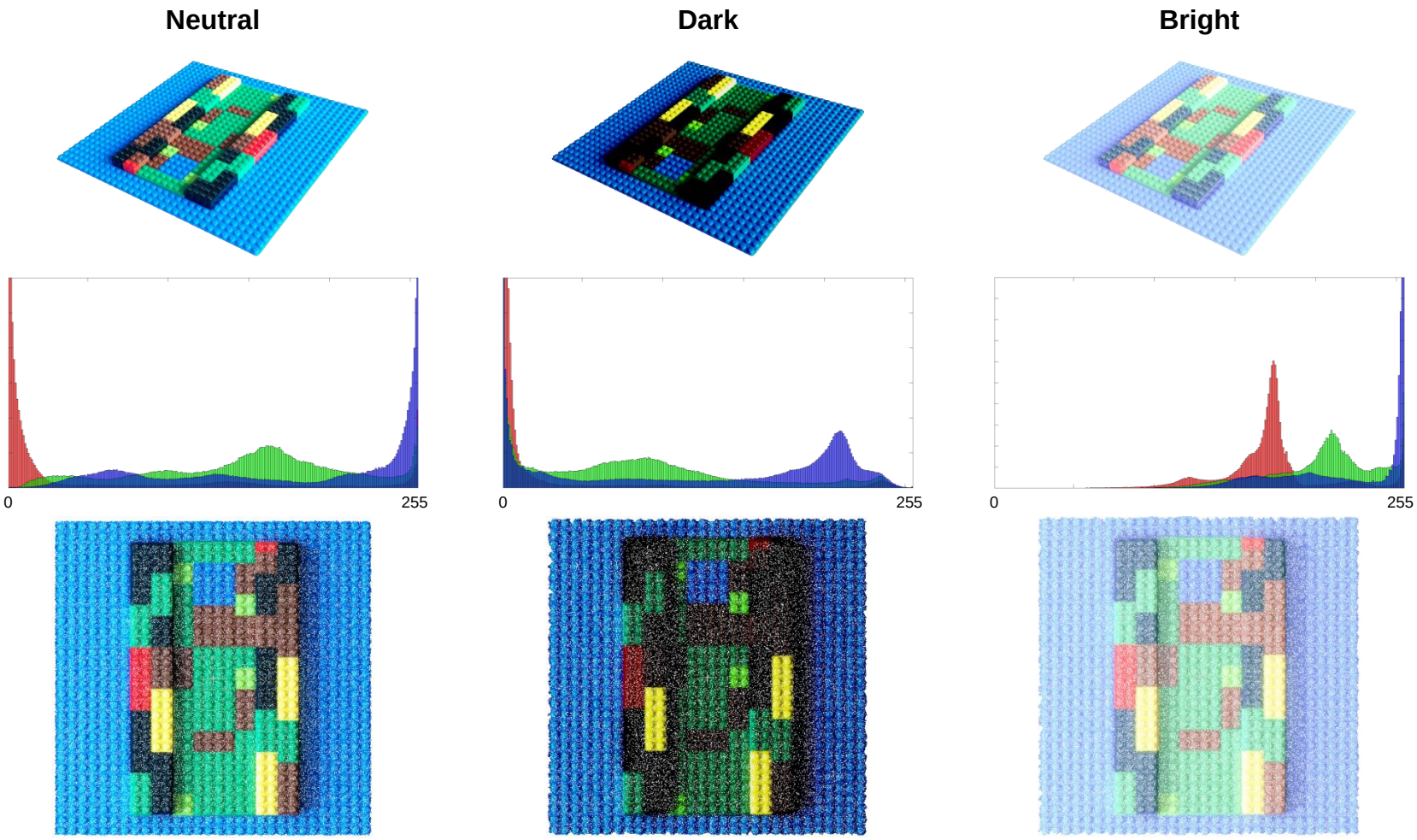

Figure 4.9: (Top row) Tested images. (Middle row) Histogram of Red, Blue and Green pixels. (Bottom row) Derived point clouds.

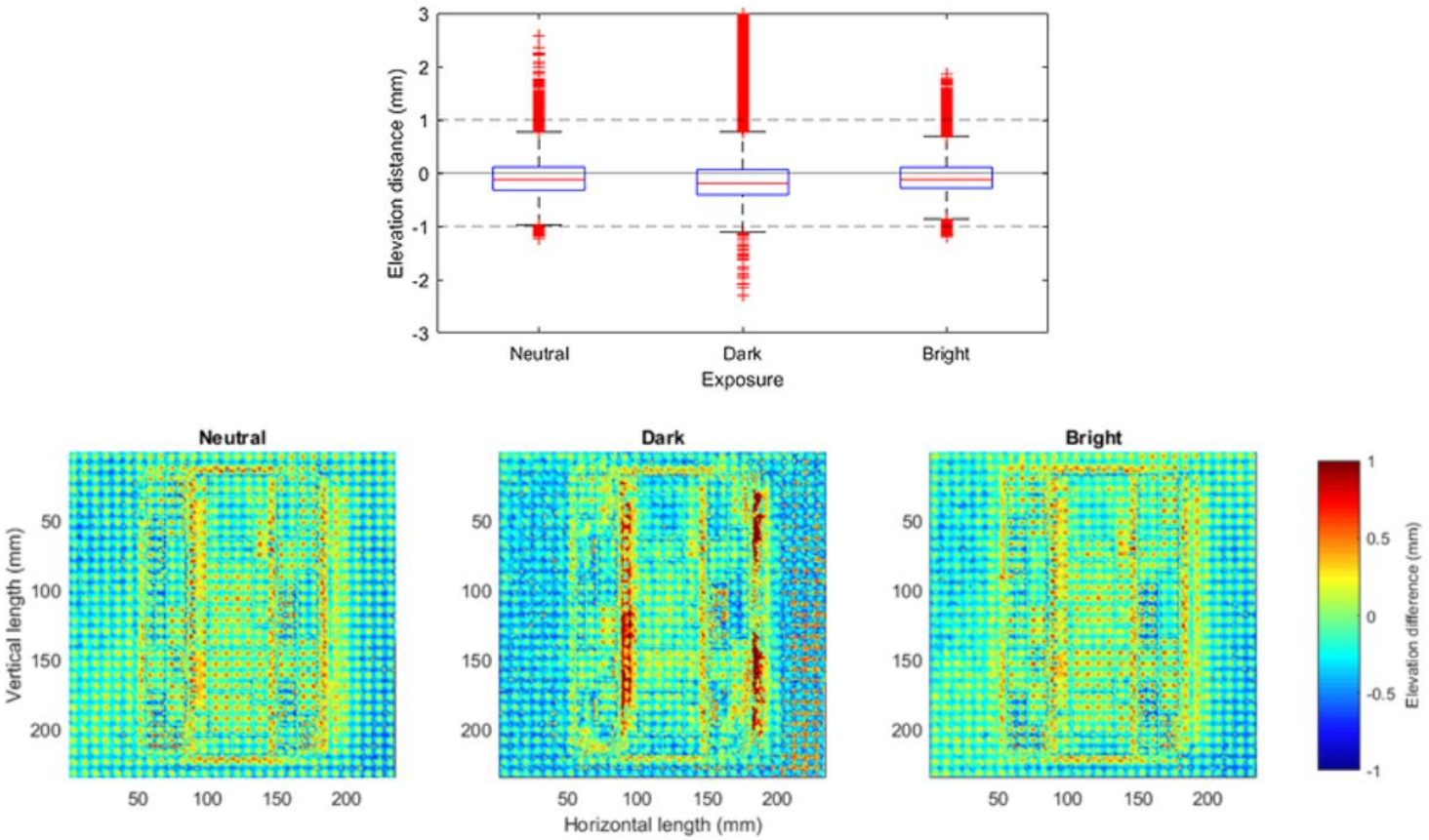

Figure 4.10: (Top) Box plot of the distribution of derived point clouds from Neutral, Dark and Bright (Bottom) Point clouds showing difference from reference.

4.6. Summary

From each factor tested, it can be concluded that:

1. Different cameras used to acquire image sequences do not substantially affect the accuracy of the results. However, in order to acquire the most accurate result, pixel noise should be minimized. Therefore, adjusting the camera to have lower light sensitivity (ISO value) would reduce the amount of noise in the images. This experiment gave the confidence that in sequential tests, portable cameras such as mobile phone cameras could produce adequately high-resolution DEMs. In this circumstance, expensive and lesser portable cameras do not produce higher quality of DEMs that are more accurate.

2. The number of images in the sequence does not have any significance as long as adequate coverage of the scene is captured. Low coverage of the scene leads to low populated point clouds. This test was crucial to understand since the bricks built represented rill eroded surface. The missing points along the depth of the higher-level bricks could introduce error in sequential experiments. Therefore, a substantial number of images should be considered when the density and population of points is essential.

3. Image size has negligible influence on accuracy.

4. Brightness and contrast of the image, amongst all factors tested, had the most influence on point accuracy. The detection algorithm in SfM-processing software (Photoscan 1 in this case (Agisoft LLC, 2016)) might assume black pixels as physical surface, hence produces point clouds at the position where black pixels are presented.

In order to reduce the error caused by underexposed pixels, adjust the underexposed pixels to brighter tone.

These results reveal, for the first time, that SfM is capable of producing highly accurate measurements of micro-topographic features at a scale similar to those found on rilled soil surfaces. They provide crucial information on how to optimize the acquisition of SFM-imagery in different lightning situations and using different cameras.

CHAPTER 5

Effect of slope on the statistical properties of eroded soil surfaces

5.1. Introduction

Before investigating the hydraulics, and their link to micro-topography, it is essential to establish the roughness characteristics of the eroded surfaces. Surfaces which are discussed in the following sections are surfaces that were prepared for the simulated storm events and the surfaces that were created after the experimental rainfall. The surfaces before the simulated storms were thoroughly mixed to distribute the different particle sizes and screeded flat to ensure the surface was randomly organized.

The aim of this chapter is to examine the statistical properties of soil surface following a single, high-intensity rainfall event. The chapter will utilise the DEMs derived from the SfM technique to provide detailed information on the micro-topography of these surfaces. Specifically, this chapter will answer the following research questions:

1. What are the statistical properties of eroded surfaces at the micro-topographic scale?

2. What is the effect of slope on these properties and the roughness of the soil surface?

Answering these questions will provide the information for examining the correlation between micro-topography and overland flow hydraulics in Chapter 7.

5.2. Digital elevation models

Digital elevation models (DEMs) of the experimental surfaces were produced to statistically analyse the roughness characteristics. There are two sets of DEMs – one of the screeded surface before the simulated storm, and one of the rill eroded surface after twenty-minute of rainfall with an intensity of 110 mm hr^{-1}. These eroded surfaces come from experiments using slopes of 5, 8, 12, 15 and 20 percent. All the DEMs produced had their mean values set to zero and were detrended to remove non-parallelism between the DEM and the experimental plot.

In Figure 5.1, as the soil was mixed randomly, the surfaces show no particular organisation. The screeded surfaces were visually flat, and different sediment size were distributed throughout the surface. The DEMs of the eroded surfaces are shown in Figure 5.2. They reveal physical changes from the screeded surfaces. At low slopes, the surface appears to be more flat and smoother, and rills were not obviously presented. However, the severity of rills were presented when steeper slopes were introduced. The width of the rills ranged approximately from 50 to 200 mm and had average depths between approximately 10 to 30 mm.

Figure 5.1: Example of the digital elevation model acquired from S3b. Streamwise direction is 1,100 mm while the lateral direction is 800 mm.

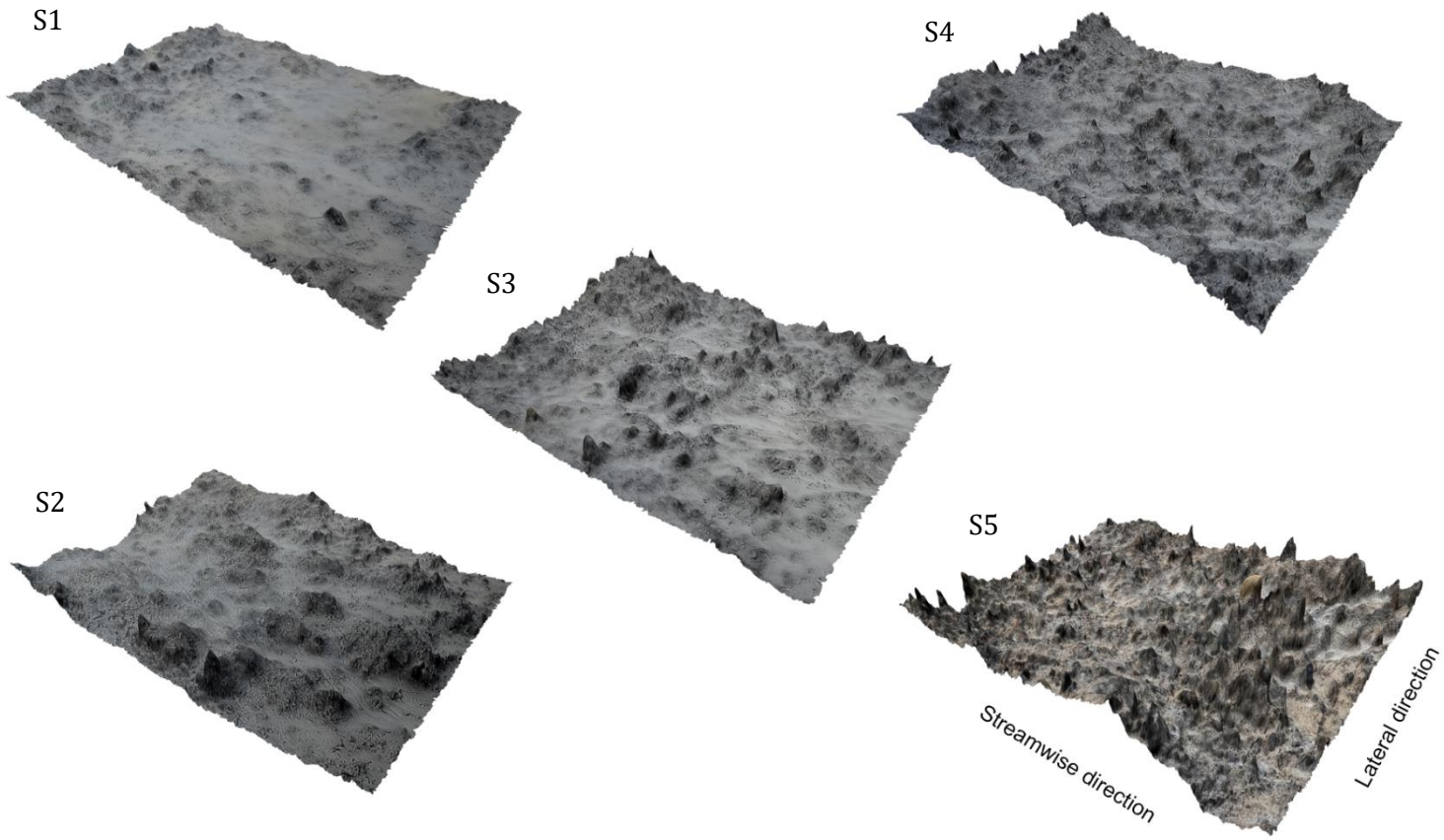

Figure 5.2: Digital elevation model showing the physical characteristics of the five surfaces. The elevation height (z axis) of the surfaces were five times exaggerated.

5.3. Probability distribution function

The probability density functions (pdf) of the surfaces in Figure 5.3 reveal a clear difference between screeded and eroded surfaces. The screeded surfaces, as mentioned above, reveal a normal distribution of elevations (Goodness-of-Fit test using Kolmogorov-Smirnov test), indicating a random organisation. The similarity in the pdfs reveal a consistency in the bed preparation between the different tests. However, after the storm events were applied, the elevation distributions changed dramatically. The eroded surfaces showed a structural pattern of change that relates to the slope of the plot. The skewness shows a gradual decrease with an increase in slope. For example surface S1 which had had the highest skewness value of 0.47 while the skewness was last half (0.22) for surface S5. A summary of the statistical analysis is presented in Table 5.1.

Table 5.1: The summary of properties of the eroded surfaces, where *Sk* is the skewness *Kr* is the kurtosis and *k* is the range of the elevation distribution, and RR_z is the random roughness value, quantified by the standard deviation in elevations. The correlation lengths scales of the elevation in the streamwise direction are represented by l_{x0} and by l_{y0} for the lateral directions H_x and H_y are the Hurst exponents for the streamwise and lateral variation in elevation respectively.

Property	S1	S2	S3	S4	S5
Sk	0.47	0.45	0.32	0.38	0.22
Kr	3.60	3.60	2.96	4.34	3.25
RR_z *(mm)*	2.41	2.87	3.34	3.89	6.14
k (mm)	17.53	22.54	27.65	33.60	47.61

Property	S1	S2	S3	S4	S5
l_{x0} *(mm)*	59.42	89.59	62.48	92.81	71.97
l_{y0} *(mm)*	41.46	47.83	44.91	46.78	42.84
H_x	0.83	0.74	0.81	0.74	0.74
H_y	0.81	0.89	0.87	0.87	0.85

Generally, positive skewness of the pdfs reflects the armouring effect on the surface (Aberle and Nikora, 2006; Cooper and Tait, 2009; Mao *et al.*, 2011; Mohajeri *et al.*, 2015) where finer particles fill the interstices between larger particles. For gravel surfaces, Cooper and Tait (2009) suggested that armouring would statistically reduce the magnitude of the surface elevation below the mean surface level. This effect is illustrated clearly in Table 5.1 and Figure 5.3 on surface S5. Surface S5 shows to have the highest roughness reflected from the wider distribution of elevation and skewness that is more positive.

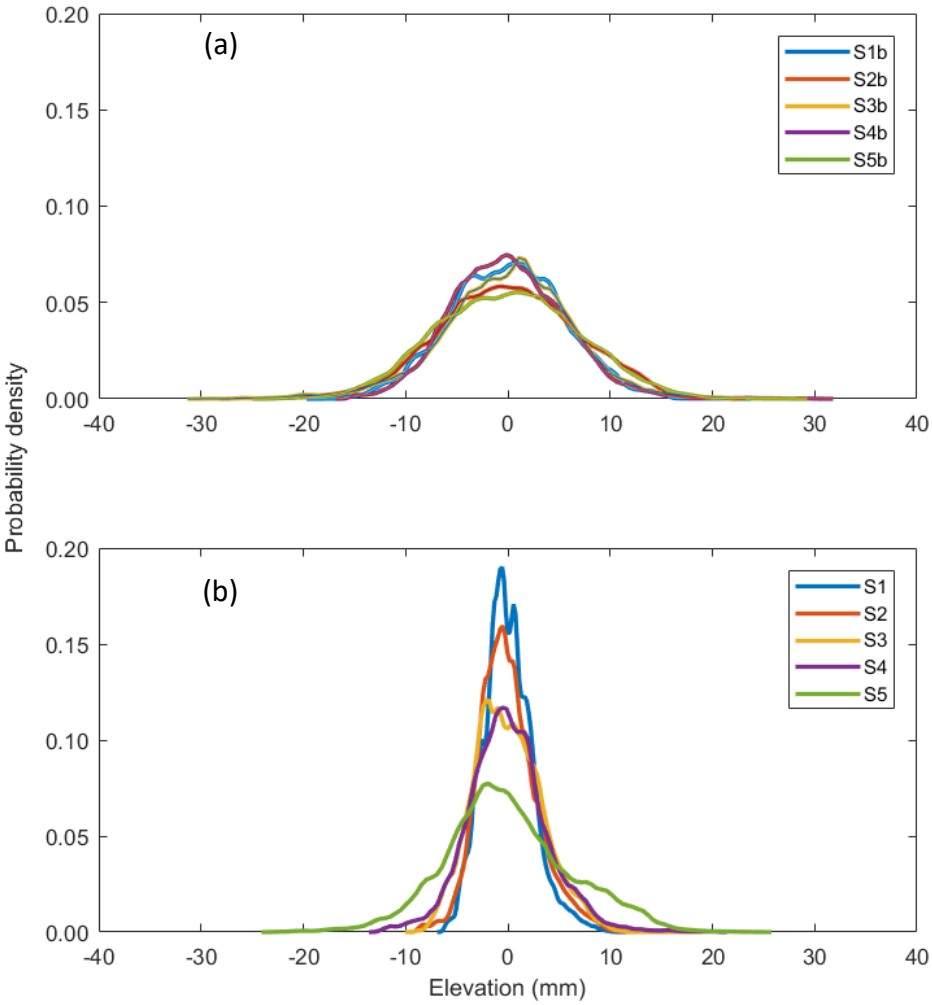

Figure 5.3: The probability density function of the zero-mean surface elevation of (a) screeded surfaces and (b) eroded surfaces.

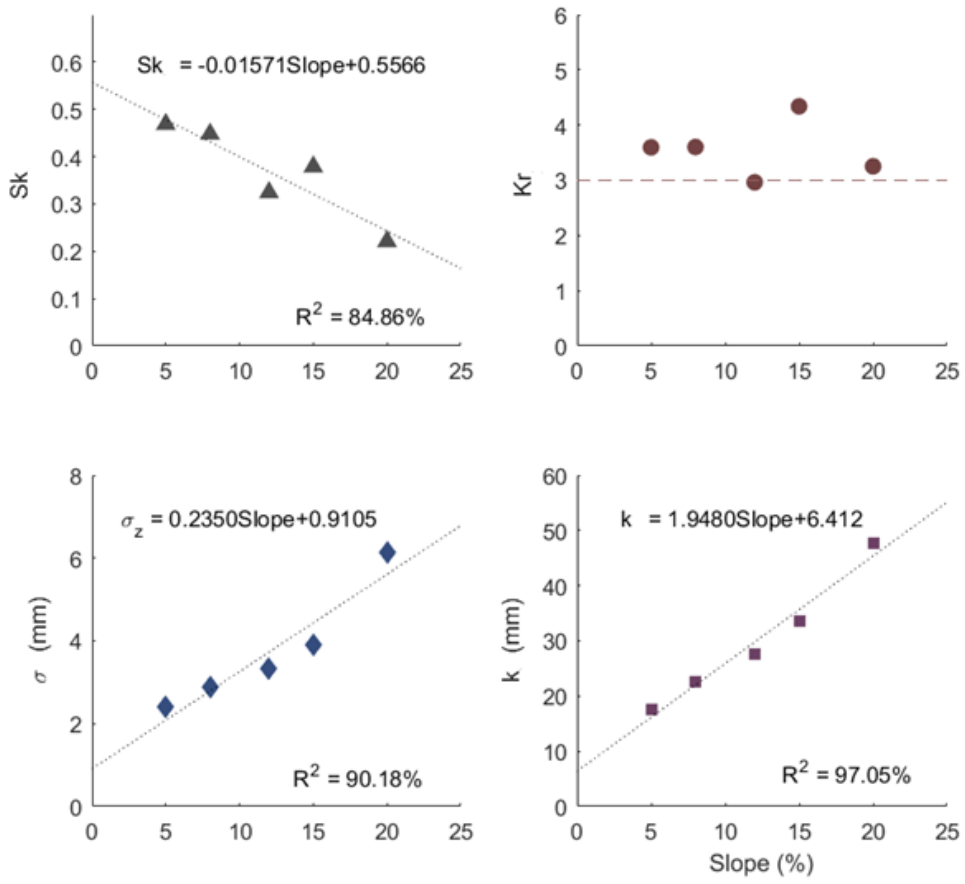

Figure 5.4: The relationship between surface properties and slope

The kurtosis values reported in Table 5.1 and Figure 5.4 suggest that the elevation distribution of the surfaces have approximately normal distribution. These values shown no clear relationship with plot slope. The standard deviation in elevations (random roughness, RR), and the range however show a clear positive relationship with slope (Figure 5.4d). Given these two parameters are commonly used to quantify the roughness of sediment surfaces (e.g. Nikora *et al.*, Goring and Biggs, 1998; Aberle and Nikora, 2006; Mao *et al.,* 2011) this relationship reveals there is a consistent increase in roughness with slope, reflecting the increased rilling on the surface

5.4. Second-order structure function

The second-order structure function of the surface elevations was used to determine the degree of surface organisation (Nikora *et al.*, 1998; Cooper and Tait, 2009; Mohajeri *et al.*, 2015). The structure function $D(l_x, l_y)$ of bed elevation $z(x, y)$ can be defined as:

$$D(l_x l_y) = \frac{1}{(N-n)(M-m)} \sum_{i=1}^{N-n} \sum_{j=2}^{M-m} \{z(x_i + n\delta x, y_j + m\delta y) - z(x_i, y_j)\}^2 \quad (5\text{-}1)$$

Where $l_x = n\delta x$, and $l_y = m\delta y$ are spatial lags in the streamwise and lateral directions, respectively; n and m are multiplying coefficients; δx and δy are sampling intervals; and N and M are the total number of the surface point clouds in x and y (streamwise and lateral directions). In this study, δx and δy are equal to 1 mm. As described by Nikora *et al*. (1998) and Cooper and Tait (2009), second-order structure functions have a relationship with the correlation function $R(l_x, l_y)$ as described in equation (5-2):

$$D(l_x l_y) = 2\left[\sigma_z^2 - R(l_x, l_y)\right] \quad (5\text{-}2)$$

The similarity of the l_{y0} values are also reflected in H_y values which can be expressed by the equations:

$$D(l_x, l_y = 0)/2\sigma_z^2 \propto 1^{2H_x} \quad (5\text{-}3)$$

and

$$D(l_x = 0, l_y)/2\sigma_z^2 \propto 1^{2H_y} \quad (5\text{-}4)$$

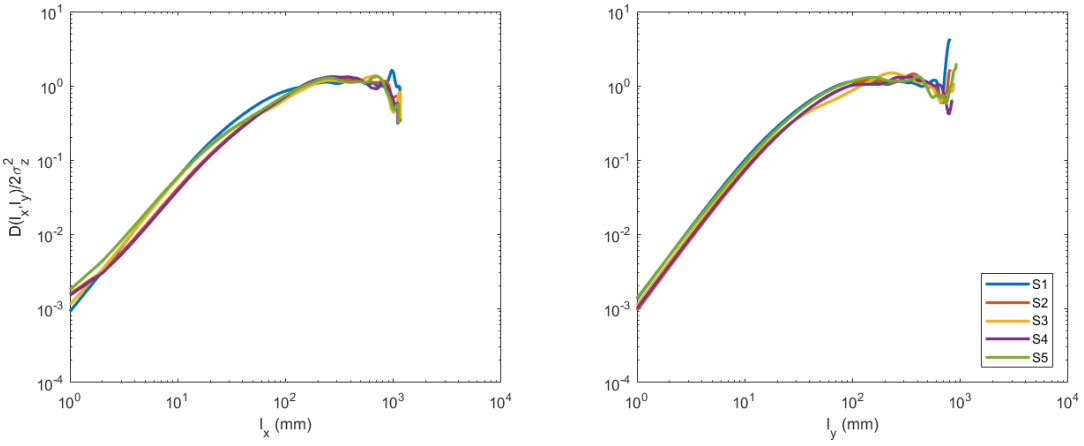

Figure 5.5: Second-order structure functions of the surface elevation normalised by $\boldsymbol{2\sigma_z^2}$. The value of D increases when lags in streamwise and lateral direction increase. This implies that the further the elevations are measured apart, the less correlated they are.

This relationship can be identified by calculating the correlation function *R(l_x, l_y)* for different lag distances. At large lags, when *R(l_x, l_y)* gets close to 0 and *D* close to $2\sigma_z^2$, there is low spatial correlation.

The plot shown in Figure 5.5 shows several important results. Firstly, both Figure 5.5a and Figure 5.5b reports the $D(l_x, l_y)/2\sigma_z^2$ of each surface to be at low values at small lag distances which indicate that the correlation levels are high. Secondly, at higher lag distances, the value of $D(l_x, l_y)/2\sigma_z^2$ increases indicating a lower correlation level. Thirdly, all five surfaces have similar structural organisation

where elevations measured further than 100 mm are close to or above unity and have no negligible correlation. At this lag distance, the surfaces' organisation is considered random (Nikora *et al.*, 1998).

When considering the value of l_{x0}, or the lag in streamwise directions at zero (shown in Table 5.1), of each surface, it can be seen that the values do not form any systematic pattern despite the increase in slope. The results also suggested that eroded surfaces have longer roughness scales in the streamwise than in the lateral direction due to rilling of the surface. However these length scales showed no clear relationship with slope suggesting that for eroded soil surfaces containing both grain and form roughness (primarily rills), these roughness measures provide a poor representation of surface structure.

The Hurst exponents or H_x and H_y in streamwise and lateral direction respectively, refers to the scaling exponent estimated from the scaling region of equations (5-3) and (5-4). The Hurst exponent determines the complexity of the topography, in which larger values indicate a less complex topography (Bergeron, 1996; Cooper and Tait, 2009).

The values acquired from each surface are presented in Table 5.1. Similar to the values of l_{x0} the H_x values do not present any particular pattern despite the raise in slope.

5.5. Local roughness

In many studies, random roughness (RR) of the surface, which is represented by a single index, is used to determine runoff which in turns determines erosion (e.g. Bryan, 2000; Römkens *et al.*, 2002). However, RR as a single index does not represent the spatial and local components of the surface (Huang and Bradford, 1990; Vidal *et al.*, 2010; Chu *et al.*, 2012). Therefore, to learn about the impact roughness has on the spatial organisation of the flow, local roughness was calculated. Values of surface roughness are used in the next chapter to examine whether the roughness that changes locally would affect the routing of the stream or not.

Local roughness (LR) was defined by taking the elevation information acquired from cells with an area of 10 x 10 mm and calculating the standard deviation from the mean of the whole surface area for each cell which in this case is equal to zero:

$$\sigma = \sqrt{\frac{\sum_{i,j=1}^{10}\left(z_{i,j} - \bar{Z}\right)^2}{10 - 1}} \qquad (5\text{-}5)$$

The distribution of local roughness presented in Figure 5.6 shows that the distributions are positively skewed. Clear transformation can be observed when higher slopes were applied. At 5 percent slope, the complexity of the rills were relatively lower than the steepest stope examined (Figure 5.6). At 20 percent slope, the surface becomes random. The mean elevation of S5 is relatively high which also confirms the severity/complexity of the rills.

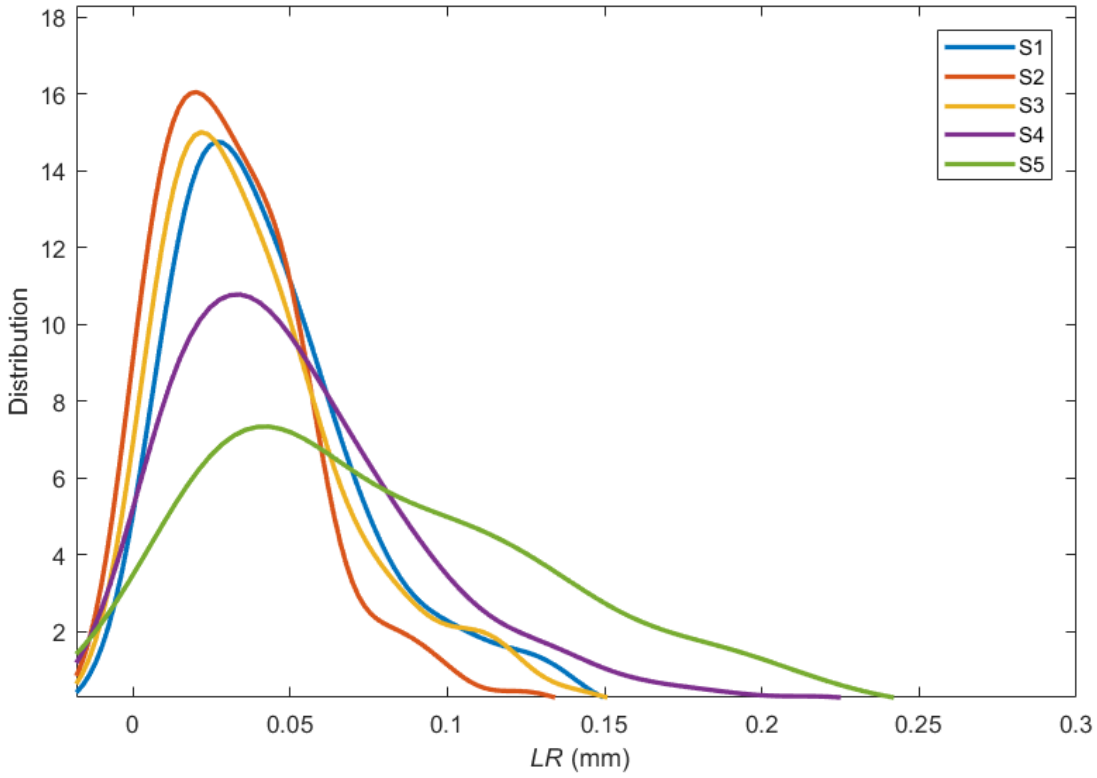

Figure 5.6: Distribution of local roughness

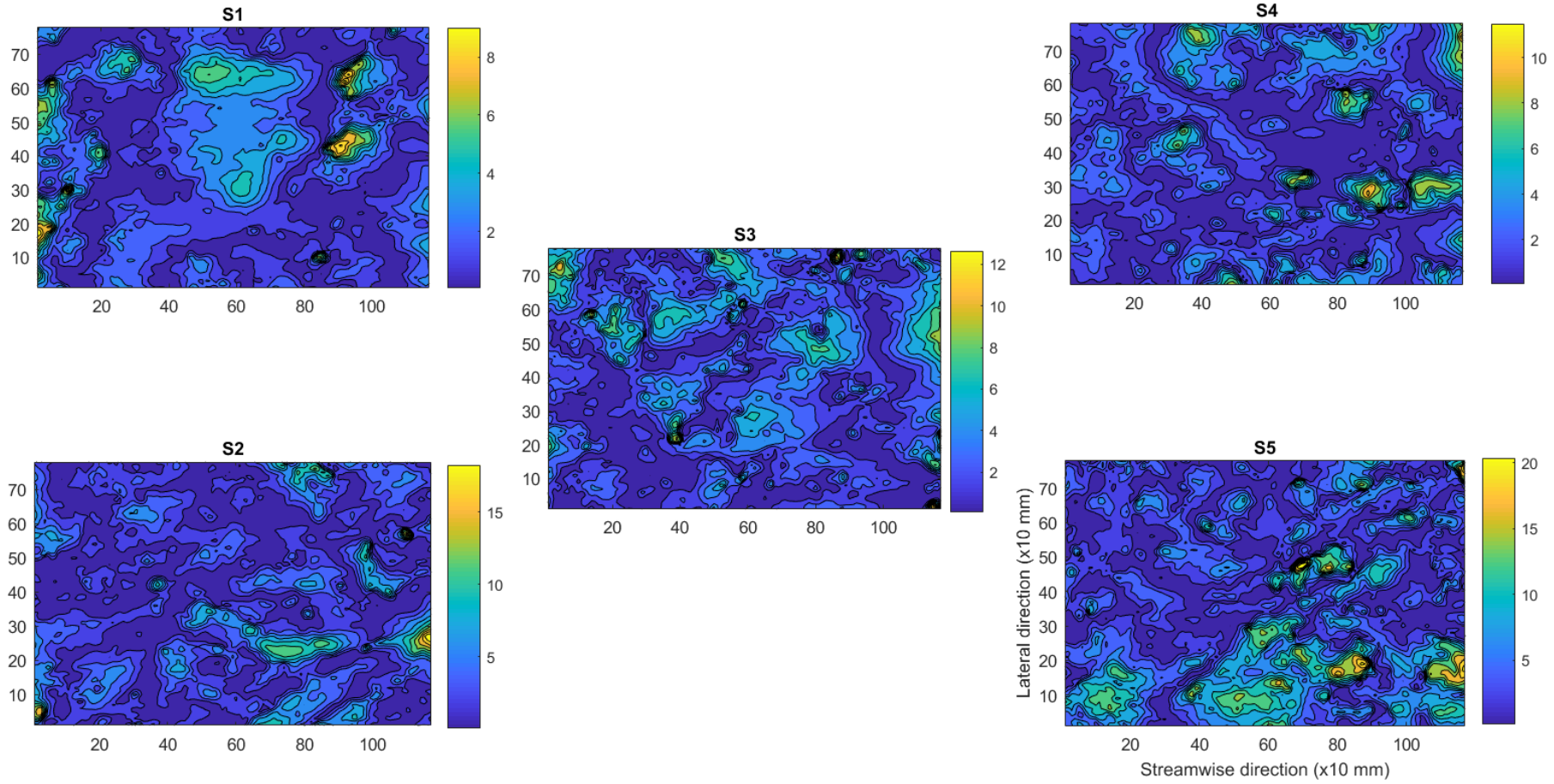

Figure 5.7: Local roughness of each surface.

5.6. Summary

The surface DEMs were statistically test to identify their properties. Key findings from this chapter are:

1. The erosions on the experiment surfaces are highly relevant to the steepness of the slopes. At mild slopes (ex. 5% and 8%), the severity of the erosion was relatively low when compared to steeper ones (ex. 12%, 15% and 20%) which can be statistically determined by the increasing pattern of random roughness (*RR*), *Range* and the decrease of *Skewness* of the distribution (Darboux *et al.*, 2001; Adelsberger and Smith, 2009; Mao, Cooper and Frostick, 2011; Chu, Yang and Chi, 2012).

2. Test of second-order structure function shows that the rills downstream hold more potential in routing the water body which can be observed from the lag distance. At lateral direction the narrowness of rill walls caused the lag at this direction to be relatively low which also affect the ability to route across the rills. Once the distance at both streamwise and lateral direction reaches approximately 100 mm, the correlation of surface elevation is negligible.

3. Though *RR* has been use to classify the erodibility of soil surfaces (Hansen *et al.*, 1999; Bryan, 2000; Römkens *et al.*, 2002), it is important for this study to define the surface roughness of positions around the surface, *LR*. Therefore, roughness values of 10 mm^2 neighbouring elevation throughout the surface were derived from the mean of the whole surface elevation which were set to zero. Results from the distribution (Figure 5.6) of *LR* suggest eroded surfaces tend to increase their complexity when steeper slopes were applied; and at steeper slopes, one could

expect the surface to be random. Moreover, this allows the analysis to learn precisely the location and the change of surface roughness.

CHAPTER 6

The effect of discharge on the spatial distribution of velocity over eroded soil surfaces

6.1. Introduction

The flow characteristics of this study were measured using Particle Tracking Velocimetry (PTV) method. Particle displacements from a 120 minute recording period were computed into a 10 x 10 mm grid of velocities. At each slope, the flow was measured for three discharges. The discharges were 6.4, 4.4 and 2.2 $\times 10^{-4}$ m^3 sec^{-1} and are referred to as high (h), medium (m) and low (l) discharges respectively. The velocity data acquired from the displacement were classified into two velocity directions – streamwise (u) and lateral (v). This chapter aims to answer the research question: What is the effect discharge does to flow velocities?

6.2. Qualitative assessment of flow organisation

Velocity maps for each test is shown in Figure 6.3. These maps show the absolute velocity, derived from:

$$\langle \boldsymbol{S} \rangle = \sqrt{\langle \boldsymbol{U} \rangle^2 + \langle \boldsymbol{V} \rangle^2} \qquad (6\text{-}1)$$

where <*S*> is the speed or the absolute velocity, <*U*> is the streamwise velocity and <*V*> is the lateral velocity. The flow pathways can be seen from the individual particle trajectories presented in the figure.

6.2.1. Inundation surface area

The physical differences between each flow were unique. As seen in Figure 6.3, the most obvious difference between each surface were the features of the surface reflected from the map and the reduction in surface area when lower discharges were applied. In steeper slopes, there tends to be stronger concentration of flow within the rills. Velocities are also higher within the channels, especially at the middle of the channels. As the discharge increases the area of inundation surface increases (Figure 6.1) and the control of the surface on the trajectories and the velocity appears to lessen. It can be seen that the area of flow surface reduces gradually according to discharge. Statistical analysis of each flow direction are presented further in this chapter.

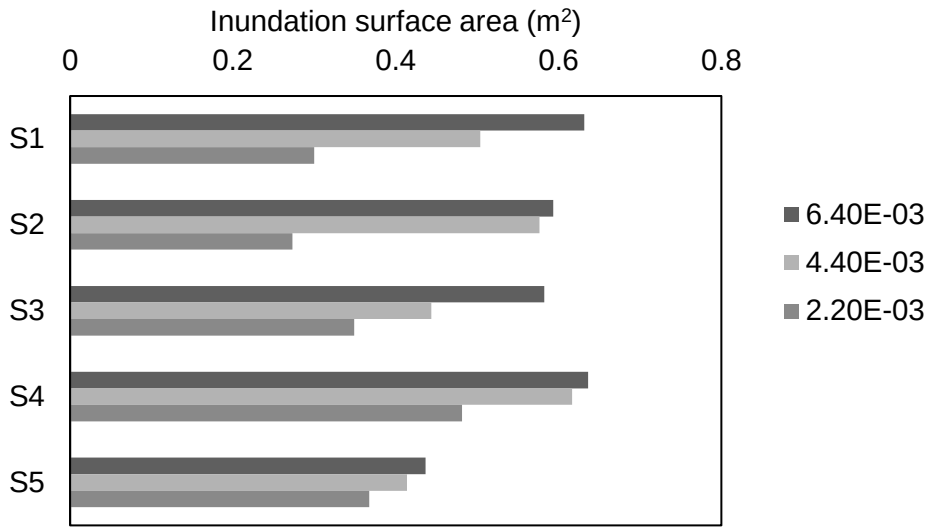

Figure 6.1: The difference in inundation area between each surface and discharge.

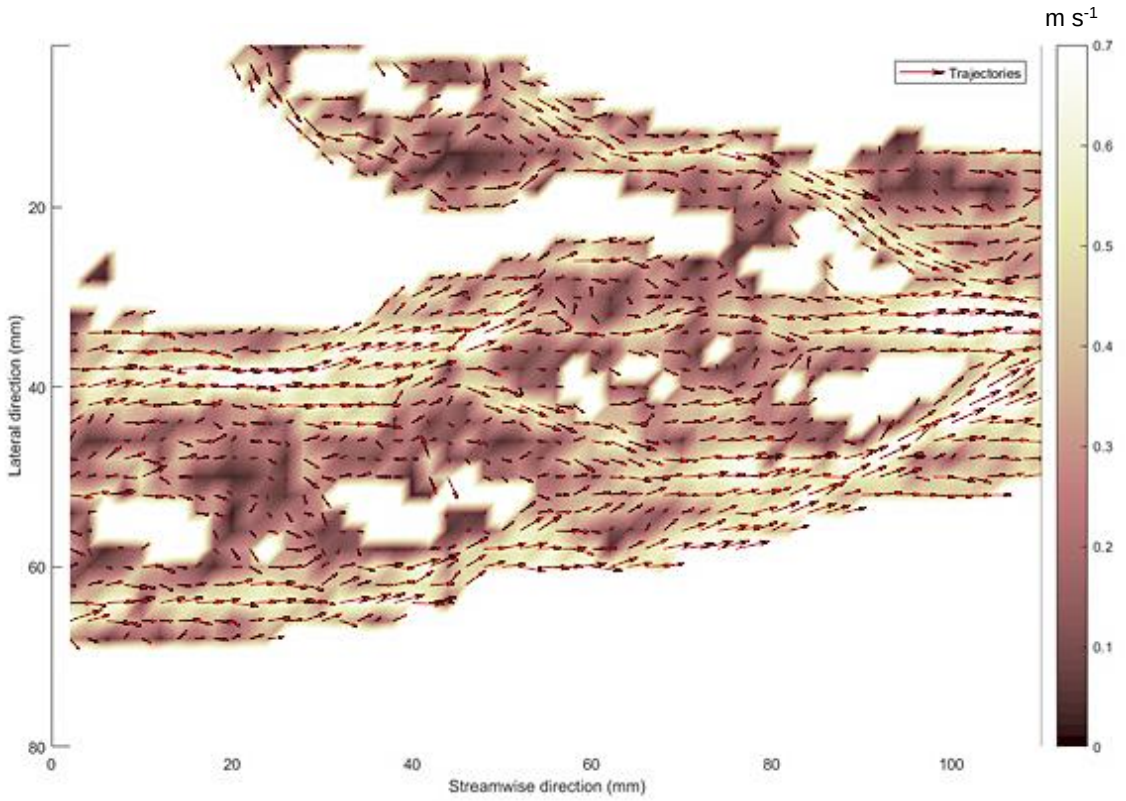

Figure 6.2: Velocity map and quivers showing the flow directions and inundation area of S3m.

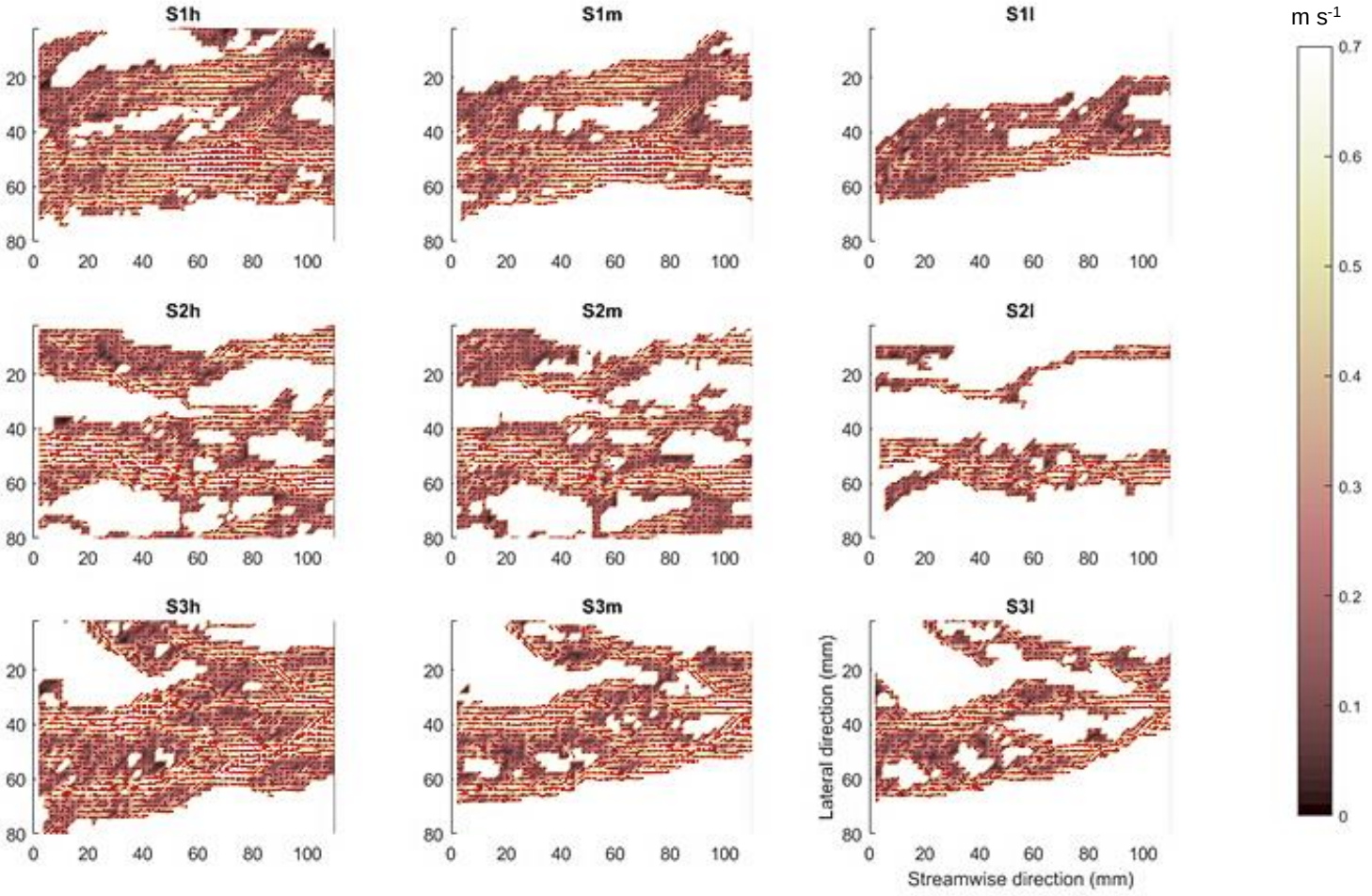

Figure 6.3: Velocity map (m sec^{-1}) of the flows over slopes x-y. The trajectories represent the particle trajectories.

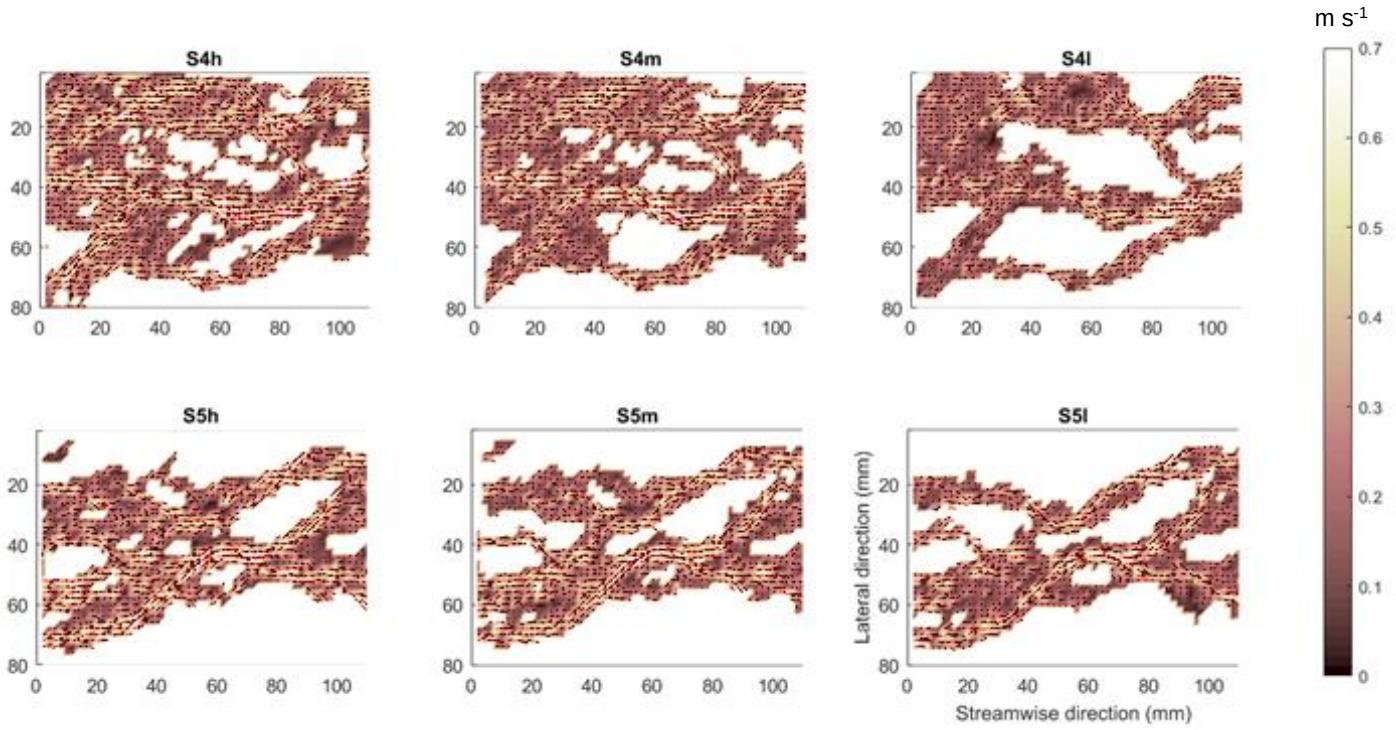

Figure 6.3: Velocity map (m sec-1) of the flows over slopes x-y. The trajectories represent the particle trajectories.

6.3. Spatial distribution of streamwise velocity

The probability distribution functions (pdf) of streamwise velocity for each test are shown in Figure 6.6. The pdfs show that the velocities are positively skewed over all surfaces, and have kurtosis values close to three. These skewness and kurtosis values both decrease with a rise in discharge. Identification of distributions suggest that streamwise velocities fit into Gumbel extreme value distribution (Anderson-Darling factors <20). The spatial variability in velocity is represented by the standard deviation in velocity, given by:

$$\sigma_U = \sqrt{\frac{1}{N}\sum_{i=1}^{N}(u_i - \langle u \rangle)^2} \qquad (6\text{-}2)$$

where N is the number of measured gridded velocities, u is the velocity value measured at grid position i and $\langle u \rangle$ is the spatially-averaged velocity of the entire plot. This measure shows that the spatial variability in velocity increases with discharge. Thus, overall the distributions are wider, flatter and more skewed at higher discharges, reflecting the higher area of inundation, and less concentration of the flow into the rills.

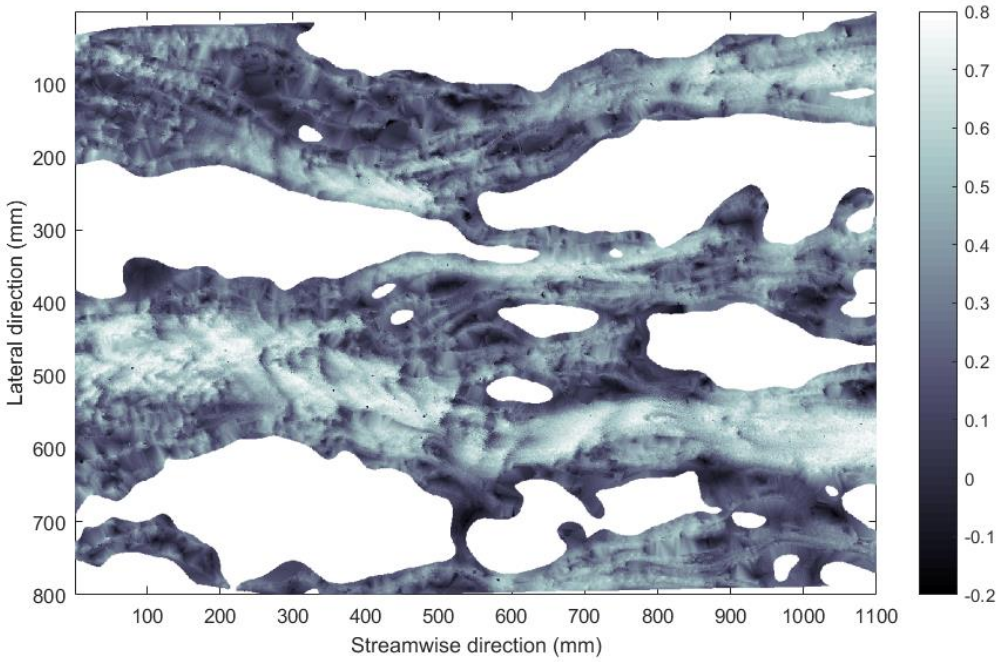

Figure 6.4: Example of the streamwise velocity (m sec^{-1}) flow map from S2m.

In Figure 6.5, each flow, by discharge rate, was related to flow properties. It can be seen that the rise in discharge increases the mean velocity systematically. The flow variability also shows a systematic increase when higher discharge was applied. As inundation area is low, the concentration of flows were mainly within the rills, so the velocities were governed by the threading and routing of the rills. While inundation area gets higher, flows travelled more in interrill areas, and were then more independent from the rills. The decrease of skewness and kurtosis at higher discharge rates infers that the distribution of the flow velocities tend to be more uniformed as higher discharges are applied. This is also due to the independence of flow when inundation area expands.

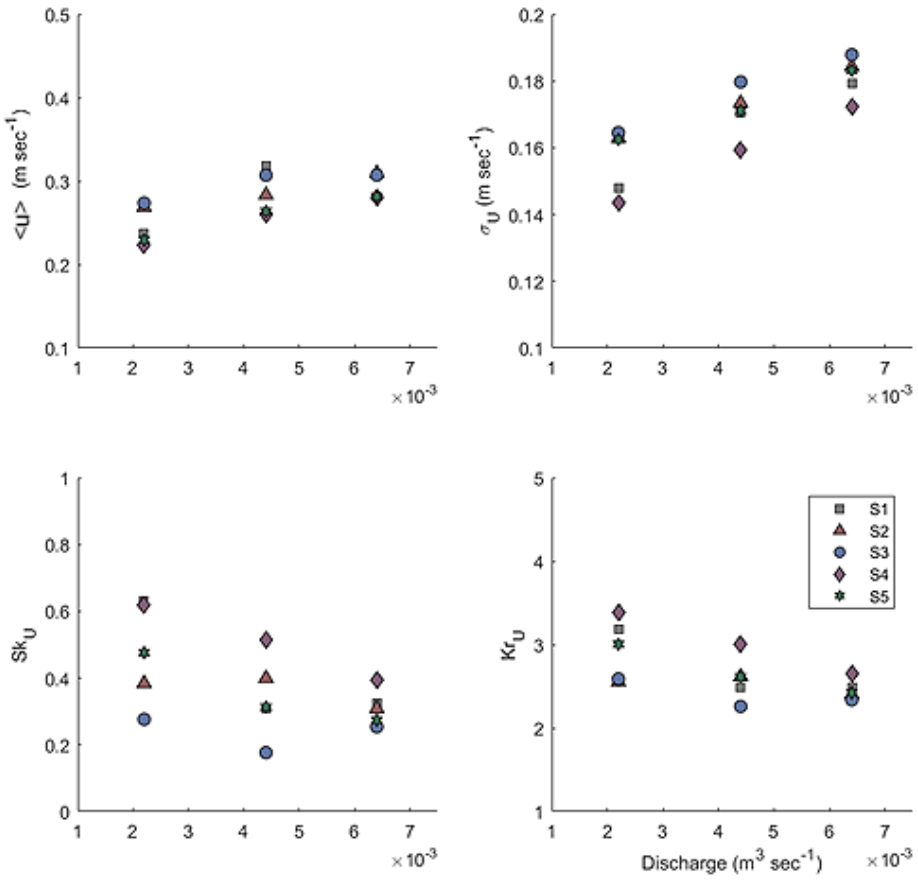

Figure 6.5: The relation between discharge and flow properties of streamwise velocity

Table 6.1: A summary of the statistical properties of the distributions of the streamwise and lateral velocity, where $\langle u \rangle$ and $\langle v \rangle$ are the spatially-averaged velocity over the inundated area, σ_u and σ_v are the standard deviation and Sk_u, Sk_v, Kr_u and Kr_v are the skewness and kurtosis of the distributions.

Property	S1			S2			S3			S4			S5		
	h	m	l	h	m	l	h	m	l	h	m	l	h	m	l
$\langle u \rangle$ (m sec^{-1})	0.34	0.34	0.26	0.34	0.32	0.30	0.34	0.34	0.31	0.32	0.31	0.27	0.33	0.31	0.28
σ_u (m sec^{-1})	0.18	0.17	0.15	0.18	0.17	0.16	0.19	0.18	0.16	0.17	0.16	0.14	0.18	0.17	0.16
Sk_u	0.32	0.31	0.63	0.31	0.40	0.38	0.25	0.18	0.28	0.39	0.51	0.52	0.27	0.31	0.48
Kr_u	2.49	2.49	3.19	2.40	2.65	2.55	2.34	2.26	2.59	2.65	3.01	3.39	2.42	2.61	3.01
$\langle v \rangle$ (m sec^{-1})	-0.04	-0.04	-0.03	0.01	0.00	0.01	-0.02	-0.01	-0.01	-0.02	-0.02	-0.02	-0.03	-0.03	-0.04
σ_v (m sec^{-1})	0.10	0.10	0.09	0.11	0.11	0.10	0.12	0.12	0.12	0.14	0.13	0.12	0.14	0.14	0.13
Sk_v	-0.10	-0.09	-0.36	0.04	0.01	-0.08	0.15	0.20	0.09	0.00	0.07	0.11	-0.15	-0.16	-0.18
Kr_u	3.20	3.33	3.93	3.23	3.16	3.43	3.56	3.80	3.40	3.57	3.52	3.21	3.84	3.80	3.77
σ_u / σ_V	1.83	1.72	1.64	1.65	1.54	1.60	1.51	1.44	1.40	1.27	1.20	1.17	1.30	1.27	1.28

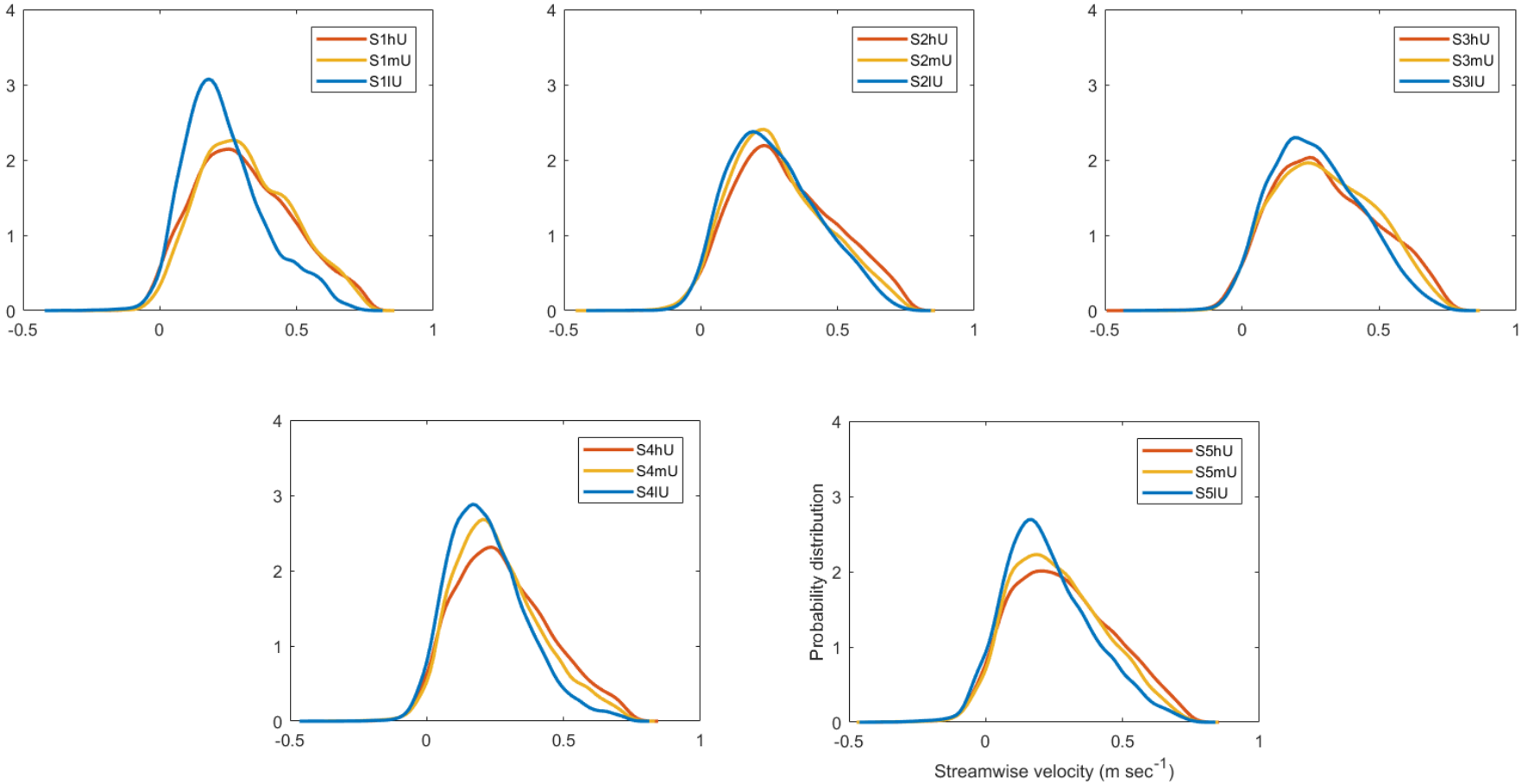

Figure 6.6: Probability distribution functions of streamwise velocity for each surface and different discharges.

6.4. Spatial distribution of lateral velocity

The lateral velocity provides important information on the degree of divergence of the flow within rill and interrill areas. The statistical properties of lateral velocity distributions are presented in Table 6.1. The spatial variation in the lateral velocity of each experiment were relatively low when comparing to streamwise direction. This was due to the physical characteristics of the eroded rills. Firstly, the span distance of the rills was narrower than the downslope distance, confining the width through which the water could flow. Secondly, according to the trajectories illustrated in Figure 6.3, the flows were mostly contained within the rills with very little flow occurred in interrill areas, and thus there was very little exchange of flow between rills hence the lower and less variable values. This last point is illustrated clearly in the pdfs in Figure 6.8a and b. The distribution peaks clearly centred around a lateral velocity of zero, and there are few large velocities. The pdfs and the statistics (Figure 6.8) reveal little variation in the distribution of velocities, apart from a slight tendency for lateral velocities to be more peak around zero at the lower discharges, owing to the lower inundation areas and increased confinement of the flow. The lateral velocity distributions fit into a Logistic distribution (AD <20).

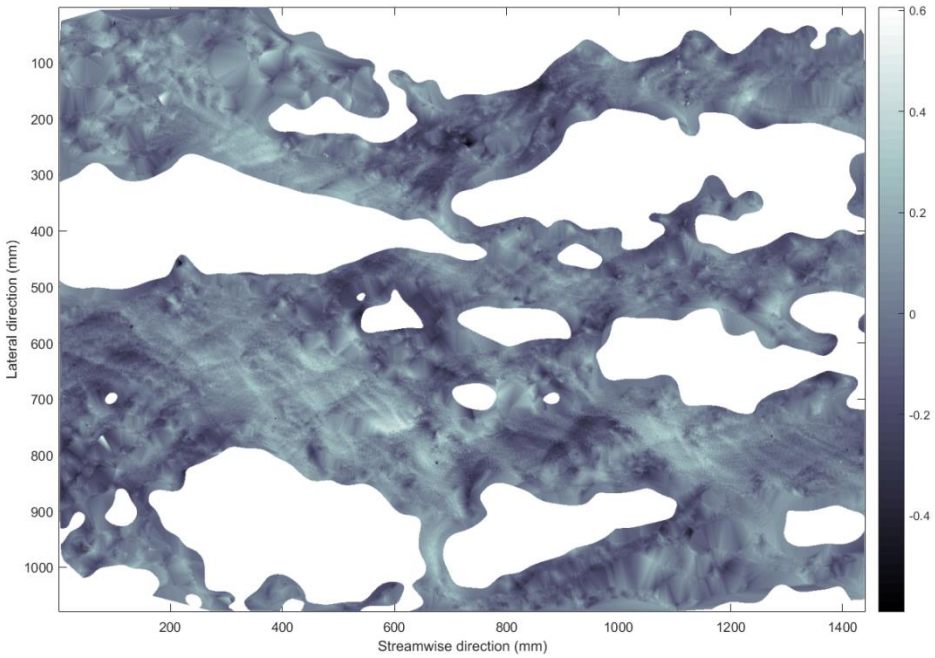

Figure 6.7: Example of the lateral velocity flow map from S2m.

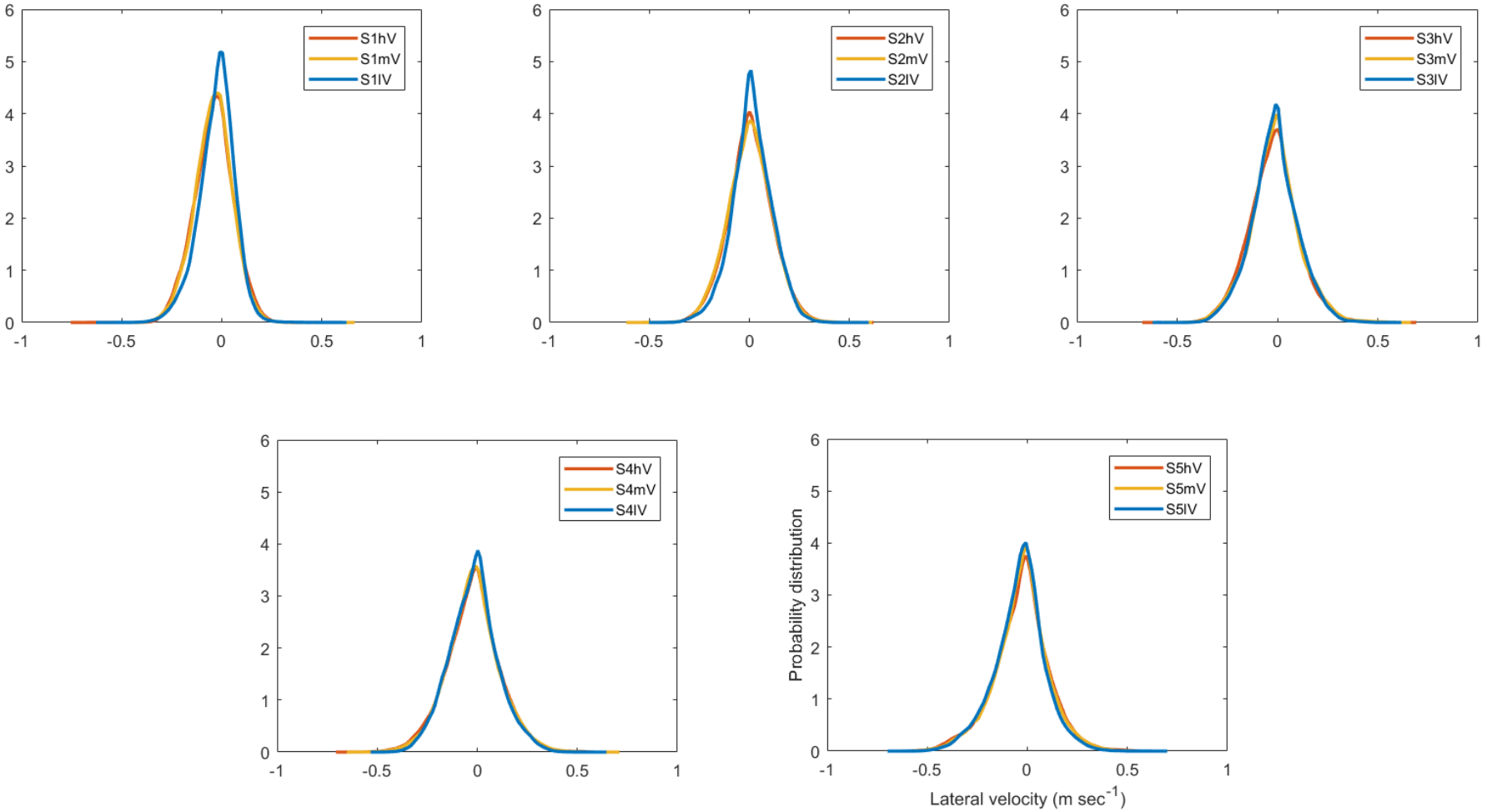

Figure 6.8: Probability distribution functions of a number of d the lateral velocity over each surface and different discharges.

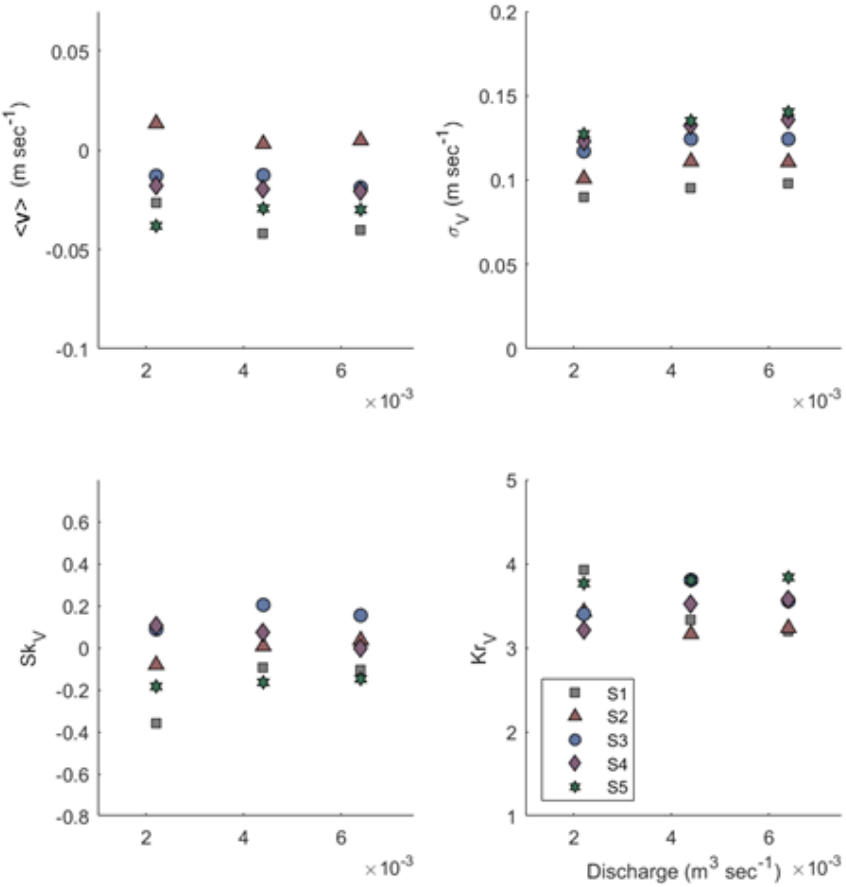

Figure 6.9: The relation between discharge and flow properties of lateral velocity

6.5. Summary

Streamwise and lateral velocities were tested to see how discharge influences the flow characteristics. Analyses focused on the properties and distribution of flow suggest that:

1. By looking at the flow maps, it can be seen that flows were more contained within the rills at low discharge rate. As inundation area increases due to higher discharge, flows were more independent from the rills are travel more on interrill areas.

2. Streamwise flow is the dominant flow direction due to downstream routing. The variation of the flow velocity in the streamwise direction was higher than that of lateral directions. This characteristic can also be observed from the results from

previous chapter as the lag at downstream direction is much higher than span direction also due to the routing of rills.

3. At higher discharge rate, the distributions of the flow velocities develop into a more uniform pattern. This can be observed from the decrease of the range of skewness and kurtosis. This implies that the flow velocities travel more randomly when they are independent from rill areas.

CHAPTER 7
Effect of micro-topography on patterns of overland flow

7.1. Introduction

In this chapter, the relationship between the microtopography of the rilled surfaces and overland flow are examined in the following ways. First, the PTV and SfM data are used to assess the level of correlation between overland flow velocity and surface elevation and roughness. Second, the effect of surface roughness, Reynolds number and relative submergence on hydraulic resistances is explored by estimating the Darcy-Weisbach friction factor. Third, the controls on the spatial patterns of drag force on a rilled surface are examined. These analyses are used to answer the following questions:

1. How does the microtopography of rilled surfaces control overland flow velocity patterns?

2. How does microtopography influence hydraulic resistance over a range of Reynolds numbers and relative submergences, and which factors have the strongest control?

3. What could be the erosion pattern of interrilled surface and what surface properties govern this pattern?

7.2. Visualizations of the effect of microtopography on the spatial patterns of overland flow

As described in earlier chapters, this test examined three overland flows over each of five rilled surfaces. In the digitally rendered illustration presented in Figure 7.1, five examples of the spatial patterns of overland flows are influenced by the surface rills are shown. These illustrations show that both the microtopography and the rills have a significant influence on the routing, number of threads and the velocity of the flows. These effects on the velocity field can be seen in more detail for each of the tests in Figure 7.2.

Flows tend to have higher concentration in deeper rills as presented in S2, S4 and S5. On the other hand, the areas with higher elevation have little influence on the flows since water travels mainly in the rills. S1 was the surface which had the flattest surface. In this case, the overland flows were spilt into just a small number of threads, and less concentrated which can be observed by the lower density of vectors. On the other hand, over S2, where there was a higher elevation range resulting in the flows being concentrated within the rills. This behaviour is illustrated by the high density of vectors in the lower elevation areas. Such behaviour is also present over surfaces S3 to S5 where rill channels were deeper still.

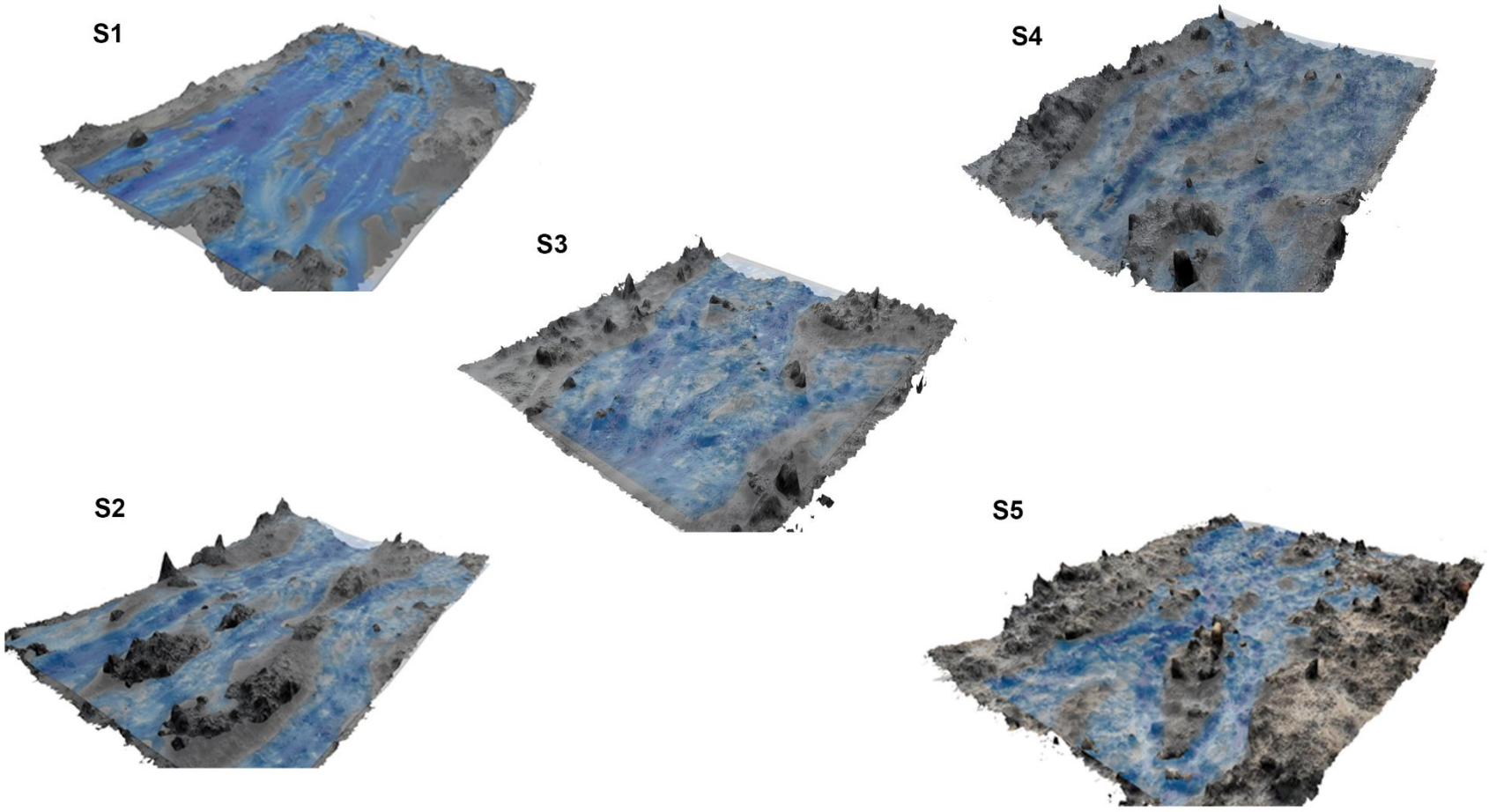

Figure 7.1: Examples of three-dimensional renders illustrating how the flow interacted with the microtopography. The elevation levels of the S1 to S4 were 5 times exaggerated while S5 was 3 times exaggerated.

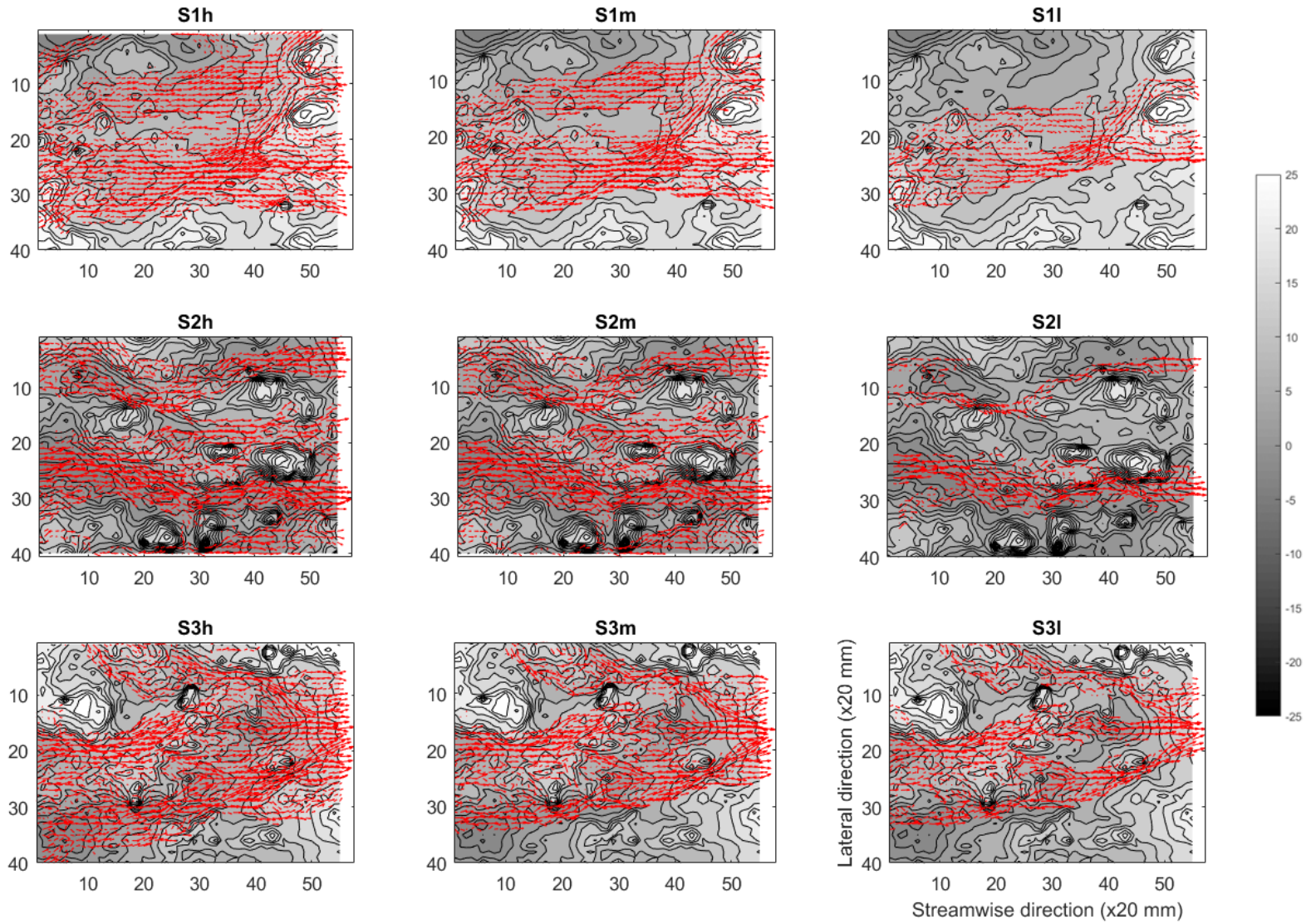

Figure 7.2a: Velocity vectors overlain on the surface elevations of surfaces S1 to S3. The flow direction is from left to right. The scale of the greyscale is mm.

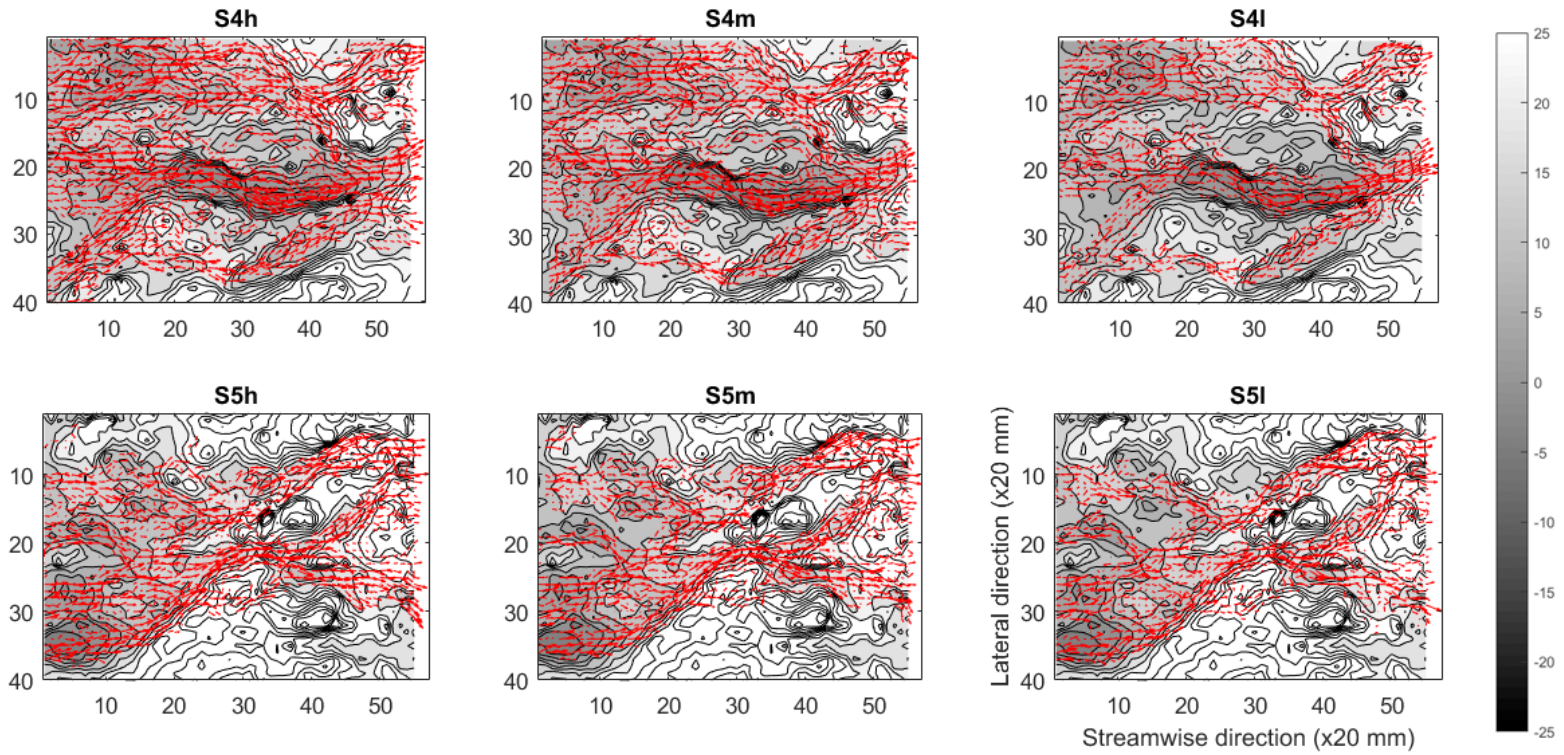

Figure 7.2b. Velocity vectors overlain on the surface elevations of surfaces S4 and S5. The flow direction is from left to right. The scale of the greyscale is mm.

7.3. Correlation between surface elevation and overland flow velocity

To quantify how closely these velocity patterns are related to the soil microtopography, a discrete variable correlation was performed. In order to make a direct correlation, the velocity fields were georeferenced to the DEMs, and the DEMs downscaled to a grid resolution to match that of the velocity fields (10 ×10 mm). Areas with no flow inundation were excluded from the correlation analysis.

The correlation was calculated, grid-to-grid, using the equation below:

$$R_{(z,u)} = \frac{\sum_{i=1}^{N}(z_i u_i)}{\sqrt{[\sum_{i=1}^{N}(z_i)^2][\sum_{i=1}^{N}(u_i)^2]}} \quad (7\text{-}1)$$

Where R is the correlation coefficient of the velocity field in relation to surfaces' elevation and i, j is the grid coordinates. Values of -1 or 1 indicate a perfect correlation and values of zero indicate no correlation. Equation (7.1) was used to examine the level of correlation between surface elevation and the streamwise, lateral and absolute velocity.

7.3.1. Streamwise velocity

The level of correlation between the surface and streamwise velocity, and how this was affected by the various surface properties are shown in Figure 7.3. The correlation coefficients reveal a large change in the level of correlation between the different surfaces. Typically, the level of correlation increases with steeper slope and the surface roughness. At the lowest slopes and lowest levels of roughness, the correlation is weak but this increases to correlation coefficients values close to -0.6 over the rougher and steeper surfaces, indicating a good level of

correlation. The correlation is particularly weak for surface S1. This is because S1 has a noticeably flatter surface than the other surfaces that resulted in less concentration of the flow, and more interrill flow (Figure 7.2a). On the other hand, the highest correlation coefficient for S2 could result from a much higher variation of rill elevation over the surface and the formation of distinct threads of flow (Figure 7.2a). Surfaces S2, S4 and S5 have similar correlation coefficients reflected in the more similar spatial patterns of flow and elevations (Figure 7.2). Each of these surfaces have clearly defined rills concentration of flows within these rills.

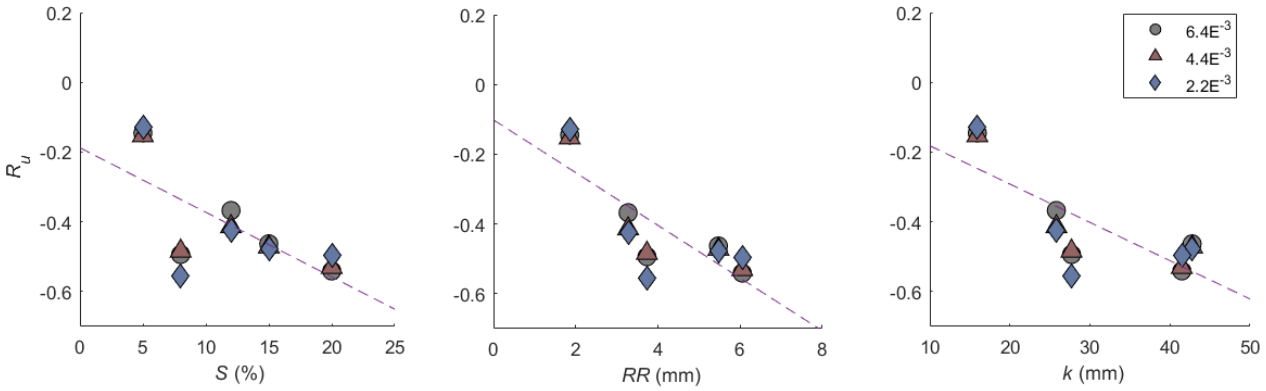

Figure 7.3: Correlation coefficient for streamwise velocity and elevation, and its variation with surface properties. *S* is the slope of the surface in percentage, *RR* is the random roughness and *k* is the range of the elevation

The correlation coefficients were also plotted against inundation ratio (*<h>/k*) and discharge (*Q*) to evaluate the relationship (Figure 7.4). The level of correlation is relatively high when inundation level is partially and marginally inundated. The level of correlation tends to decrease when well-inundated which is reflected from the inundation ratio. This relationship confirms that flows threads and routs when inundation level is within or around the rill heights. Discharge, on the other hand, does not seem to have any systematic effect on the correlation level.

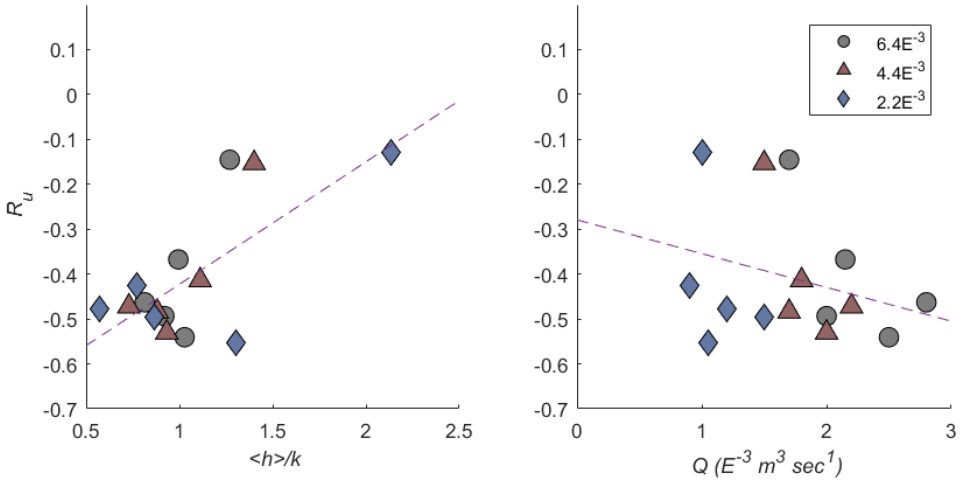

Figure 7.4: Correlation coefficient for streamwise velocity, and its variation with inundation ratio, $<h>/k$ and discharge rate, Q

7.3.2. Lateral velocity

As learnt from Chapter 5, the lag values of lateral direction l_{y0} are relatively lower than l_{x0} (i.e. streamwise lag). As a result, the correlation between surface and flow were expected to be low. The correlation coefficients in Figure 7.4 reveal that although the surface topography may influence the routing and threading of the flow (Figure 7.2), it has a negligible association with lateral velocity. This weak correlation is likely because the narrowness of the rill channels leads to overland flows having limited space to travel in the lateral direction. The level of correlation displays no systematic variation with slope or surface roughness, possibly reflecting the much lower elevation correlation lengths scales in the lateral direction than in the streamwise direction.

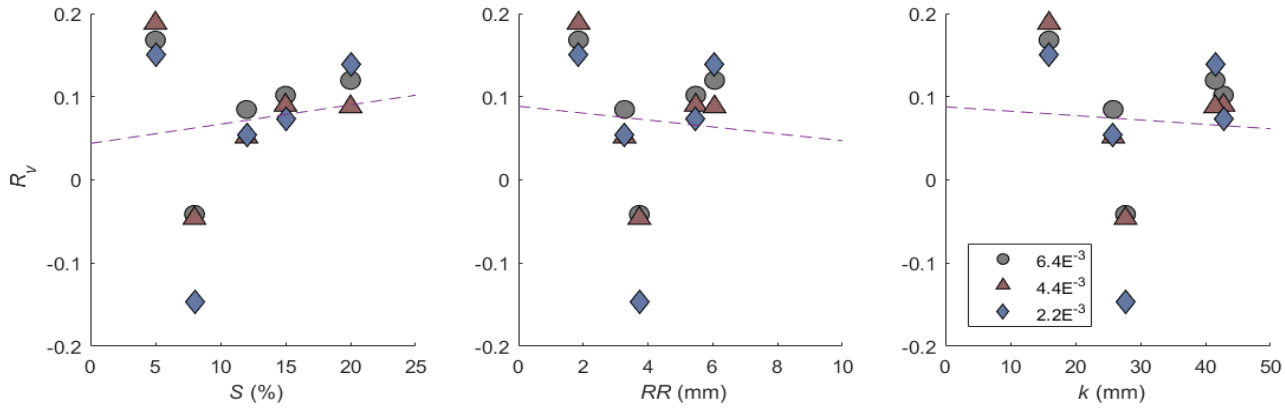

Figure 7.5: Correlation coefficient for lateral velocity and elevation, and its variation with surface properties

7.3.3. Absolute velocity

The correlation coefficients for the absolute velocity are almost exactly the same as for the streamwise velocity, and show a similar variation with slope and surface roughness (Figure 7.5). This result reveals that streamwise velocity and the correlation with the surface (in particularly the streamwise-directed rills), dominates the overall spatial pattern of overland flows. The systematic relevance of correlation coefficient levels and surface properties presented at streamwise velocity can be used to explain the relationship of absolute velocity.

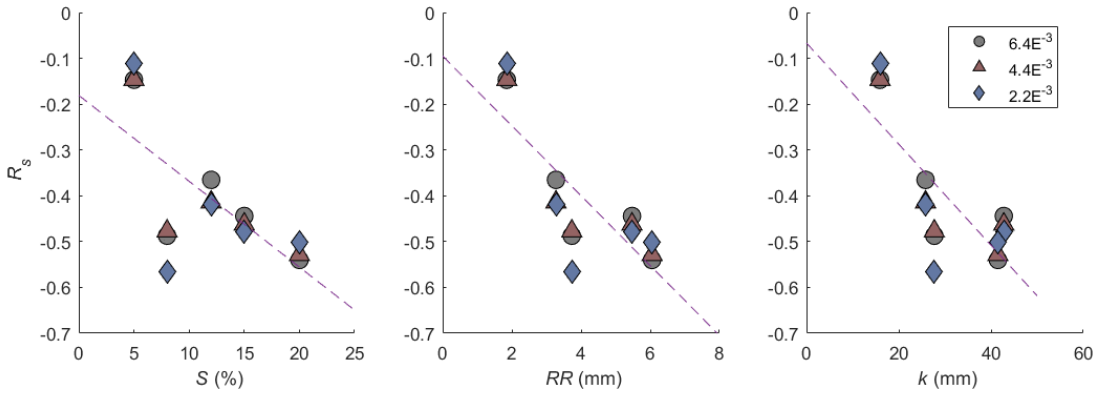

Figure 7.6: Correlation coefficient for absolute velocity and elevation, and its variation with surface properties

7.4. Correlation between local roughness and overland flow velocity

When comparing the correlation coefficient acquired from this method to flow against elevation, a clear difference is presented. The correlation coefficient from streamwise direction and absolute velocity fluctuate from about 0.61 to about 0.73. This can be inferred that local roughness have higher influence on flow velocities than surface elevation.

The correlation coefficients were plotted against surface properties similar to 7.3. Correlation coefficient level of high discharge ($6.4E^{-3}$ m^3 sec^{-1}) flows seem to stabilise, maintaining *R* values of 0.65 and 0.66 despite the change in surface properties. Lower discharges on the other hand are dependent on surface properties. The flows at $2.24E^{-3}$ m^3 sec^{-1} discharge gradually decrease when greater surface properties were applied. At inundation ratio from 0.5 - 1.5, the correlation coefficient varies between 0.60 and 0.68 with low discharge rate fluctuating most. Discharge rate does not possess any systematic relationship to the coefficients.

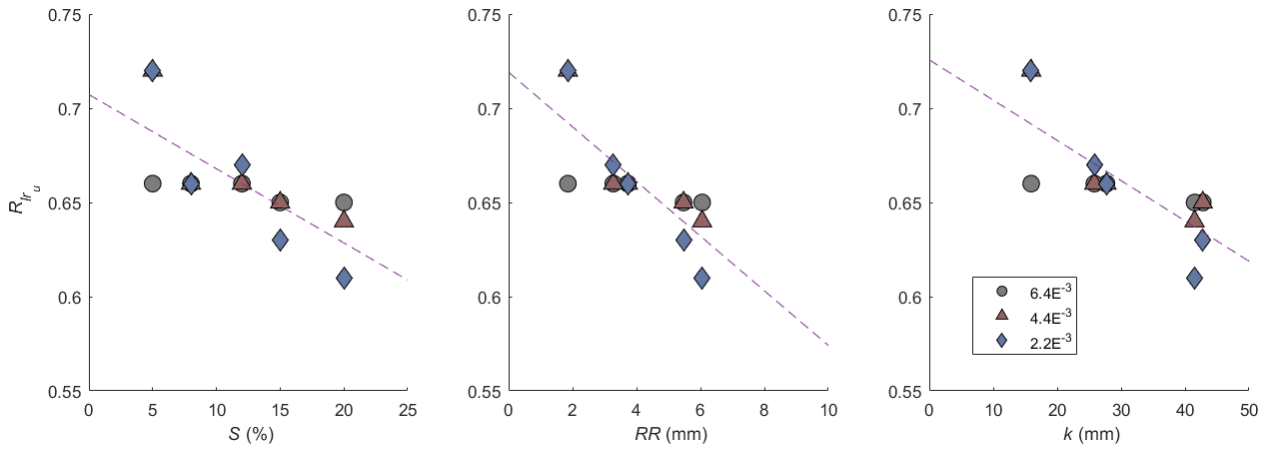

Figure 7.7: Correlation coefficient for streamwise velocity and local roughness (R_{lru}), and its variation with surface properties.

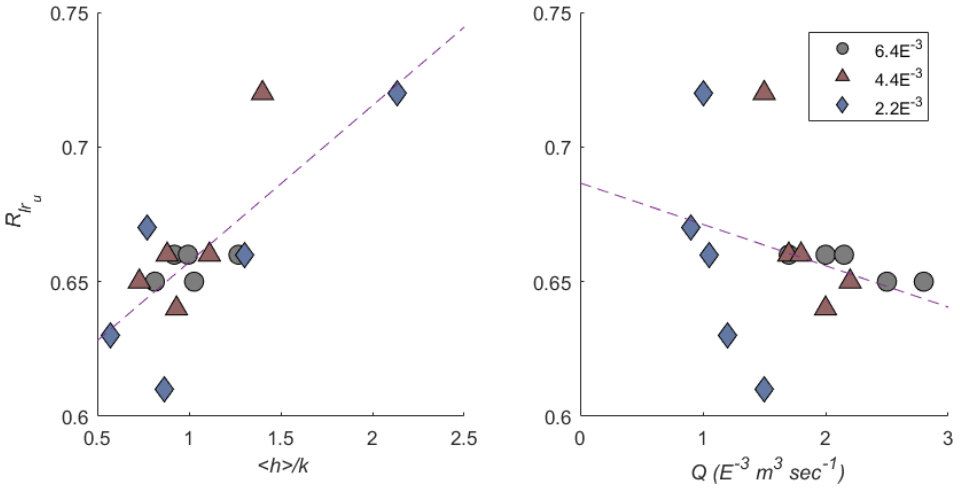

Figure 7.8: Correlation coefficient for streamwise velocity and local roughness and its variation with inundation ratio and discharge

7.5. Effect of surface roughness on flow resistance

To examine the effect of bed roughness on hydraulic resistance, the Darcy-Weisbach friction factor was used. This equation was chosen because it is commonly used to predict overland flow velocity (e.g. Gilley *et al.*, 1992; Smith *et al.*, 2011; Legout *et al.*, 2012). Assuming

uniform and steady flow conditions, the Darcy-Weisbach friction factor, f can be calculated from the modified equation:

$$f = \frac{8g\langle h \rangle S}{\langle u \rangle^2} \tag{7-2}$$

Where g is the gravitational acceleration, $\langle h \rangle$ is the spatially-averaged flow depth (values are presented in Chapter 6), S is the slope of the surface and $\langle u \rangle$ is the spatially-averaged streamwise velocity. When the channels are non-rectangular in shape, $\langle h \rangle$ can be replaced with the hydraulic radius (e.g. Abrahams *et al.*, 1986; Gilley *et al.*, 1992).

In many studies, the Darcy-Weisbach friction factor is correlated to the Reynolds number in order to model hydraulic resistance (Abrahams *et al.*, 1986; Gilley *et al.*, 1992; Smith *et al.*, 2011). In Figure 7.9, the Darcy-Weisbach friction factor calculated from surfaces S1 to S5 are shown. These results show some tendency for the friction factor to increase with Reynolds number, particularly so at the two highest discharges. At the highest discharge the R^2 values for the fitted relationship between f and Re is 97.6 %, 70.4% at the mid-discharge but just 1.9% for the lowest discharge. This shows that this relationship only holds when the flows are fully turbulent (i.e. Re >> 4000) and not when they are close to being transitional, such as for shallow, interrill flows.

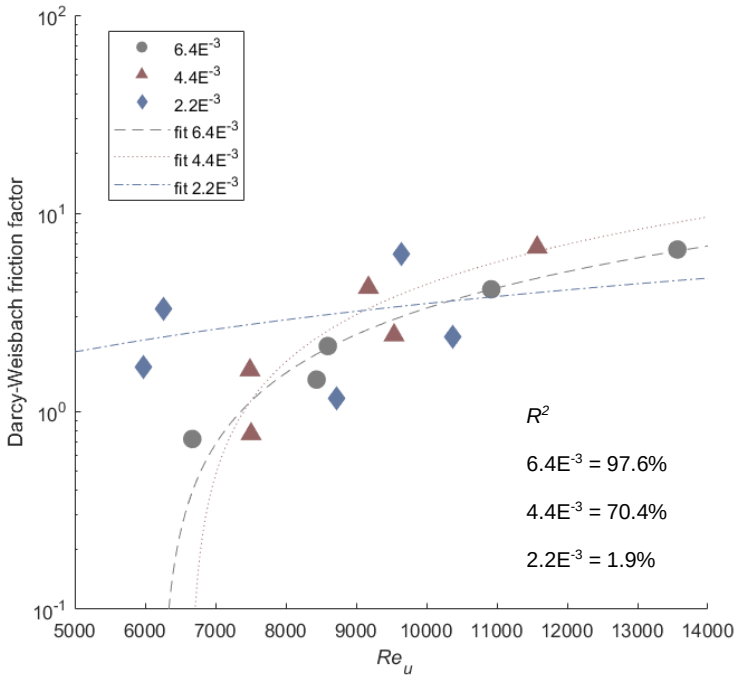

Figure 7.9: Darcy-Weisbach friction factor as a function of *Re*.

The results in Figure 7.6 suggest that other factors are likely important in determining the hydraulic resistance. Figure 7.8 reveals that *f* has a strong power relationship with surface roughness (random roughness and elevation range). Fitted power equations show that *RR* has the strongest influence on *f* with a R^2 value of 85.94%, and *k* has a R^2 of 72.19%. The friction factor also has a power relationship with relative submergence, albeit a weaker relationship than observed with surface roughness. But interestingly, a stronger relationship than was seen with Reynolds number. This result is not surprising given that lower submergence flows are more roughness dominated, and that two flows with the same Reynolds number but at different slopes will exhibit a different relative submergence, and thus be dominated by surface roughness by differing degrees.

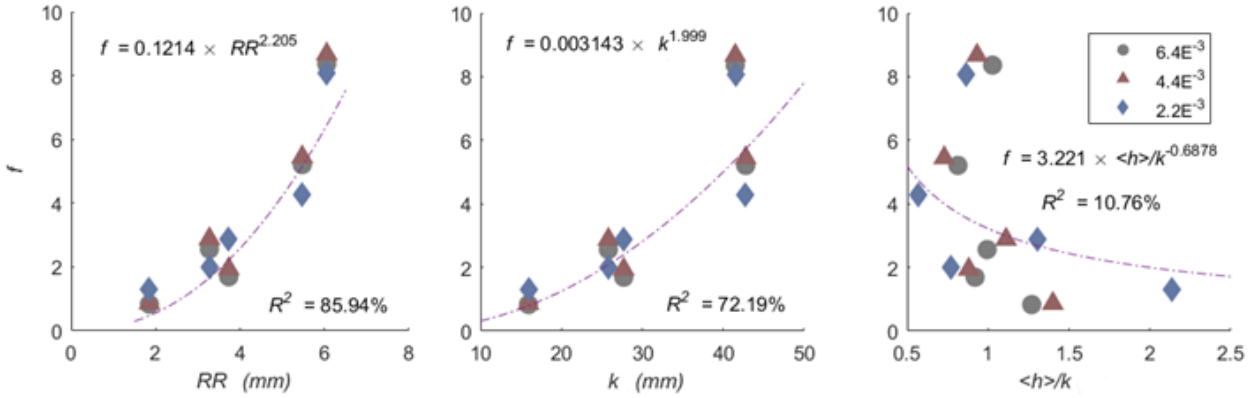

Figure 7.10: Surface properties vs Darcy-Weisbach friction factor.

7.6. Effect of topography on spatial patterns of fluid drag

The drag force experienced by the surface is a direct measure of hydraulic resistance and determines the entrainment of sediment. Thus knowing how its distribution varies over a soil surface is important for determining the effect of topography on resistance and erosion patterns. Using the georeferenced DEMs used in the correlation analysis above, the drag force f_D experienced by each cell i, j of the surface was calculated by:

$$f_{D(i,j)} = 0.5\,\rho\,C_D\,A(i,j)\,u^2_{(i,j)} \tag{7-3}$$

where ρ is the density of water, A is the frontal area exposed to the flow (determined from the DEM), u is the velocity of the flow and C_D is the drag coefficient of soil, which was estimated using the following:

$$C_D = \left[\left(\frac{32}{Re}\right)^{2/3} + 1\right]^{3/2} \tag{7-4}$$

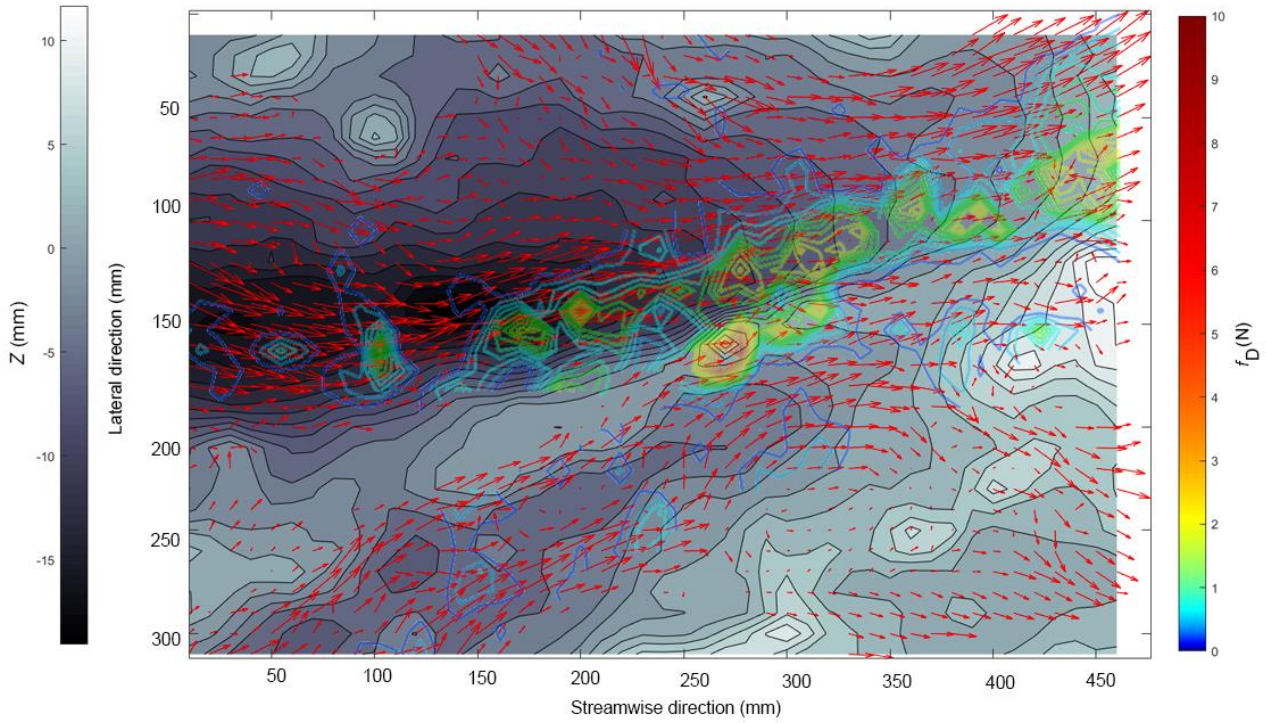

Figure 7.11: Enlarged proportion of S4h showing the drag force interacting with the velocity field and surface elevations

Figure 7.11 shows an example of how the drag force can be visually correlated with the velocity field and the surface topography. These results, presented here for S4h ($6.4E^{-3}$ m^3 sec^{-1}), show a high level of spatial variance. Large areas of high drag, that extend for a distance of more than 200 mm, coincide with the convergence of flows from two rills at a streamwise and lateral position of 250 mm and 150 mm. High drag is also produced when flows converge from above at a similar streamwise position and a lateral position of 100 mm. These high drag areas often coincide with the walls of the rills. The drag force distributions for all the tests show the same relationship with topography, and show that discharge has a small influence on this pattern when distinct rills are present and flow is more correlated with the topography (S2-S5;

Figures 7.11a and b; see Figure 7.3), and a greater influence when there is greater interrill flow and lower levels of correlation (S1; Figure 7.11a; see Figure 7.3).

Examples of the pdf's of the drag force distributions are shown in Figure 7.13, revealing clear differences in their shape and magnitude between the different surfaces. From distribution identification analysis, two-parameter Weibull distribution fits best with f_D (Anderson-Darling factor <15). Distribution parameters hold the potential to predict certain characteristics (e.g. Nearing *et al.*, 1997; Parsons and Wainwright, 2006). In this study, the scale, λ_{wbl}, and shape, K_{wbl}, parameters of the Weibull distribution were used. Equations for Weibull distribution is as followed:

$$f_{wbl}(x) = \frac{K}{\lambda}\left(\frac{x}{\lambda}\right)^{K-1} exp^{-(/\lambda)^K} \quad (7\text{-}5)$$

Table 7.1: Weibull distribution parameters acquired from f_D

	λ_{wbl}			K_{wbl}		
	$6.4E^{-3}$	$4.4E^{-3}$	$2.2E^{-3}$	$6.4E^{-3}$	$4.4E^{-3}$	$2.2E^{-3}$
S1	0.10	0.10	0.05	0.61	0.64	0.59
S2	0.13	0.11	0.10	0.58	0.57	0.56
S3	0.16	0.15	0.12	0.58	0.57	0.58
S4	0.16	0.15	0.11	0.55	0.55	0.54
S5	0.29	0.25	0.20	0.55	0.55	0.53

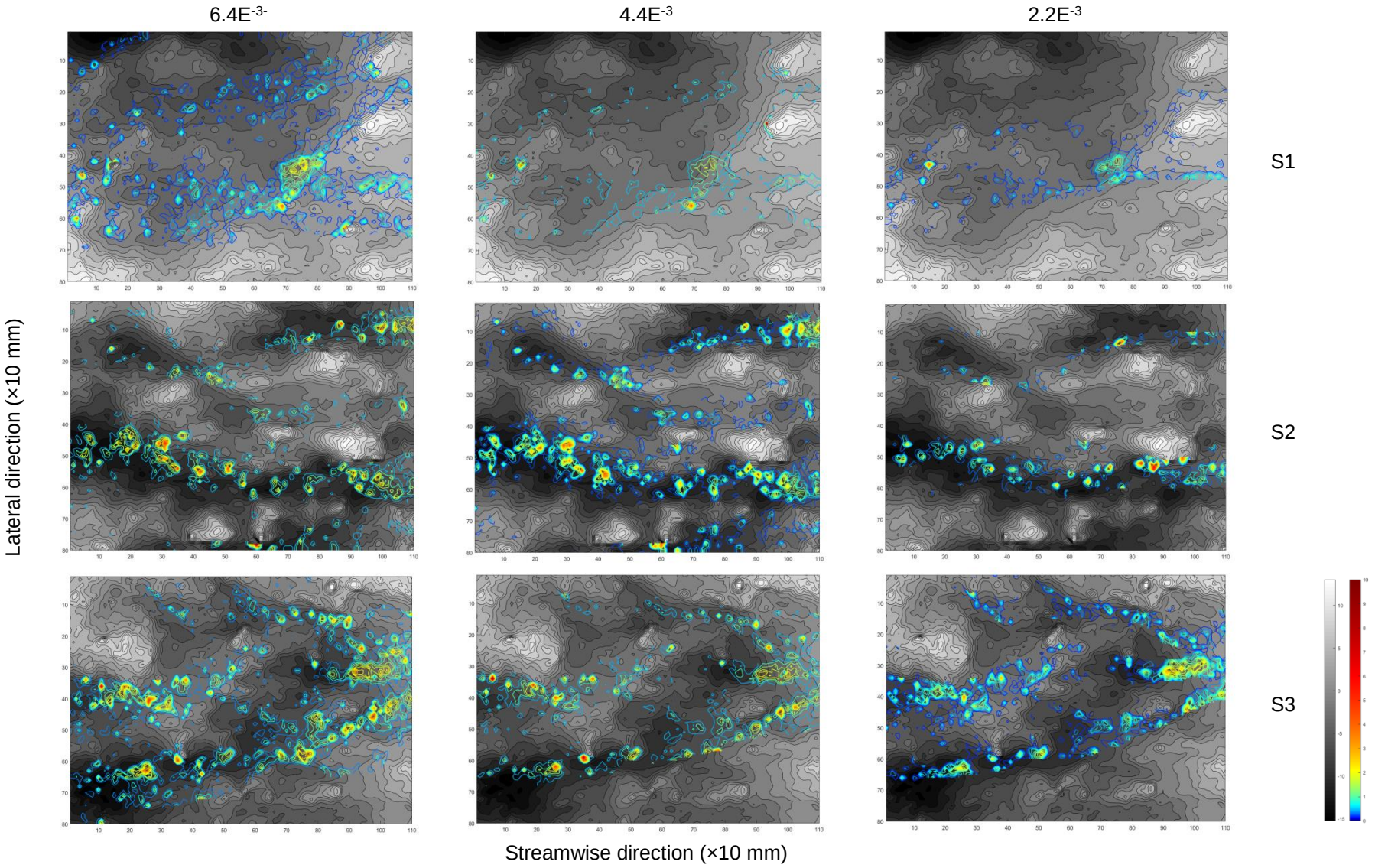

Figure 7.12a: Drag force map of surfaces S1-S3 at different flow discharges.

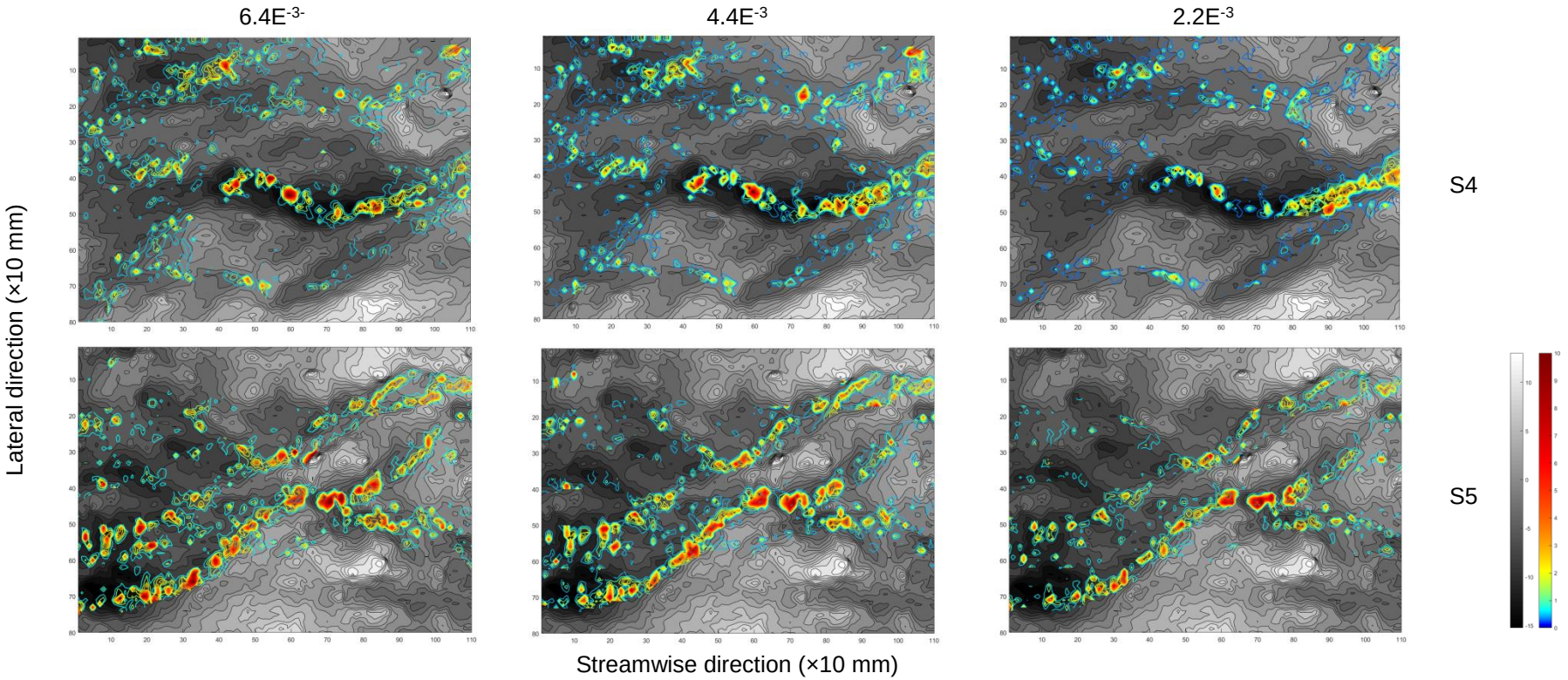

Figure 7.12b: Drag force map of surfaces S4-S5 at different flow discharges.

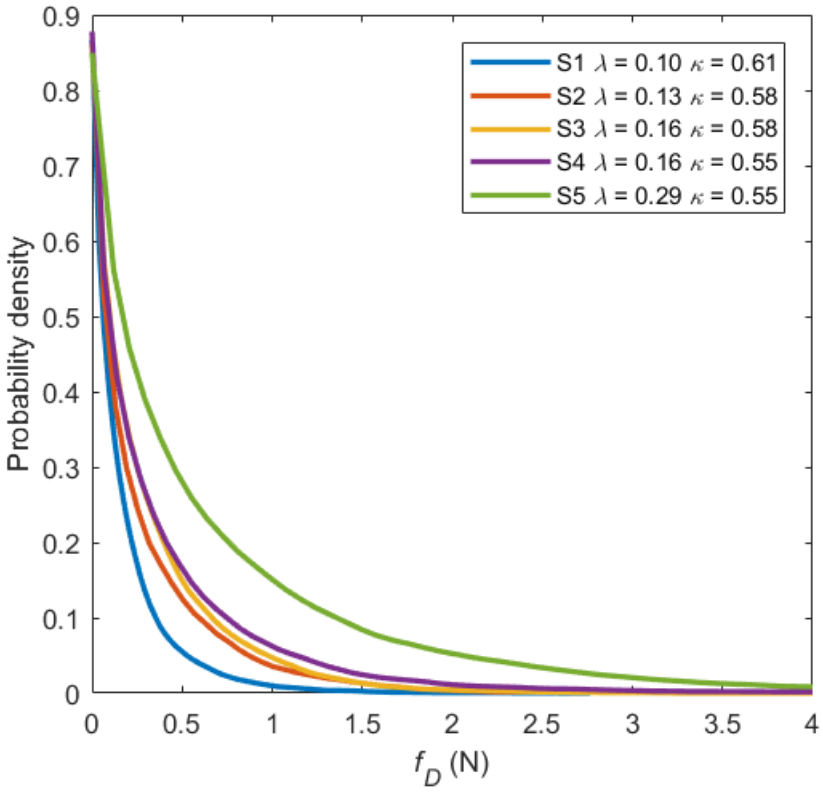

Figure 7.13: Examples of probability distribution of surfaces S1 to S5 at 6.4E^{-3} m^3 sec^{-1} discharge.

To examine the factors that influence the distributions, the variation in the scale and shape parameters with surface roughness, hydraulic resistance and relative submergence were examined (Figure 7.14, 7.13 and 7.14). The results reveal that the distributions are all affected, in a systematic way, by these factors. The changes in the scale parameter reveals that, typically, the drag force increases with a rise in roughness, hydraulic resistance and relative submergence. Fitted exponential (f) and power (RR) equations show that these changes were most well associated with changes in f (R^2 = 78.36%) and RR (R^2 = 59.19%). The results for the shape parameters reveal opposing trends with these factors, showing that the distributions are typically more peaky and less uniform for surfaces that are rougher and more resistant, and for

flows that have higher submergence. This parameters changes most consistently with *RR* (R^2 = 80.09%), followed by *k* (R^2 = 78.62%) and *f* (R^2 = 77.345%).

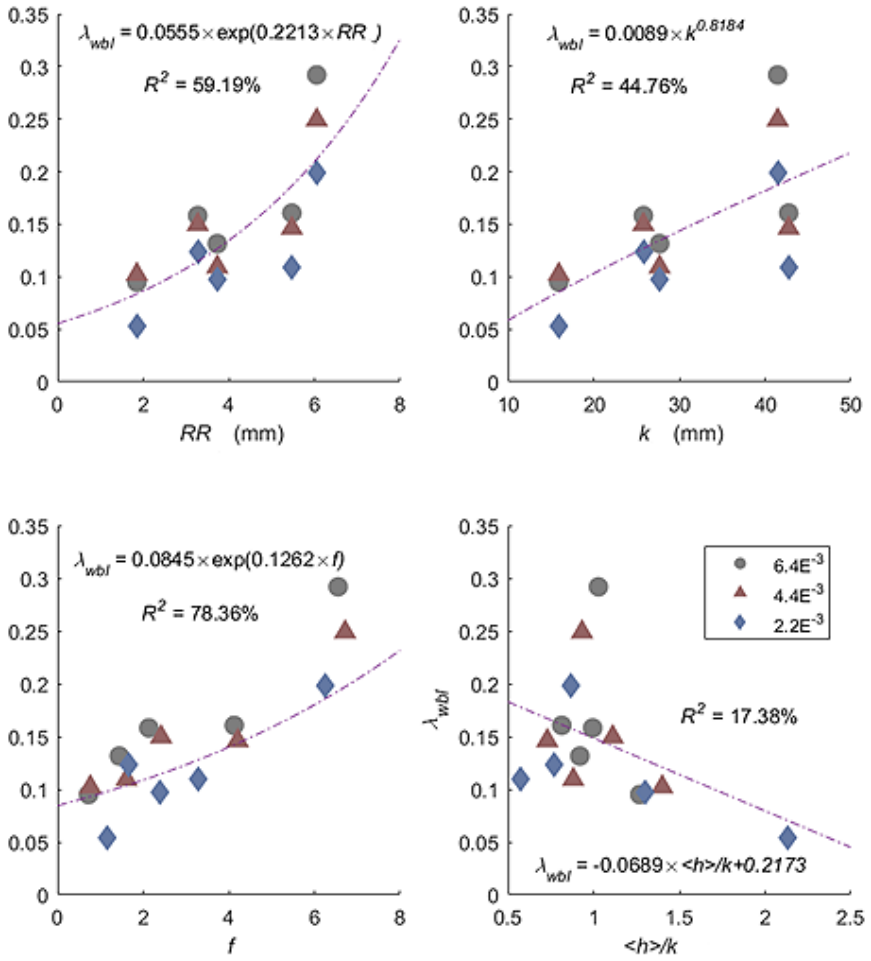

Figure 7.14: Weibull scale parameter, λ_{wbl}, acquired from drag force distribution against *RR*, *k*, *f* and *<h>/k*

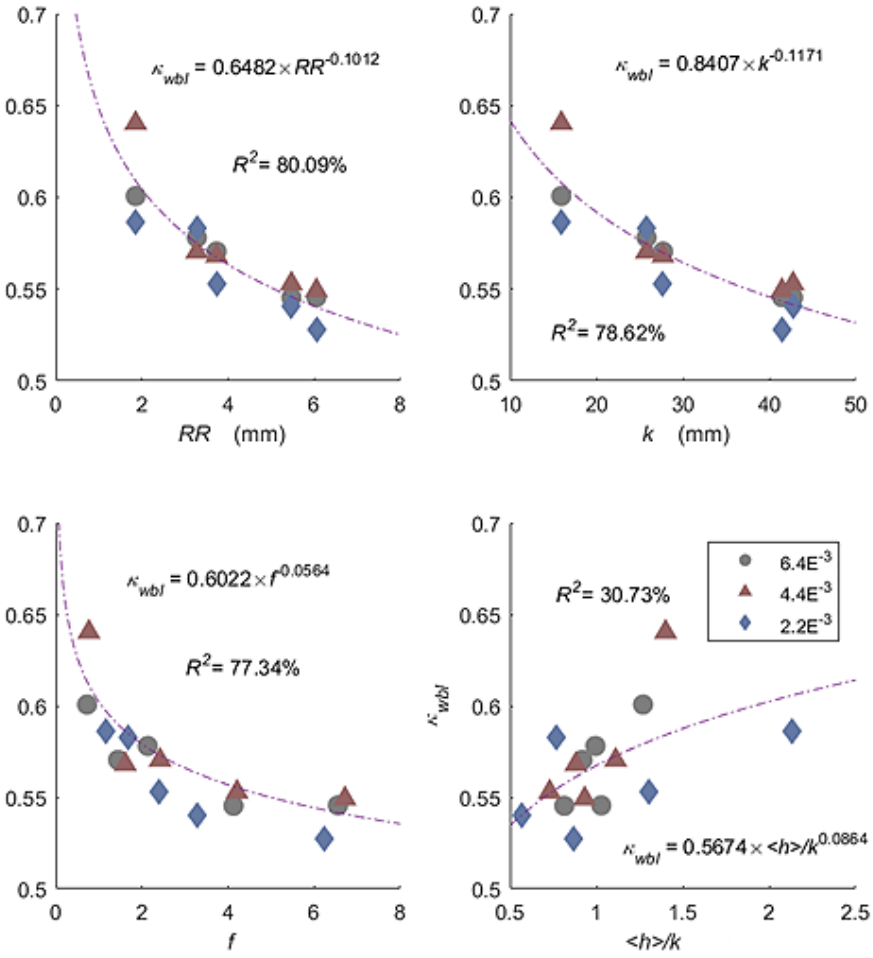

Figure 7.15: Weibull shape parameter, *K*, acquired from drag force distribution against *RR*, *k*, *f* and *<h>/k*

7.7. Summary

Several analyses were performed to evaluate the relationship between surface and flow characteristics. Firstly, correlation of discrete variables were performed to determine the correlation coefficient of surface properties and flow velocities at different flow directions. Secondly, flow resistance was calculated using Darcy-Weisbach friction factor. This resistant factor was tested against Reynolds number and different surface properties to determine the

relationship. Finally, high-resolution fluid drag was measured to see the potential erosion pattern. Key findings from this chapter are as listed:

1. The level of correlation between overland flow velocity and surface elevation was shown to increase with a rise in bed slope and roughness. Only at the higher slopes and levels of roughness was the streamwise velocity and absolute velocity reasonably well correlated with the surface elevation.

2. The hydraulic resistance, estimated by the Darcy-Weisbach friction factor, varied strongly with the Reynolds number when the flows were fully turbulent (i.e. Re >> 4000) but not when they were close to being transitional, such as in shallow, interrill flows. Surface roughness and relative submergence were found to have a greater or equally strong control as Reynolds number on hydraulic resistance.

3. The drag force distributions showed high levels of spatial variation over the rilled surfaces. Areas of high drag forces correlated with the walls of rills and with areas in which flows converged from different rills. The distributions were shown to be heavily dependent upon surface roughness and hydraulic resistance, and to a lesser extent, relative submergence. The strength of these relationships revealed the potential to predict the drag force distribution, and thus spatial patterns of hydraulic resistance and erosion, based on these simple parameters.

CHAPTER 8
Discussion

8.1. Introduction

This Chapter brings the findings of the previous Chapters together to interpret and then consider the significance of the main outcomes of the research. The Chapter will begin by discussing whether the statistical properties of eroded soil surface can be estimated, followed by whether overland flow properties can be predicted based on these properties. The Chapter will also examine the implications of the observed spatial patterns of overland flow on soil erosion. Finally, there will be a discussion of the future avenues of research in this area.

8.2. Estimating eroded soil surface properties from hillslope gradient

In Chapter 5, a series of rainfall events were simulated over five surfaces on different hillslope gradients. The tests showed that the depth and severity of the rills were highly dependent on the slope of the surface, as one might expect (e.g. Berger *et al.*, 2010) given the positive correlation between slope and erosion rate. This dependency was reflected in RR (random roughness, σ) and k (elevation range) having a power relationships with slope (R^2 = 86% and 81.6% respectively). For a 110 mm hr^{-1} rainfall intensity over a duration of 20 minutes, the random roughness and range of the rills can be estimated empirically by the following:

$$RR = 0.62 \times S^{0.76} \quad (8\text{-}1)$$

$$k = 6.4 \times S^{0.64} \quad (8\text{-}2)$$

when S is the percentage of slope. Furthermore, the skewness of the distribution of surface elevations showed a strong negative relationship with slope, reflecting the greater rilling on the surface (R^2 = 84.8%)

$$Sk = -0.12 \times S + 0.56 \quad (8\text{-}3)$$

The kurtosis was fairly invariant with slope, attaining a value between 3 and 4.5. Together these relationships reveal the potential to estimate soil surface roughness and the distribution of elevations based on just one, simple, easy-to-measure, parameter. Further tests over a range of different rainfall events and soils are required to test this potential.

On the other hand, correlation length scales derived from second-order structure functions showed no clear relationship with slope. In fluvial studies, these length scales have been shown to provide a representative estimate of grain roughness and the structure of the bed (e.g. Nikora *et al.*, 1998; Cooper and Tait, 2009; Mohajeri *et al.*, 2015). For eroded soil surfaces, where both grain and form roughness (primarily rills) are present, the lack of relationship with slope appears to suggest these length scales provide a poor representation of surface structure.

8.3. Spatial properties overland flow

Overland flow velocity is commonly estimated using hydraluic resistance equations (e.g. Darcy-Weisbach, Mannings) that are based on the assumption that the flow is uniform and 1D (Smith et al., 2007). The vector fields and flow inundation areas in Chapter 5 demonstrate that this assumption does not hold for the investigated surfaces. The streamwise and lateral velocities showed considerable spatial variance over the plot, revealing the flow was 2D. This was particularly evident at the higher flow dischrages and relative submergences, in which the spatial variability in streamwise velocity was higher and the distributions were wider, flatter and more skewed. The changes in spatial varaibility with relative submergence are the same as those obeserved for 2D flows over fluvial, gravel surfaces (Lamarre and Roy, 2005; Cooper, 2012; Rice *et al.*, 2014). But the changes in the distributions are not the same (Cooper, 2012), reflecting that the area of inundation increases, and the flow becomes less concentrated into the rills over hillslopes, but not so for fluvial, within-channel flows.

8.4. Estimating overland flow hydraulics using surface properties from SfM-derived DEMs

8.4.1. Overland flow velocity

The results in Chapter 7 revealed that the level of correlation between the surface elevations and streamwise velocity increased with plot slope, surface roughness and minimally with inundation ratio. This rise coincided with an

increase in the depth and severity of rilling, showing that interrill flows are poorly correlated with the surface elevations. Even over the rilled surfaces, the correlation values were not sufficiently high (negative or positive) to suggest that overland flow velocity can be predicted based on a DEM alone. There are no similar studies for hillslopes, so it remains unclear whether the correlation may be higher for more eroded surfaces, or those with a greater range of grain sizes. Furthermore, the presented results are for surface velocities and one would expect the correlation to increase close to the surface. However, rather interestingly, the correlation values match very well those of Cooper and Tait (2008) who examined the same correlation for near-bed velocities over fluvial, gravel beds.

The correlation between the local roughness and streamwise velocity was stronger, and was invariant with slope and relative submergence. This result suggests that incorporating local variations in surface elevations is a more valuable pursuit in the estimation of spatial patterns of overland flow velocity.

8.4.2. Overland inundation level

Erosion rates are sensitive to changes in the distribution of inundation level. Thus to accurately estimate flow detachment, not only do the spatial patterns of overland flow velocity need to be accurately estimated, but also those of depth (Abrahams *et al.*, 1989). Parsons and Wainwright (2006) suggested that a two-parameter Gambel distribution provided an appropriate depth model for interrill flow. The shape and location parameters of this distribution type were strongly correlated to discharge, and could be used to model the conditions under which

rilling will occur. Smith et al. (2011) on the other handed proposed that a two-parameter gamma distribution was as the optimum model for depths of both interrill and rill flows.

The model proposed by Smith *et. al,* (2011) was tested using surface elevation level from S5. The probability distribution functions of depth (*h*) for the three discharges over S5 are displayed in Figure 8.1. Identification of distribution type shows that the *h* of S5 has the same exponential distribution family as Parsons and Wainwright's (2006) and Smith et al.'s (2007) proposed models. However, the distributions are better fitted by a two-parameter Weibull distribution with Anderson-Darling (AD) factors of 5.95, 6.54 and 5.37 for discharges $6.4E^{-3}$, $4.4E^{-3}$ and $2.2E^{-3}$ m^3 s^{-1} respectively. The same set of data had AD values for a Gamma distribution of 9.35, 8.88 and 7.35, and 28.95, 31.10 and 31.80 for a Gambel distribution, respectively. The parameters of the Weibull distributions are also fairly similar for each discharge, contrasting to the results of Parsons *et al.*, (2006) and Smith *et. al.* (2007).

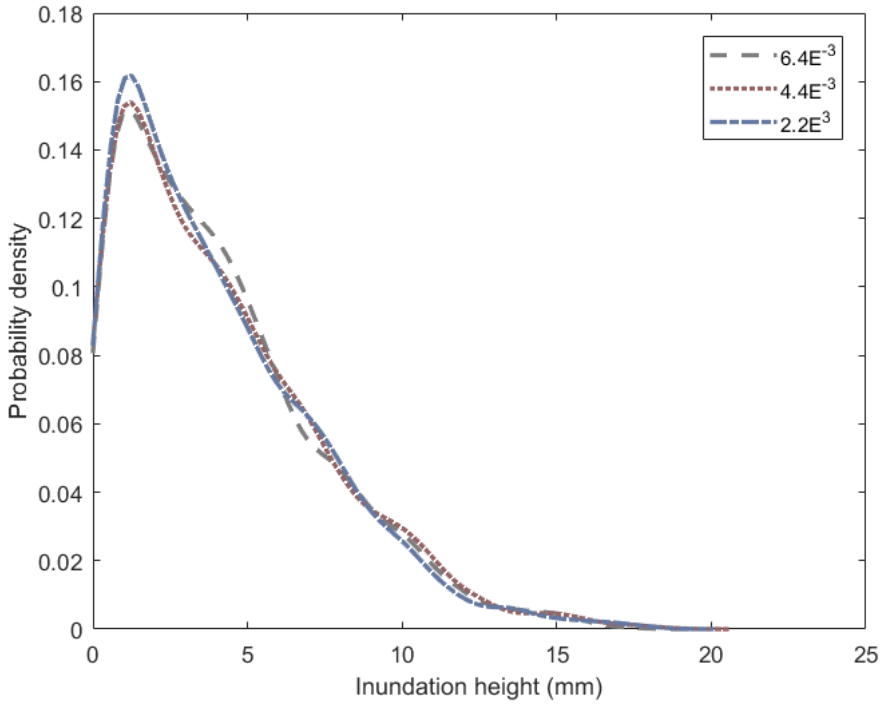

Figure 8.1: Flow inundation height distribution over surface S5 for three discharges ($m^3\ s^{-1}$)

8.4.3. Hydraulic resistance

The Darcy-Weisbach friction factor was highly correlated to surface roughness through a power relationship:

$$f = 0.1214 \times RR^{2.20} \quad (8\text{-}4)$$

$$f = 0.0031 \times k^2 \quad (8\text{-}5)$$

Albeit weaker, the friction factor was also well correlated with relative submergence, through the following relationship:

$$f = 3.221 \times \langle h \rangle / k^{-0.69} \quad (8\text{-}6)$$

This relationship was much stronger than was seen with Reynolds number. This result is not surprising given that lower submergence flows are more roughness dominated, and that two flows with the same Reynolds number but at different slopes will exhibit a different relative submergence, and thus be dominated by surface roughness by differing degrees. Overall, the results suggest that the friction factor cannot be estimated based on Reynolds number alone, and more physically reliable parameters, such as surface roughness and relative submergence, should be incorporated into the parameterisation of friction. The presented results differ somewhat from the bulk of previous work on the scaling of hydraulic resistance, because rather than using single-point measurements of velocity and inundation level, these estimates of the friction factor are based on spatially-distributed measurements. This difference may have allowed the greater sensitivity of friction factor to surface roughness and relative submergence to be revealed.

8.4.4. Surface drag force

The drag force distributions were well-approximated by a two-parameter Weibull distribution for all flows and surfaces. Since this distribution type is the same as found for inundation level, it reveals a consistent link between the microtopography and the organisation of the flow. The scale (λ_{wbl}) and shape (K_{wbl})

parameters of the Weibull distributions were most strongly correlated with the Darcy-Weisbach friction factor, through the following relationship:

$$\lambda_{wbl} = 0.06 \times \exp^{0.22 \times RR} \quad (8\text{-}7)$$

$$K_{wbl} = 0.60 \times f^{0.06} \quad (8\text{-}8)$$

The relationship between these parameters and random roughness was weaker, but still showed there is potential for estimating drag force distributions using the surface DEM.

8.5. The effect of spatial variability in overland flow

Interrill and rill erosion is spatially heterogeneous over hillslopes, with certain areas of the slope experiencing large erosion rates and other negligible erosion. The drag force was highly variable over the surface, with some areas experiencing forces an order magnitude higher than others. This result provides a physical explanation for this spatial heterogeneity in erosion rates. Since erosion laws are non-linear, this spatial variability in the flow can potentially cause large errors in the prediction of erosion when using conventional models that use a single shear stress, discharge or stream power value (amongst others). Large areas of high drag most often coincided with the convergence of flows from neighbouring rills and with the walls of the rills. This coincidence occurred because high velocity areas correlated with highly exposed microtopography. Thus the distributions of drag force also provide some explanation for why rills expand, deepen and migrate.

8.6. Future research avenues

8.6.1. Mobile surfaces

There is need to explore how the observed relationships with microtopography vary when the surface is mobile. The controls may become less strong (or clear) when there is body of particles moving above the bed, effectively reducing the effect of roughness on the flow. Furthermore, the influence of moving particles on the structure of the flow itself (damping effects) should be explored, as this effect has been shown to be important in open channel flows (Vanoni and Nomicos, 1959; Gust and Southard, 1983; Lorna *et al.*, 2005; Ferreira *et al.*, 2017).

8.6.2. 3D turbulence measurements

The study has used surface flow velocities to infer near-bed flow conditions. Although common place in hillslope studies, such as though the use of correction factors in dye tracing velocity measurement (e.g. Pan, Shangguan and Ma, 2015) there is presently no means by which to correlate the surface velocities with the velocity experienced at the bed surface. In open channel flows, various different velocity profiles shapes has been observed, such as logarithmic, s-shape and linear (Mignot *et al.*, 2009; Dey and Das, 2012) that allow such a correlation. Thus how the results may differ using measurements of near-bed flow are unclear. Thus efforts should be made to establish the inner flow structure for shallow overland flows. Furthermore, it was not possible to gain turbulence measurements using PTV because of the low seeding densities that occur in multi-threaded flows. Thus,

the turbulence characteristics of overland flows also need to be examined. Ideally these should provide 3D velocity measurements to establish the dynamics of coherent flow structures that might be critical for flow detachment. Furthermore, the effect of the impact of raindrops on overland flow has been ignored. Studies within oceanic environments suggest this difference may be important. Observations have shown that rainfall can attenuate sea-wave height through generating turbulence in the upper column of the water surface (e.g. Nystuen, 1990; Tsimplis, 1992) and can increase water surface roughness (e.g. Moore *et al.*, 1979; Craeye *et al.*, 1997). Thus, it is plausible that in shallow overland flows the exchange of momentum between a raindrop and the surrounding flow might influence its flow structure and resulting detachment rates.

As highlighted in Chapter 2, most current velocimeters are unsuitable for overland flows, and therefore these future avenues for research are a significant technical challenge. Many studies have been able to use photogrammetric velocimetry measurement to study three-dimensional flows (e.g. Malik *et al.*, 1993; Ranchon *et al.*, 2015; Bocanegra Evans *et al*., 2016). However, none has used 3D photogrammetric velocimetry measurements to study multi-threaded flows of the depths typical of overland flows, especially interrill flows. Recent development of research equipment and software has opened many doors of opportunity to perform more extreme experiments effectively and affordably. As high-speed cameras are becoming more affordable and portable, software that are capable of measuring three-dimensional velocities are also becoming more reliable. Particle Tracking Velocimetry software such as OpenPTV (OpenPTV Consortium, 2014),

ImageJ toolbox, Mosaic (Mosaic Group, 2017) and Trackpy (Allan et al., 2016), are opensource software that can all handle three-dimensional velocimetry, and are widely used in velocimetry related researches. By being able to measure shallow flows in three-dimensions, the understanding of the turbulent flow of shallow overland flow will dramatically improve.

8.7. Key findings

This series of study has demonstrated that surface roughness properties which consist of local roughness and random roughness play significant roles in governing the hydraulics of overland flow. Local roughness which is the spatiotemporal variation of surface roughness (Haubrock *et al.*, 2009) was found to be highly correlated to the velocity at the location which both occur. This relationship shows that the evaluation of stream velocity could be gained from the root-mean square of surface elevation of a specified surface area.

Additionally the *RR* of surfaces showed relatively high correlation with surface drag force. With further investigation on how these relate, *RR* has the potential to estimate the erosion rate since surface drag highly correlates with erosion rate (Bonelli *et al.*, 2017). Random roughness is also a property that is correlated to many flow properties (See Chapter 7).

CHAPTER 9
Conclusion

Using an experimental plot, rainfall simulation experiments were performed to quantify the microtopography of eroded soils and to examine its effect on the spatial patterns of overland flow and fluid drag force. A particular emphasis was placed on developing low-cost photogrammetric techniques to provide novel, high spatial resolution measurements of surface DEMs, 2-D flow velocities and distributions of inundation levels. Overland flow experiments were run over surfaces with differing topographies to further examine the effect of discharge and relative submergence on the spatial patterns of overland flow velocities, hydraulic resistance and fluid drag.

The tests to examine the accuracy of Structure-from-Motion (SfM) suggested that SfM is capable of producing highly accurate measurements of microtopographic features at a scale similar to those found on rilled soil surfaces. And for the first time, the results shown in chapter 4 provide crucial information on how to optimize the acquisition of SFM-imagery in different lightning situations and using different cameras. At the scale of 250 × 250 mm, statistical tests revealed that SfM was able to reconstruct more than 99% of points within a 1 mm accuracy. These results have provided confidence in using SfM to measure the microtopography of eroded soils.

Five surface with different microtopographies were generated using simulated rainfall at a constant monsoon intensity of 110 mm h^{-1} using five different plot slopes. The experimented surfaces before and after the simulated rainfall were converted into digital elevated models (DEMs) using SfM. Statistical analyses were performed to evaluate the properties of the eroded surfaces. The surface elevations all had a normal distribution whose shape varied strongly with plot slope. Moment analyses showed that the standard deviation and range of surface elevations, both measures of surface roughness, had strong power relationships with plot slope. The skewness showed a strong negative relationship with slope. These relationships reflected the dependency of the depth and severity of the rills with slope. The kurtosis was fairly invariant with slope. Together these relationships reveal the potential to estimate soil surface roughness and the distribution of elevations based on just one, simple, easy-to-measure, parameter. Further tests over a range of different rainfall events and soils are required to test this potential. Second-order structure function were used to quantity the organisation of the surface. They revealed that eroded surfaces possess complex topography (low Hurst exponents). The results also suggested that eroded surfaces have longer roughness scales in the streamwise than in the lateral direction due to rilling of the surface. However these length scales showed no clear relationship with slope suggesting that for eroded soil surfaces containing both grain and form roughness (primarily rills), these roughness measures provide a poor representation of surface structure.

For each surface, three overland flow discharges were generated at the upslope end of the plot to create differing flow submergences. A Particle Tacking

Velocimetry system was developed to measure the 2D surface flow velocities of the resulting flows. The results showed that streamwise and lateral velocities have high spatial variability, revealing the flow was 2D. Each exhibited a differing distribution. The streamwise velocities had a Gumbel distribution while the lateral velocities had a Logistic distribution. The mean streamwise velocity across all the studied flows was ~0.32 m sec^{-1} with a standard deviation of ~0.16 m sec^{-1} (~50% of the mean), while the lateral direction had a mean ~0 m sec^{-1} and a standard deviation of ~0.12 m sec^{-1}. The notably lower mean velocity in the lateral direction most likely resulted from the characteristics of the eroded surfaces, in which the roughness scales were longer in the streamwise direction. The distribution shape of streamwise velocities was dependent upon discharge and thus relative submergence. At the higher flow discharges and relative submergences, the spatial variability in streamwise velocity was higher and the distributions were wider, flatter and more skewed.

To examine the effect of microtopography on the spatial patterns of overland flow velocity, a correlation analysis between the georeferenced DEMs and vector fields was performed. This analysis revealed that the level of correlation between the surface elevations and streamwise velocity increased with plot slope, surface roughness and inundation ratio. This rise coincided with an increase in the depth and severity of rilling, showing that interrill flows are poorly correlated with the surface elevations. Only at the higher slopes and levels of roughness was the streamwise velocity and absolute velocity reasonably well correlated with the surface elevation. Even over the rilled surfaces, however, the correlation values were not sufficiently high to suggest that overland flow velocity can be predicted well by

surface elevations alone. The lateral velocity had a weak correlation with elevation. The correlation between the local roughness and streamwise velocity was, however stronger, suggesting that local variations in surface elevations are more important in controlling spatial patterns of overland flow velocity.

The hydraulic resistance, estimated by the Darcy-Weisbach friction factor, varied strongly with the Reynolds number when the flows were fully turbulent but not when they were close to being transitional, such as in shallow, interrill flows. Surface roughness and relative submergence were found to have a greater or equally strong control as Reynolds number on hydraulic resistance.

Estimates of fluid drag force made using the georeferenced DEMs and vector fields revealed that drag force varied considerably over eroded soil surfaces, with some areas experiencing forces an order magnitude higher than others. Areas of high drag forces correlated with the walls of rills and with areas in which flows converged from different rills. This correlation occurred because high velocity areas correlated with highly exposed microtopography. Thus, the distributions of drag force provide some explanation for why rills expand, deepen and migrate, as well as why erosion rates are so variable over hillslopes.

The drag force distributions were well-approximated by a two-parameter Weibull distribution for all flows and surfaces. The shape and scaling parameters of these distributions were shown to be heavily dependent upon surface roughness and hydraulic resistance, and to a lesser extent, relative submergence. The strength of these relationships revealed the potential to predict the drag force distribution, and

thus spatial patterns of hydraulic resistance and erosion, based on these simple parameters.

Overall, the study has provided the first detailed study of the effect of microphotography on overland flow patterns, revealing new understanding of the statistical properties of eroded surfaces and the control of roughness on the distribution of 2D velocities, drag force and hydraulic resistance. These results have important implications for the modelling of overland flow and resultant flow detachment. In doing so, the study has demonstrated the great potential of low-cost photogrammetric techniques for providing new understanding of the physics of overland flows, and thus, in the future, driving the development of more physically-based erosion models. Future work should focus on two aspects. First, exploring how the observed relationships with microtopography vary when the surface is mobile. Secondly, establishing the turbulent nature of the inner flow structure of shallow overland flows under rainfall. This later focus remains a significant technical challenge.

Bibliography

Aberle, J. and Nikora, V. (2006) 'Statistical properties of armored gravel bed surfaces', Water Resources Research, 42(11), pp. 1–11. doi: 10.1029/2005WR004674.

Abrahams, A. D. et al. (2001) 'a Sediment Transport Equation for Interrill Overland Flow on Rough Surfaces', 1459, pp. 1443–1459.

Abrahams, A. D., Parsons, A. J. and Luk, S.-H. (1986) 'Field measurement of the velocity of overland flow using dye tracing', Earth Surface Processes and Landforms. John Wiley & Sons, Ltd, 11(6), pp. 653–657. doi: 10.1002/esp.3290110608.

Abrahams, A. D., Parsons, A. J. and Luk, S. H. (1986) 'Resistance to overland flow on desert hillslopes', Journal of Hydrology, 88(3–4), pp. 343–363. doi: 10.1016/0022-1694(86)90099-5.

Abrahams, A. D., Parsons, A. J. and Luk, S. H. (1989) 'Distribution of depth of overland flow on desert hillslopes and its implications for modeling soil erosion', Journal of Hydrology, 106(1–2), pp. 177–184. doi: 10.1016/0022-1694(89)90173-X.

Abràmoff, M. D., Magalhães, P. J. and Ram, S. J. (2004) 'Image processing with imageJ', Biophotonics International, pp. 36–41. doi: 10.1117/1.3589100.

Adelsberger, K. A. and Smith, J. R. (2009) 'Desert pavement development and landscape stability on the Eastern Libyan Plateau, Egypt', Geomorphology. Elsevier B.V., 107(3–4), pp. 178–194. doi: 10.1016/j.geomorph.2008.12.005.

Adobe Systems (2017a) 'Adobe Lightroom'.

Adobe Systems (2017b) 'Adobe Photoshop CC 2017 (Windows)'.

Agisoft LLC (2016) Agisoft PhotoScan User Manual : Professional Edition, Version 1.3, User Manuals.

Allan, D. et al. (2016) 'trackpy: Trackpy v0.3.2'. doi: 10.5281/ZENODO.60550.

Berger, C. et al. (2010) 'Rill development and soil erosion: A laboratory study of slope and rainfall intensity', Earth Surface Processes and Landforms, 35(12), pp. 1456–1467. doi: 10.1002/esp.1989.

Bergeron, N. E. (1996) 'Scale-space analysis of stream-bed roughness in coarse gravel-bed streams', Mathematical Geology, 28(5), pp. 537–561. doi: 10.1007/BF02066100.

Blott, S. J. and Pye, K. (2001) 'GRADISTAT: a grain size distribution and statistics package for the analysis of unconsolidated sediments', Earth Surface Processes and Landforms. John Wiley & Sons, Ltd., 26(11), pp. 1237–1248. doi: 10.1002/esp.261.

Bocanegra Evans, H. et al. (2016) 'Holographic microscopy and microfluidics platform for measuring wall stress and 3D flow over surfaces textured by

micro-pillars', Scientific Reports. Nature Publishing Group, 6(January), p. 28753. doi: 10.1038/srep28753.

Bonelli, S. et al. (2017) 'Criteria of erosion for cohesive soils To cite this version : HAL Id : hal-01007486'.

Bryan, R. B. (2000) 'Soil erodibility and process of water erosion on hillslope', Geomorphology, 32(3–4), pp. 385–415.

Buffin-Bélanger, T. and Roy, A. G. (2005) '1 min in the life of a river: Selecting the optimal record length for the measurement of turbulence in fluvial boundary layers', Geomorphology, 68(1–2), pp. 77–94. doi: 10.1016/j.geomorph.2004.09.032.

Bullard, J. E. et al. (2018) 'Impact of multi-day rainfall events on surface roughness and physical crusting of very fine soils', Geoderma. Elsevier, 313(October 2017), pp. 181–192. doi: 10.1016/j.geoderma.2017.10.038.

Carrivick, J. L., Smith, M. W. and Quincey, D. J. (2016) 'Structure from Motion in the Geosciences', in Structure from Motion in the Geosciences, pp. 37–59. doi: 10.1017/CBO9781107415324.004.

Cea, L. et al. (2014) 'Experimental validation of a 2D overland flow model using high resolution water depth and velocity data', Journal of Hydrology. Elsevier B.V., 513, pp. 142–153. doi: 10.1016/j.jhydrol.2014.03.052.

Chu, X., Yang, J. and Chi, Y. (2012) 'Quantification of soil random roughness and surface depression storage: Methods, applicability, and limitations', Transactions of the ASABE, 55(5), pp. 1699–1710. Available at:

http://www.scopus.com/inward/record.url?eid=2-s2.0-84872357536&partnerID=40&md5=f222a6eea94ce8095e3279899dcf8d50.

CloudCompare (2017) 'CloudCompare'. Available at: http://www.cloudcompare.org/.

Cooper, J. R. (2012) 'Does flow variance affect bedload flux when the bed is dominated by grain roughness?', Geomorphology, 141–142, pp. 160–169. doi: 10.1016/j.geomorph.2011.12.039.

Cooper, J. R. and Tait, S. J. (2008) 'The spatial organisation of time-averaged streamwise velocity and its correlation with the surface topography of water-worked gravel beds', Acta Geophysica, 56(3), pp. 614–641. doi: 10.2478/s11600-008-0023-0.

Cooper, J. R. and Tait, S. J. (2009) 'Water-worked gravel beds in laboratory flumes – a natural analogue?', Earth Surface Processes and Landforms, 34(November), pp. 384–397. doi: 10.1002/esp.

Craeye, C., Sobieski, P. W. and Bliven, L. F. (1997) 'Scattering by artificial wind and rain roughened water surfaces at oblique incidences', International Journal of Remote Sensing. Taylor & Francis, 18(10), pp. 2241–2246. doi: 10.1080/014311697217864.

Darboux, F. et al. (2001) 'Evolution of soil surface roughness and flowpath connectivity in overland flow experiments', Catena, 46, pp. 125–139.

Detert, M. and Weitbrecht, V. (2015) 'A low-cost airborne velocimetry system: proof of concept', Journal of Hydraulic Research. Taylor & Francis, 53(4), pp. 532–539. doi: 10.1080/00221686.2015.1054322.

Dey, S. and Das, R. (2012) 'Gravel-Bed Hydrodynamics : Double-Averaging Approach', Journal of Hydraulic Engineering, 138(8), pp. 707–725. doi: 10.1061/(ASCE)HY.1943-7900.0000554.

Engman, E. T. and Eswin, T. E. (1986) 'Roughness Coefficients for Routing Surface Runoff', Journal of Irrigation and Drainage Engineering, 112(1), pp. 39–53.

Evans, M., Hastings, N. and Peacock, B. (2000) Statistical Distributions. Wiley (Wiley Series in Probability and Statistics). Available at: https://books.google.co.th/books?id=zAApTi9kAg4C.

Favis-Mortlock, D. T. et al. (2000) 'Emergence and erosion: a model for rill initiation and development', Hydrological Processes, 14(July 1999), pp. 2173–2205. doi: 10.1002/1099-1085(20000815/30)14:11/12<2173::AID-HYP61>3.0.CO;2-6.

Ferreira, E. et al. (2017) 'Automated extraction of free surface topography using SfM-MVS photogrammetry', Flow Measurement and Instrumentation, 54 (December 2016), pp. 243–249. doi: 10.1016/j.flowmeasinst.2017.02.001.

Fritz, a., Kattenborn, T. and Koch, B. (2013) 'UAV-Based Photogrammetric Point Clouds – Tree Stem Mapping in Open Stands in Comparison to Terrestrial Laser Scanner Point Clouds', ISPRS - International Archives of the Photogrammetry, Remote Sensing and Spatial Information Sciences, XL-1/W2(September), pp. 141–146. doi: 10.5194/isprsarchives-XL-1-W2-141-2013.

Fu, S., Biwolé, P. and Mathis, C. (2015) 'A Comparative Study of Particle Image Velocimetry (PIV) and Particle Tracking Velocimetry (PTV) for Airflow Measurement', 9(1), pp. 40–45.

Furbish, D. J. et al. (2007) 'Rain splash of dry sand revealed by high-speed imaging and sticky paper splash targets', Journal of Geophysical Research: Earth Surface, 112(1), pp. 1–19. doi: 10.1029/2006JF000498.

Furukawa, Y. and Ponce, J. (2007) 'Accurate, Dense, and Robust Multi-View Stereopsis'. doi: http://doi.ieeecomputersociety.org/10.1109/TPAMI.2009.161.

Gilley, J. E., Kottwitz, E. R. and Wieman, G. a. (1992) 'Darcy-Weisbach Roughness Coefficients for Gravel and Cobble Surfaces', Journal of Irrigation and Drainage Engineering, 118(1), pp. 104–112. doi: 10.1061/(ASCE)0733-9437(1992)118:1(104).

Govers, G., Takken, I. and Helming, K. (2000) 'Soil roughness and overland flow', Agronomie, 20(2), pp. 131–146. doi: 10.1051/agro:2000114.

Gust, G. and Southard, J. B. (1983) 'Effects of weak bed load on the Universal Law of the Wall', Journal of Geophysical Research: Oceans, 88(C10), pp. 5939–5952. doi: 10.1029/JC088iC10p05939.

Hansen, B., Schjønning, P. and Sibbesen, E. (1999) 'Roughness indices for estimation of depression storage capacity of tilled soil surfaces', Soil and Tillage Research, 52(1–2), pp. 103–111. doi: 10.1016/S0167-1987(99)00061-6.

Harwin, S. and Lucieer, A. (2012) 'Assessing the accuracy of georeferenced point clouds produced via multi-view stereopsis from Unmanned Aerial Vehicle (UAV) imagery', Remote Sensing, 4(6), pp. 1573–1599. doi: 10.3390/rs4061573.

Haubrock, S. N. et al. (2009) 'Spatiotemporal variations of soil surface roughness from in-situ laser scanning', Catena. Elsevier B.V., 79(2), pp. 128–139. doi: 10.1016/j.catena.2009.06.005.

Hergault, V. et al. (2010) 'Image processing for the study of bedload transport of two-size spherical particles in a supercritical flow', Experiments in Fluids, 49(5), pp. 1095–1107. doi: 10.1007/s00348-010-0856-6.

Hooke, J. and Sandercock, P. (2012) 'Use of vegetation to combat desertification and land degradation: Recommendations and guidelines for spatial strategies in Mediterranean lands', Landscape and Urban Planning, 107(4), pp. 389–400. doi: 10.1016/j.landurbplan.2012.07.007.

Huang, C. -h and Bradford, J. M. (1990) 'Depressional storage for Markov-Gaussian surfaces', Water Resources Research, 26(9), pp. 2235–2242. doi: 10.1029/WR026i009p02235.

Javernick, L., Brasington, J. and Caruso, B. (2014) 'Modeling the topography of shallow braided rivers using Structure-from-Motion photogrammetry', Geomorphology. Elsevier B.V., 213, pp. 166–182. doi: 10.1016/j.geomorph.2014.01.006.

Kashyap, S. et al. (2010) 'A semi-permanent method for fixing sand beds in laboratory flumes', Journal of Hydraulic Research, 48(3), pp. 377–382. doi: 10.1080/00221686.2010.481831.

Khalil, M. B. (1972) 'On preserving the sand patterns in river models', Journal of Hydraulic Research, 10(3), pp. 291–303. doi: 10.1080/00221687209500162.

Kinnell, P. I. A. (1991) 'Effect of flow depth on sediment transport induced by raindrops impacting shallow flows', Transactions of the ASAE, 34(1), pp. 161–168. doi: 10.13031/2013.31639.

Kinnell, P. I. A. (1993) 'Interrill erodibilities based on the rainfall intensity-flow discharge erosivity factor', Australian Journal of Soil Research, 31(3), pp. 319–332. doi: 10.1071/SR9930319.

Kinnell, P. I. A. (2000) 'The effect of slope length on sediment concentrations associated with side-slope erosion', Soil Sci. Soc. Am. J, 64, pp. 1004–1008. doi: 10.2136/sssaj2000.6431004x.

Kinnell, P. I. A. (2001) 'Particle travel distances and bed and sediment compositions associated with rain-impacted flows', Earth Surface Processes and Landforms, 26(7), pp. 749–758. doi: 10.1002/esp.221.

Kirkby, M. (2001) 'Modelling the interactions between soil surface properties and water erosion Modelisation des interactions entre caracteristiques superficielles des sols et erosion hydrique ′', Catena, 46, pp. 89–102. doi: 10.1016/S0341-8162(01)00160-6.

Lague, D., Brodu, N. and Leroux, J. (2013) 'Accurate 3D comparison of complex topography with terrestrial laser scanner: Application to the Rangitikei canyon (N-Z)', ISPRS Journal of Photogrammetry and Remote Sensing. International Society for Photogrammetry and Remote Sensing, Inc. (ISPRS), 82, pp. 10–26. doi: 10.1016/j.isprsjprs.2013.04.009.

Lamarre, H. and Roy, A. G. (2005) 'Reach scale variability of turbulent flow characteristics in a gravel-bed river', Geomorphology, 68(1–2), pp. 95–113. doi: 10.1016/j.geomorph.2004.09.033.

Lascelles, B. et al. (2000) 'Spatial and temporal variation in two rainfall simulators: implications for spatially explicit rainfall simulation experiments', Earth Surface Processes and Landforms. Wiley Online Library, 25(7), pp. 709–721.

Lawrence, D. S. L. (1997) 'Macroscale surface roughness and frictional resistance in overland flow', Earth Surface Processes and Landforms, 22(4), pp. 365–382. doi: 10.1002/(SICI)1096-9837(199704)22:4<365::AID-ESP693>3.0.CO;2-6.

LEGO (2017a) How LEGO® bricks are made, LEGO. Available at: https://www.lego.com/en-gb/service/help/fun-for-fans/more-about-us/how-lego-bricks-are-made-408100000007834 (Accessed: 1 August 2017).

LEGO (2017b) 'LEGO.com Digital Designer Virtual Building Software'. Available at: http://ldd.lego.com/en-gb/ (Accessed: 1 August 2017).

Legout, C. et al. (2012) 'High spatial resolution mapping of surface velocities and depths for shallow overland flow', Earth Surface Processes and Landforms, 37(9), pp. 984–993. doi: 10.1002/esp.3220.

Li, M. Z. (1994) 'Direct skin friction measurements and stress partitioning over movable sand ripples', Journal of Geophysical Research, pp. 791–799. doi: 10.1029/93JC02445.

Lorna, C. et al. (2005) 'Bed-Load Effects on Hydrodynamics of Rough-Bed Open-Channel Flows', Journal of Hydraulic Engineering. American Society of Civil Engineers, 131(7), pp. 576–585. doi: 10.1061/(ASCE)0733-9429(2005)131:7(576).

Malik, N. A., Dracos, T. and Papantoniou, D. . (1993) 'Particle Tracking Velocimetry in Three-dimensional Flow', Experiments in Fluids, 15, pp. 279–294.

Mao, L., Cooper, J. R. and Frostick, L. E. (2011) 'Grain size and topographical differences between static and mobile armour layers', Earth Surface Processes and Landforms, 36(10), pp. 1321–1334. doi: 10.1002/esp.2156.

Mathworks (2017) 'Matlab R2017'.

Matthews, N. a. (2008) 'Aerial and Close-Range Photogrammetric Technology', Technical Note 428, p. 42. doi: 10.1017/CBO9781107415324.004.

Michaelides, K. and Wainwright, J. (2008) 'Internal testing of a numerical model of hillslope–channel coupling using laboratory flume experiments', Hydrological Processes, 22(October), pp. 2274–2291. doi: 10.1002/hyp.

Mignot, E., Barthelemy, E. and Hurther, D. (2009) 'Double-averaging analysis and local flow characterization of near-bed turbulence in gravel-bed channel flows', Journal of Fluid Mechanics, 618, pp. 279–303. doi: 10.1017/S0022112008004643.

Minitab (2017) ‘Minitab 17’.

Mohajeri, S. H. et al. (2015) ‘The structure of gravel-bed flow with intermediate submergence: A laboratory study’, Water Resources Research, 51. doi: 10.1002/2015WR017273.

Moore, R. et al. (1979) ‘Preliminary study of rain effects on radar scattering from water surfaces’, IEEE Journal of Oceanic Engineering, 4(1), pp. 31–32. doi: 10.1109/JOE.1979.1145408.

Mosaic Group (2017) ‘Mosaic’. Available at: http://mosaic.mpi-cbg.de/.

Natural England (2014) National Character Area Profile: Wirral.

Nearing, M. A. et al. (1997) ‘Hydraulics and erosion in eroded rills’, Water Resources Research, 33, pp. 865–876.

Nikora, V. I., Goring, D. G. and Biggs, B. J. F. (1998) ‘On gravel-bed roughness characterization’, Water Resources Research, 34(3), pp. 517–527. doi: 10.1029/97WR02886.

Nystuen, J. A. (1990) ‘A note on the attenuation of surface gravity waves by rainfall’, Journal of Geophysical Research: Oceans, 95(C10), pp. 18353–18355. doi: 10.1029/JC095iC10p18353.

OpenPTV Consortium (2014) ‘OpenPTV’. Available at: http://openptv.net.

Pan, C., Shangguan, Z. and Ma, L. (2015) ‘Assessing the dye-tracer correction factor for documenting the mean velocity of sheet flow over smooth and grassed

surfaces', Hydrological Processes, 29(26), pp. 5369–5382. doi: 10.1002/hyp.10565.

Parsons, A. J. et al. (2006) 'Scale relationships in hillslope runoff and erosion', Earth Surface Processes and Landforms, 31(April), pp. 1384–1393. doi: 10.1002/esp.

Parsons, A. J. et al. (2014) 'The use of RFID in soil-erosion research', Earth Surface Processes and Landforms, 39(12), pp. 1693–1696. doi: 10.1002/esp.3628.

Parsons, A. J., Abrahams, A. D. and Luk, S. -H (1991) 'Size characteristics of sediment in interrill overland flow on a semiarid hillslope, Southern Arizona', Earth Surface Processes and Landforms, 16(2), pp. 143–152. doi: 10.1002/esp.3290160205.

Parsons, A. J., Abrahams, A. D. and Wainright, J. (1996) 'Responses of interrill runoff and erosion rates to vegetation change in southern Arizona', Geomorphology, 14, pp. 311–317. doi: 10.1016/0169-555X(95)00044-6.

Parsons, A. J. and Wainwright, J. (2006) 'Depth distribution of interrill overland flow and the formation of rills', Hydrological Processes, 20(7), pp. 1511–1523. doi: 10.1002/hyp.5941.

Poesen, J. and Savat, J. (1981) 'Detachment and transportation of losse sediments by rainfall splash', Catena, 8(1), pp. 19–41. doi: 10.1016/S0341-8162(81)80002-1.

Prasad, S. N., Suryadevara, M. R. and Romkens, M. J. M. (2009) 'Grain transport mechanics in shallow overland flow', Ecohydrology, 2, pp. 248–256. doi: 10.1002/eco.

Prosdocimi, M. et al. (2015) 'Bank erosion in agricultural drainage networks: New challenges from structure-from-motion photogrammetry for post-event analysis', Earth Surface Processes and Landforms, 40(14), pp. 1891–1906. doi: 10.1002/esp.3767.

Quansah, C. (1981) 'The effect of soil type, slope, rain intensity and their interactions on splash detachment and transport', Journal of Soil Science, 32(2), pp. 215–224. doi: 10.1111/j.1365-2389.1981.tb01701.x.

Raffel, M. et al. (2007) Particle Image Velocimetry, Current Science. doi: 10.1007/978-3-540-72308-0.

Ranchon, H., Picot, V. and Bancaud, A. (2015) 'Metrology of confined flows using wide field nanoparticle velocimetry', Scientific Reports. Nature Publishing Group, 5(MAY 2015), p. 10128. doi: 10.1038/srep10128.

Remondino, F. and El-Hakim, S. (2006) 'Image-based 3D Modelling: A Review', The Photogrammetric Record. Blackwell Publishing Ltd, 21(115), pp. 269–291. doi: 10.1111/j.1477-9730.2006.00383.x.

Rice, S. P., Buffin-Bélanger, T. and Reid, I. (2014) 'Sensitivity of interfacial hydraulics to the microtopographic roughness of water-lain gravels', Earth Surface Processes and Landforms, 39(2), pp. 184–199. doi: 10.1002/esp.3438.

Rimkus, A. (2012) 'Structure of turbulent vortices in a compound channel', Archives of Hydroengineering and Environmental Mechanics, 59(3–4), pp. 113–135. doi: 10.2478/heem-2013-0003.

Robert, A. (2014) RIVER PROCESSES: An Introduction to Fluvial Dynamics. Taylor & Francis. Available at: https://books.google.co.uk/books?id=ZcaOAwAAQBAJ.

Römkens, M. J. M., Helming, K. and Prasad, S. N. (2002) 'Soil erosion under different rainfall intensities, surface roughness, and soil water regimes', Catena, 46(2–3), pp. 103–123. doi: 10.1016/S0341-8162(01)00161-8.

Sbalzarini, I. F. and Koumoutsakos, P. (2005) 'Feature point tracking and trajectory analysis for video imaging in cell biology', Journal of Structural Biology, 151(2), pp. 182–195. doi: 10.1016/j.jsb.2005.06.002.

Shit, P. K. and Maiti, R. (2012) 'Rill Hydraulics - An Experimental Study on Gully Basin in Lateritic Upland of Paschim Medinipur , West Bengal , India', Journal of Geography and Geology, 4(4), pp. 1–11. doi: 10.5539/jgg.v4n4p1.

Skarlatos, D. and Kiparissi, S. (2012) 'Comparison of Laser Scanning, Photogrammetry and Sfm-Mvs Pipeline Applied in Structures and Artificial Surfaces', ISPRS Annals of the Photogrammetry, Remote Sensing and Spatial Information Sciences, I-3(September), pp. 299–304. doi: 10.5194/isprsannals-I-3-299-2012.

Smith, M. W., Carrivick, J. L. and Quincey, D. J. (2015) 'Structure from motion photogrammetry in physical geography', Progress in Physical Geography, 40(2), pp. 247–275. doi: 10.1177/0309133315615805.

Smith, M. W., Cox, N. J. and Bracken, L. J. (2007) 'Applying flow resistance equations to overland flows', Progress in Physical Geography, 31(4), pp. 363–387. doi: 10.1177/0309133307081289.

Smith, M. W., Cox, N. J. and Bracken, L. J. (2011a) 'Modeling depth distributions of overland flows', Geomorphology, 125(3), pp. 402–413. doi: 10.1016/j.geomorph.2010.10.017.

Smith, M. W., Cox, N. J. and Bracken, L. J. (2011b) 'Terrestrial laser scanning soil surfaces: A field methodology to examine soil surface roughness and overland flow hydraulics', Hydrological Processes, 25(6), pp. 842–860. doi: 10.1002/hyp.7871.

Smith, M. W. and Vericat, D. (2015) 'From experimental plots to experimental landscapes: Topography, erosion and deposition in sub-humid badlands from Structure-from-Motion photogrammetry', Earth Surface Processes and Landforms, 40(12), pp. 1656–1671. doi: 10.1002/esp.3747.

Tamminga, A. D., Eaton, B. C. and Hugenholtz, C. H. (2015) 'UAS-based remote sensing of fluvial change following an extreme flood event', Earth Surface Processes and Landforms, 40(11), pp. 1464–1476. doi: 10.1002/esp.3728.

Tebaldi, C. et al. (2006) 'Going to the extremes: An intercomparison of model-simulated historical and future changes in extreme events', Climatic Change, 79(3–4), pp. 185–211. doi: 10.1007/s10584-006-9051-4.

Thielicke, W. and Stamhuis, E. J. (2014) 'PIVlab - Towards User-friendly, Affordable and Accurate Digital Particle Image Velocimetry in MATLAB', Journal of Open Research Software, 2(1), p. e30. doi: 10.5334/jors.bl.

Torri, D., Sfalanga, M. and Del Sette, M. (1987) 'Splash detachment: Runoff depth and soil cohesion', Catena, 14(1–3), pp. 149–155. doi: 10.1016/S0341-8162(87)80013-9.

Tropea, C., Yarin, A. L. and Foss, J. F. (2007) 'Springer Handbook of Experimental Fluid Mechanics', AIAA Journal, 46, pp. 2653–2655. doi: 10.2514/1.38773.

Tsimplis, M. N. (1992) 'The Effect of Rain in Calming the Sea', Journal of Physical Oceanography. American Meteorological Society, 22(4), pp. 404–412. doi: 10.1175/1520-0485(1992)022<0404:TEORIC>2.0.CO;2.

Vanoni, V. A. and Nomicos, G. N. (1959) 'Resistance properties of sediment-laden streams', Journal of the Hydraulics Division, 85, pp. 77–107. Available at: https://authors.library.caltech.edu/49212/.

Vidal, E. V. A. et al. (2010) 'Evolution of the Soil Surface Roughness Using Geostatistical Analysis (1)', pp. 141–152.

Wainwright, J., Parsons, A. J., Muller, E. N., Brazier, R. E., Powell, D. M., et al. (2008) 'A Transport-Distance Approach to Scaling Erosion Rates: 2. Sensitivity and Evaluation of MAHLERAN', Earth Surface Processes and Landforms, 33(January), pp. 962–984. doi: 10.1002/esp.

Wainwright, J., Parsons, A. J., Muller, E. N., Brazier, R. E. and Powell, D. M. (2008) 'A transport-distance approach to scaling erosion rates: 3. Evaluating scaling characteristics of MAHLERAN', Earth Surface Processes and Landforms, 33(January), pp. 1113–1128. doi: 10.1002/esp.

Walling, D. and Kleo, A. H. A. (1979) 'Sediment yields of rivers in areas of low precipitation: a global view', IAHS Publ., (128), pp. 479–493.

Westoby, M. J. et al. (2012) '"Structure-from-Motion" photogrammetry: A low-cost, effective tool for geoscience applications', Geomorphology. Elsevier B.V., 179, pp. 300–314. doi: 10.1016/j.geomorph.2012.08.021.